Title
On The Anomalous Conductivity of Low Permittivity Electrolytes Used in Electrochemical Applications

Author
Self, Julian

Publication Date
2021

Peer reviewed|Thesis/dissertation

On The Anomalous Conductivity of Low Permittivity Electrolytes Used in Electrochemical Applications

by

Julian Self

A dissertation submitted in partial satisfaction of the

requirements for the degree of

Doctor of Philosophy

in

Materials Science and Engineering

in the

Graduate Division

of the

University of California, Berkeley

Committee in charge:

Professor Kristin A. Persson, Chair
Professor Bryan D. McCloskey
Professor Mark Asta

Spring 2021

On The Anomalous Conductivity of Low Permittivity Electrolytes Used in Electrochemical Applications

Abstract

On The Anomalous Conductivity of Low Permittivity Electrolytes Used in Electrochemical Applications

by

Julian Self

Doctor of Philosophy in Materials Science and Engineering

University of California, Berkeley

Professor Kristin A. Persson, Chair

Most of the battery electrolyte candidates for multivalent-ion systems (e.g. Mg, Ca) present interesting physicochemical properties. In these are included anomalous conductivity, where molar conductivity increases with salt concentration. This phenomenon is related to the electrochemical performance and electrolyte viability. In this thesis, this phenomenon is explained via understanding and quantification of the strong inter-ionic interactions in solution. To this end, computational methods including classical molecular dynamics and electronic structure methods are combined with dielectric relaxation spectroscopy measurements. Two cases studies with ether based electrolytes, one with $MgTFSI_2$ salt and one with $Ca(BH_4)_2$ are undertaken. In both cases, the anomalous conductivity originates from changes in salt speciation, i.e. changes in the population of distinct chemical species formed by the ions in the solution. A larger fraction of ionic salt species are promoted at higher salt concentration at the expense of larger, associated clusters. Moreover, it is found that the increase in dielectric constant with increasing salt concentration, due to a significant fraction of polar associated salt species, is likely one of the thermodynamic driving forces for this effect. The findings here are important for the rational design of multivalent electrolytes for electrochemical applications, and help inform salt and solvent selection for advanced electrolyte formulations.

Contents

Acknowledgments

This work was conducted under the auspices of the Joint Center for Energy Storage Research (JCESR), an Energy Innovation Hub funded by the U.S. Department of Energy. Computational resources were provided by the National Energy Research Scientific Computing Center (NERSC). I further acknowledge the NIH Grant S10OD023532.

Much of this work was completed in direct collaboration with Kara Fong, Nathan Hahn, Kevin Zavadil and my supervisor Kristin Persson. I additionally thank Brandon Wood, Nidhi Rajput, Kiran Mathew and David Mrdjenovich for many useful and technical discussions. In addition, I acknowledge the Persson group at the Lawrence Berkeley National Lab and UC Berkeley, for which most members, unmentioned here, have provided support in various regards for the completion of this thesis.

Chapter 1

Introduction

The effort by academia and industry to produce the technology and knowledge necessary for the electrification of vehicles has resulted in a tremendous amount of research in electrochemistry, one main focus being rechargeable batteries. Of these, Li-ion is perhaps the most popular. However, due to scarcity of certain battery materials resources, e.g. cobalt,[1] which is found in the commonly-used LCO (lithium cobalt oxide) positive electrode, there is a need for alternative secondary (rechargeable) batteries.[2] One well-known class of secondary batteries are multivalent batteries, where instead of a Li-ion being the electroactive ion, a multivalent ion, e.g. a Mg-ion or Ca-ion is used. While still under research, they present the possibility for less energy-intensive materials processing, higher volumetric capacity, and higher abundance of materials used.[3, 4] This thesis focuses on one component of the battery — the electrolyte. Generally, viable liquid electrolytes for multivalent batteries can be described as having a low permittivity, due to their low dielectric constant as compared to, say, aqueous electrolytes. This leads to a new set of physicochemical properties involving strong interionic interactions and anomalous transport — main topics of this thesis.

In Chapter 1, an introduction to multivalent electrochemistry, speciation and transport of bulk electrolytes, their activity coefficients and dielectric relaxation spectroscopy is provided. In Chapter 2, the methods to model dielectric relaxation spectroscopy on the atomic, molecular and supra-molecular level via molecular dynamics are detailed. Next, In Chapter 3, a case study of $MgTFSI_2$ in G1 (Mg bis(trifluoromethylsulfonyl)imide in monoglyme) and G2 (diglyme) is presented. In Chapter 4, a case study of $Ca(BH_4)_2$ and $Mg(BH_4)_2$ in tetrahydrofuran follows. Finally, in Chapter 5, a conclusion, discussion of open problems and possible further work is detailed.

1.1 Multivalent Electrochemistry

A secondary battery has three primary components: the two electrodes and the electrolyte. In addition, there typically is a separator used between both electrodes to avoid short-circuiting, as well as current collectors to complete the circuit. Figure 1.1 shows a schematic

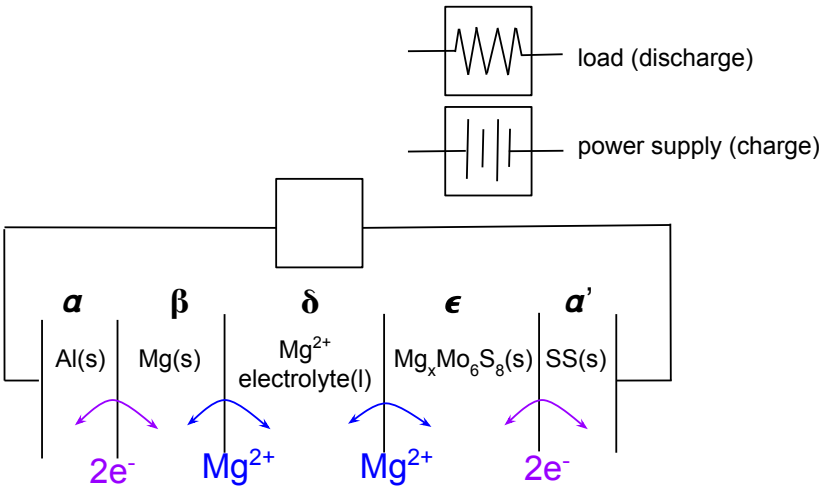

Figure 1.1: Example Mg electrochemical cell shown where the various components are labelled with Greek letters. Either a load or power supply is used during the discharge and charge, respectively.

version of a Mg-ion cell. Aluminum[5] and stainless steel (SS)[6] current collectors are shown (α and α'), while the negative electrode is here Mg-metal (β) and the positive electrode $Mg_xMo_6S_8$(Chevrel, solid, ϵ). There is currently intense research on different chemistries for the positive electrode, for which the reader is referred to a recent review.[2] Between both electrodes is an electrolyte which allows conduction of the electroactive species (in this case Mg^{2+}) from one electrode to the another. More precisely, for this cell, during charge, the Mg^{2+} deintercalates from the $Mg_xMo_6S_8$ and plates on the Mg electrode and vice versa for the discharge (stripping from the Mg metal and intercalation into $Mg_xMo_6S_8$). Ideally, the current collectors allow flow of electrons but not of ions to and from the electrodes, while the electrolyte allows flow of ions but not electrons between electrodes. Since the current collectors are in electrical contact with their respective electrodes, their electrochemical potentials η_e are equal, respectively:

$$\begin{aligned} \eta_e^{\alpha} &= \eta_e^{\beta} \\ \eta_e^{\epsilon} &= \eta_e^{\alpha'} \end{aligned} \tag{1.1}$$

Mg plating and stripping follows the equilibrium:

$$Mg_{(s)} \rightleftharpoons Mg^{2+} + 2e^- \tag{1.2}$$

Accordingly, the Mg plating (or intercalation) process supposes that the chemical potential of the magnesium atom μ_{Mg} in an electrode is equal to the the electrochemical potential of

the Mg ion $\eta_{Mg^{2+}}$ in addition to the electron electrochemical potential η_e multiplied by the ion's charge number:

$$\mu^{\beta}_{Mg} = \eta^{\beta}_{Mg^{2+}} + 2\eta^{\beta}_{e} \tag{1.3}$$

Moreover, at the open circuit voltage, it can be shown that the electrochemical potential of the electroactive ion is equal across the cell components:[7]

$$\eta^{\beta}_{Mg^{2+}} = \eta^{\delta}_{Mg^{2+}} = \eta^{\epsilon}_{Mg^{2+}} \tag{1.4}$$

Using the above relations, the voltage (measured via probing the current collectors) can be directly related to the chemical potential of the Mg atoms:

$$V = -\frac{\eta^{\alpha}_{e} - \eta^{\alpha'}_{e}}{e} = -\frac{\mu^{\beta}_{Mg} - \mu^{\epsilon}_{Mg}}{2e} \tag{1.5}$$

Thus, the voltage of the cell V can be related to the chemical potential difference between the electroactive atom in the two electrodes. In other words, if we have two electrode materials where the chemical potential of the magnesium is different, and intercalation (or plating) is reversible, then in principle these can be used in a battery (with an adequate electrolyte). When current is flowing, either during charge or discharge, the electrolyte allows transport of the electroactive species. It is worth noting that during operation of real cells, there is a significant amount of electroactive species either lost to formation of interphases (or passivation films) on the surface of electrodes or lost to other, perhaps parasitic or deleterious side-reactions. These are generally non-trivial and thus require a careful choice of solvent and salt.[8]

Of the various electrolyte candidates for Mg batteries, ethers such as tetrahydrofuran and glyme-based (e.g. monoglyme, diglyme) have proved among the most promising.[6, 8] Those with TFSI-based salt (bis(trifluoromethylsulfonyl)imide) can have high conductivity (3 mS/cm) compared to other candidates. The high conductivity is a desired feature as low conductivities can lead to a high Ohmic voltage drop at moderate currents. $MgTFSI_2$-ether electrolytes, discussed further in Chapter 3, can show very high dissolution overpotentials, likely due to not a low conductivity but to a non-viable interphase formed on the Mg-surface. To alleviate this issue, a combination of $MgTFSI_2$ with other salts (e.g. $MgCl_2$) can be used.[6] There are many other Mg electroyte systems currently under research for electrochemical application, for which the details are outside the scope of this thesis. These include electrolytes based on magnesium boron clusters and borohydrides, MACC (magnesium aluminum chloride complexes), magnesium organoborates, and phenyl complexes.[2, 8, 9]. Most often, the salts are dissolved in ether-based solvents. Moreover, the use of supporting salt is not uncommon.

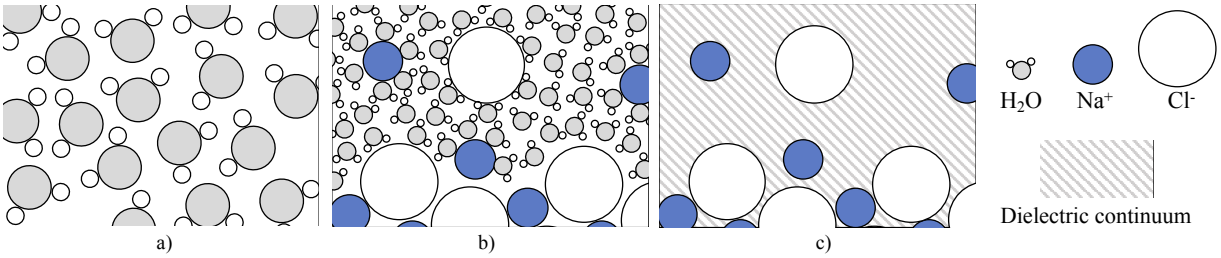

Figure 1.2: Cartoon of water magnified fifty million times (approximately) a). Cartoon of table salt (NaCl) dissolving in water b). Same as b), where the water is represented by a dielectric continuum c.) Legend for ions and molecules on the right. Figures a) and b) are adapted from reference.[10]

1.2 Speciation and Transport of Bulk Electrolytes

As salt is dissolved in a solvent, the salt ions change structure from the solid host lattice to that of ions dissolved and solvated in a liquid. Figure 1.2 shows a molecular-level cartoon representation of the solvent (a) and the dissolution process (b), for an aqueous NaCl electrolyte. Figure 1.2 c) shows the same as b) with the solvent depicted as a structureless dielectric medium instead of in its explicit molecular representation.

For Mg and Ca-based electrochemistry, aqueous electrolytes are generally avoided due to their reactivity with $Mg_{(s)}$ and $Ca_{(s)}$.[11, 12] For 1-1 electrolytes (e.g. singly charged ions) in a non-aqueous polar solvent, at low to moderate concentrations c, the ions are generally completely dissociated. Figure 1.3 (top row) illustrates this for a 1-1 electrolyte. Here, the solvent is represented implicitly as a background continuum, and not in its molecular structure, as in Figure 1.2 c) and b), respectively.

For electrochemical applications, Mg and Ca electrolytes generally use low permittivity solvents due to their relative stability versus the employed electrodes.[8] Low permittivity refers to the lower dielectric constant of the neat solvent (e.g. ε less than 10 without any salt added) as compared to water ($\varepsilon = 78$ at room temperature[13]) In the case of low permittivity 1-1 electrolytes (e.g. Li^+ electrolytes), a possible scenario is shown in Figure 1.3 (middle row), where at low concentrations, there is an abundance of contact ion pairs, where anions and cations are in direct contact and move as one kinetic entity. As concentration increases, there is, counterintuitively, an *increase* in the fraction of free ions. This is due to the *redissociation* mechanism, described later in this chapter. A cartoon for a possible scenario for 2-1 electrolytes (e.g. $MgTFSI_2$ in G1 for use in Mg batteries) is shown in the bottom row. Contact ion pairs and free anions are present in the lower concentration regime, where higher concentrations of salt allow for a higher fraction of free cations. The

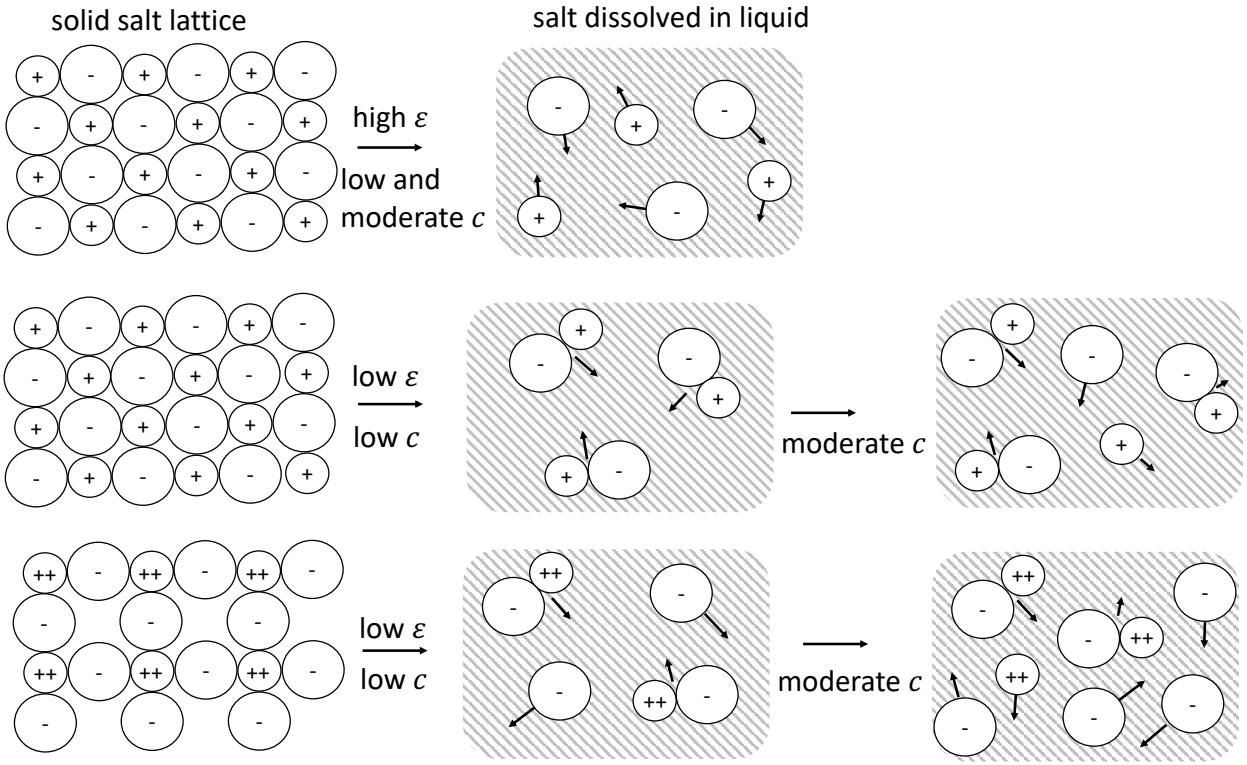

Figure 1.3: Cartoons of ionic dissolution. Top row: 1-1 electrolyte showing no ion pairing in a high permittivity (i.e. high ε) solvent. Middle row: 1-1 electrolyte showing ion pairing with contact ion pairs at low concentration and a higher fraction of free ions as concentration increases. Bottom row: 2-1 electrolyte in a low permittivity electrolyte, with cations in contact ion-pairs. As concentration increases, a higher fraction of free ions is present.

low permittivity, compounded with the stronger charge of multivalent ions (Mg^{2+} and Ca^{2+}) can lead to significant ion association in solution for 2-1 electrolytes, generally speaking, with a non-trivial concentration dependence.

Once dissolved and solvated, ions can conduct current. The conductivity $\sigma = j/E$ can be understood as the inverse of the resistivity, or the current density j for a given electric field magnitude E. A useful quantity to study how conductivity changes with salt concentration is the molar conductivity Λ, which is defined as the following:

$$\Lambda = \sigma/c \tag{1.6}$$

Figure 1.4 shows the measured conductivity (left) and molar conductivity (right) as a function of concentration for various salts in various non-aqueous solvents popular for elec-

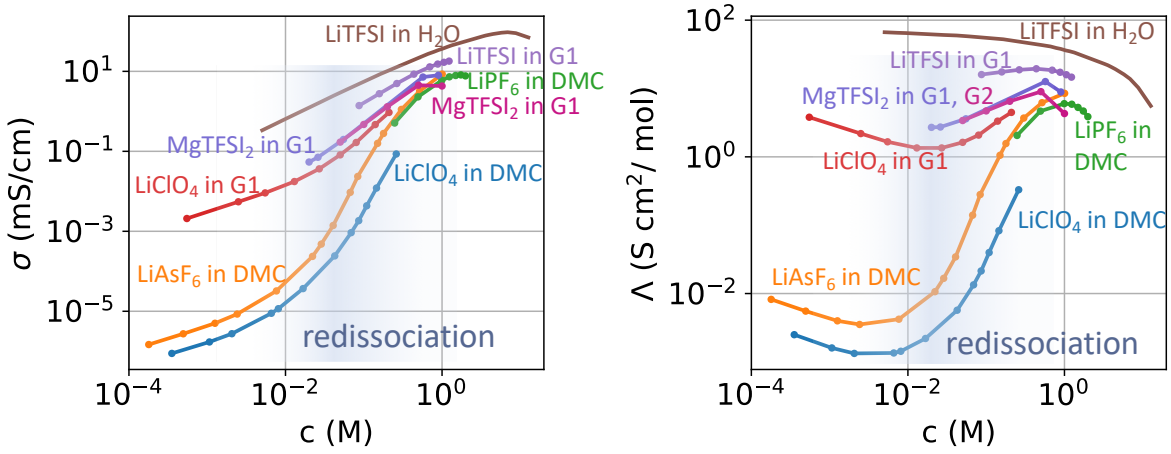

Figure 1.4: Measured conductivity (left) and molar conductivity (right) taken from literature. Regime where molar conductivity increases is highlighted (approximately) by the "redissociation" region, for DMC, G1 and G2 electrolytes.[14, 16–20]

trochemical applications. LiTFSI in an aqueous electrolyte is also shown (brown).[14] For aqueous LiTFSI, the salt is completely or almost completely dissociated and the molar conductivity decreases with concentration (in the entire concentration range studied). For this aqueous electrolyte, σ exhibits a maximum as a function of concentration. At concentrations lower than that of the maximum σ, there is a lower conductivity due to a smaller quantity of charge-carrier ions while at concentrations higher than that of the maximum σ, a combination of viscosity and perhaps some ion pairing (or generally interionic correlations) lead to reduced conductivity. The other electrolytes (e.g. salts in dimethyl carbonate, or DMC, G1 and G2) which are low permittivity electrolytes, show different behavior than the high permittivity 1-1 electrolytes. For concentrations above the dilute limit (e.g. $c > 10^{-2}$ M), the conductivity is much lower than for the aqueous counterpart, and generally the molar conductivity Λ increases with increasing concentration. This is contrary to what is predicted by conventional theories of liquid electrolytes. For example, Kohlrausch's law in very dilute solutions predicts a decrease in molar conductivity proportional to the square root of the concentration,[15] due to electrophoretic and relaxation effects. At higher concentrations, molar conductivity decreases for, say, aqueous electrolytes, due to viscosity increases of the electrolyte as well as ion-ion correlations. The region where molar conductivity Λ is increasing is denoted by the *redissociation* regime drawn in Figure 1.4. This refers to a region where the population fraction of conductive salt species increases, leading to an increase in Λ. This is specific to low permittivity electrolytes, in contradistinction to the aqueous electrolyte shown in brown. The driving forces for redissociation are explained in a following section.

1.3 Activity Coefficients for Strongly-Associating Electrolytes

As salt concentration increases in liquid electrolytes, this inevitably leads to a change in the chemical potentials of all chemical species in solution: salt and solvent. The physical consequences of this include changes in the colligative properties such as freezing point depression and boiling point elevation. The consequences of chemical potential and activity coefficient changes are not solely relegated to colligative properties - activity coefficients are relevant to ion pairing and charge transport. Moreover, solvation thermodynamics, which activity coefficients directly describe, in general have been also found to be tied to electrolyte performance in batteries, both multivalent and Li-ion.[21–23]

In this thesis, the chemical potential (or activity coefficient) of the salt in solution is calculated based on the idea that the contribution to the change in chemical potential comes from four different physicochemical contributions: ideal concentration effects, ion pairing, ion-atmosphere effects[24] (as predicted by Debye-Huckel theory, denoted DH) and solvation effects from varying permittivity (Born solvation, denoted Born):

$$\mu_{\text{salt}} - \mu^0_{\text{salt}} = \Delta\mu_{\text{ideal concentration}} + \Delta\mu_{\text{ion pairing}} + \Delta\mu_{\text{DH}} + \Delta\mu_{\text{Born}} \tag{1.7}$$

It is here stressed that the above contributions to the chemical potential are well known, but research efforts sometimes neglect either Born solvation or Debye-Huckel effects[19, 25]. Moreover, there exist altogether different activity coefficient models, which are discussed further below. Equation 1.7 shows the various contributions to the chemical potential of the salt considered in this work. In order to analyze the various terms, we herein discuss the various contributions more explicitly. Assuming simple monovalent salt components, the $\Delta\mu_{\text{ideal concentration}}$ term is equal to $2RT\ln(c)$. For ion pairing of the simplest kind, an equilibrium is established between free ions S_+, S_- and contact ion pairs (CIPs) S_{CIP}. For a 1-1 electrolyte, we can write:

$$S_+ + S_- \rightleftharpoons S_{\text{CIP}} \tag{1.8}$$

A concentration equilibrium constant can be defined via the following mass-action relationship:

$$K_{\text{A}} = \frac{c_{\text{CIP}}}{c_+ c_-} \tag{1.9}$$

The equilibria between associated salt species and free ions is influenced by the activity coefficients of the respective species, i.e. we can distinguish the activity coefficients of free ions y_+, y_- with those of associated species (e.g. contact ion pairs, y_{CIP}). Using these activity coefficients, the concentration equilibrium constant can be related to the thermodynamic (infinite dilution) equilibrium constant (independent of concentration) K^0_{A}:

$$K_{\text{A}} = K^0_{\text{A}} \frac{y_+ y_-}{y_{\text{CIP}}} \tag{1.10}$$

It is to be noted that the activity coefficients of the various salt species can be directly related to the total activity coefficient ($y_{\pm}$) of the salt, which itself is experimentally measurable (vide infra). For a fraction of free ions α:

$$\mu_{\text{salt}} - \mu^0_{\text{salt}} = \alpha\mu_+ + \alpha\mu_- + (1-\alpha)\mu_{\text{CIP}} \tag{1.11}$$

Here, if $y_{\text{CIP}} = 1$, then $\mu_{\text{CIP}} = \Delta G^0_{\text{A}} + RT\ln(c_{\text{CIP}})$, directly related to the infinite dilution equilibrium constant $K^0_{\text{A}} = \exp(-\Delta G^0_{\text{A}}/(RT))$. The last term $RT\ln(c_{\text{CIP}})$ is the ideal concentration term corrected due to speciation for the CIP species. Here the reference state is that of free ions at infinite dilution, such that, at infinite dilution, all free ion activity coefficients are $y_i = 1$. One of the main driving forces for change in activity coefficients in electrolyte solutions as a function of concentration is long-range electrostatics. These can include long-range electrostatics from the ionic atmosphere (Debye-Huckel) and changes in permittivity coming from the ions present in solution. However, the latter point, although highlighted as early as 1925 by Huckel,[26, 27] has been overlooked by many researchers, which is discussed below. Briefly, the Debye-Huckel theory of ion atmosphere effects accounts for the electrostatic interactions of ions in solution. Generally, the presence of other ions or charged species in solution leads to a lowering of the chemical potential of all the various charged species. A derivation can be found in Newman and Thomas-Alyea.[24] The Debye-Huckel contribution to ions' free energies is dependent on the ions' solution radius (a semi-empirical quantity), the dielectric constant of the solution, the charge number of ions and the ionic strength. Another contribution to the ions' free energy is its Born solvation energy, or its "self-energy", as predicted by the Born energy equation.[28] This contribution is dependent on the ions' solution radius and the dielectric constant of the electrolyte. We can write out the contribution to the free energies from the various electrostatic contributions using the relevant activity coefficients:

$$\mu_+ - \mu^0_+ = RT\ln y_{\text{DH},+} + RT\ln y_{\text{Born},+} + RT\ln(c_+) \tag{1.12}$$

$$\mu_- - \mu^0_- = RT\ln y_{\text{DH},-} + RT\ln y_{\text{Born},-} + RT\ln(c_-) \tag{1.13}$$

Substituting the two above equations in equation 1.11:

$$\mu_{\text{salt}} - \mu^0_{\text{salt}} = \frac{c_+}{c}RT\ln(y_{\text{Born},+}y_{\text{DH},+}c_+) + \frac{c_-}{c}RT\ln(y_{\text{Born},-}y_{\text{DH},-}c_-) + \frac{c_{\text{CIP}}}{c}RT\ln(c_{\text{CIP}}/K^0_{\text{A}}) \tag{1.14}$$

The exact mathematical expression for each of these terms is listed in the Appendix (DH and Born solvation effects are calculated via equations A.1 and A.5). In order to compare to experiment, the experimental quantity $y_{\pm}$ is useful. It is directly relatable to the chemical potential via the following, where a factor of 2 arises from the sum of the ions' charge number:

$$\mu_{\text{salt}} = \mu^0_{\text{salt}} + 2RT\ln(cy_{\pm}) \tag{1.15}$$

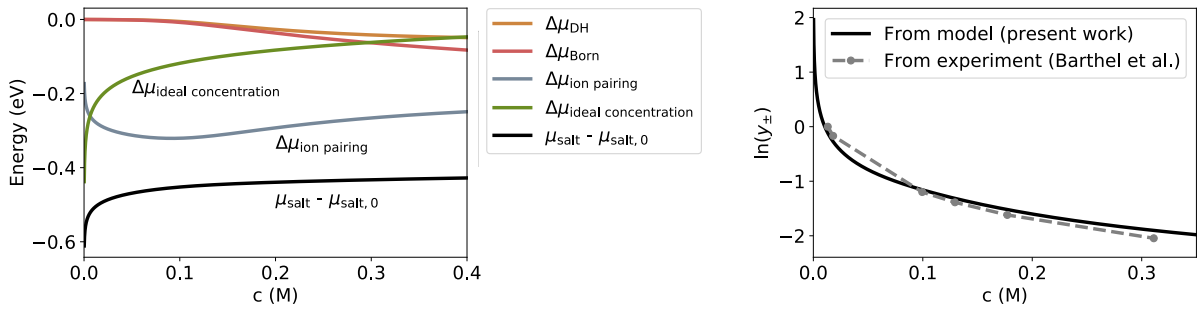

Figure 1.5: Various contributions to the chemical potential of the salt for $LiClO_4$ in G1 (left), using equation 1.14 , and the corresponding concentration-dependent activity coefficient (right). Experimental data taken from Barthel et al.[29] Debye-Huckel radii and Born radii taken from Cachet et al.,[30] concentration-dependent dielectric constant and infinite dilution association constant from Onishi et al.[17]

$$y_\pm = \frac{1}{c}\exp\left(\frac{\mu_{\text{salt}} - \mu^0_{\text{salt}}}{2RT}\right) \tag{1.16}$$

Figure 1.5 shows the contributions to the chemical potential, as listed in equation 1.7, for $LiClO_4$ in G1 (left). $LiClO_4$ is not widely used as a salt in contemporary applications or research due to safety issues,[31] however for many non-aqueous electrolytes, it has been thoroughly characterized, more so than many salts currently used in electrochemical applications, which is why certain $LiClO_4$ case studies are reported here and in the following chapter as they allow comparison to experiment from theoretical or computational models that are the subject of this thesis. For the chemical potential model used in Figure 1.5, the relevant input parameters, namely the relevant ionic radii, infinite dilution association constant and concentration-dependent dielectric constant, were taken from experiment.[17, 30] The model used herein shows agreement with the experimentally measured activity coefficient (right). For comparison of the experimental and model activity coefficients, the reference state was shifted by a constant. Importantly, the agreement suggests that the current proposed contributions to the chemical potential in equation 1.7 are both necessary and sufficient to explain activity coefficients for this low permittivity electrolyte in the low to moderate concentration range (below $\simeq$ 1 M), and arguably for low permittivity electrolytes in general.

Different Activity Cofficient Models

The above described-model considers DH ion atmosphere, ion pairing, and permittivity (e.g. Born Solvation) effects. There exist other activity coefficient models where the assumptions regarding the important thermodynamic driving forces are different. Historically, one of the most important is the model of Pitzer equations.[32, 33] These have been developed

for aqueous electrolytes, but have been used for low permittivity electrolytes.[34] Here, an expansion of the activity coefficient as a function of ionic strength, including DH effects, is used. However, it is here suggested that that Pitzer type models, although allowing phenomenological fitting of the activity coefficients, may miss important physical effects in the underlying model while allowing the many adjustable parameters to fit experimental data. In other words, overfitting may be the consequence of the good agreement of Pitzer equations with experiment. In this way, Pitzer equations may not be the best to predict activity coefficients with little or no a priori experimental data. For example, permittivity changes and the physical effects that follow (e.g. redissociation, discussed in more detail later) are not captured. Pitzer models are generally applied such that the ionic strength is taken as a (weighted) sum over all salt species and not over all charged species, which means that ion-pairing is not well accounted for.[35] Moreover, the dielectric constant is kept constant as a function of salt concentration, an assumption undoubtedly incorrect beyond the dilute limit.

Another model is the mean spherical association (MSA).[35–37] Here, the effect of volume exclusion from the presence of the salt in the solution leads to a correction to the DH expression for chemical potential. As the name implies, radii of interacting spheres are used to model the salt, and can allow reproduction of activity coefficient data. Although the MSA has been used in a way that allows prediction of K_{A}^{0} values for certain cases,[38] it does not by itself allow for the prediction of changes in permittivity, which can dramatically affect the activity coefficients of salt species. Certain authors have enhanced the MSA via accounting for the permittivity changes as an addition to the model, although to the best of our knowledge, such work has not predicted the dielectric constant but rather has relied on experimental data.[39] There is at least one adjustable parameter in the MSA (radius of closest approach), analogous to the radius used in DH theory, which is also either a semi-empirical or adjustable parameter. The hypothesis in this thesis, due to the moderate concentrations studied, is that volume exclusion effects are not one of the major physical mechanisms dictating changes in bulk properties of electrolytes. Permittivity effects and ion-atmosphere effects are assumed as the most significant. As such, the MSA is not considered herein, although it could be incorporated in further work to the methodology in this thesis, where concentration dependent permittivity is modeled.

For aqueous electrolytes, various research groups have proposed that activity coefficients could be well modeled by inclusion of Debye-Huckel, Born and ideal concentrations effects, provided the dielectric constant is known as a function of concentration, with no need for consideration of volume exclusion effects (as in the MSA) or ion pairing.[26, 37, 40, 41] Due to the high permittivity of water, ion pairing is arguably negligible in their studies of 1-1 aqueous electrolytes. However in the solvents studied for Mg and Ca batteries (G1, THF) any reasonable activity coefficient model should incorporate ion pairing, as discussed earlier. Moreover, the concentration-dependent dielectric constant for low permittivity electrolytes can only be understood and predicted via the consideration of ion pairing, as will be shown in a following section. It is noted that the idea of distinct ion speciation, where ions that are close together stay together, is presumably a model well suited for concentrations sufficiently

lower that that of high concentration (e.g. well suited for $c \simeq 1$ M and below). As we approach concentrated and superconcentrated regimes,[42, 43] ions may be best described as neither free nor paired, clustered or aggregated but as correlated to a certain degree. As a perhaps trivial but revealing example, the ions in ionic liquids do not form a single giant aggregate, but are better described as correlated ions in liquid phase. Nonetheless, in the regimes studied in this thesis, ion pairing is assumed to be well suited to described the nanoscopic picture of the salt.

1.4 Dielectric Relaxation Spectroscopy

Despite the importance of the degree of ion pairing in solutions, the speciation in multivalent 2-1 electrolytes is to date quite poorly understood, due to the difficulty of experimentally determining the degree of ion pairing as a function of salt concentration. Otherwise successful techniques such as conductometry[35] are increasingly difficult to use, due to both the increase in amount of ion pairing and to the fact that even simple contact ion pairs can carry charge. More precisely, from conductometric analysis alone of 2-1 electroltyes, it is not a priori obvious even what the basic relevant association equilibria are.[44] Thus, there will not be a focus in this thesis on uses of conductometric expressions to "fit" Λ vs c, as is often undertaken for 1-1 electrolytes.[19, 35, 45] The expressions developed (e.g. Fuoss-Hsia,[35] Lee-Wheaton[46] etc.), which include contributions from relaxation and electrophoretic effects, are not easily applied to 2-1 electrolytes where too many fitting variables are often introduced from the various possible charge carriers in solution.[35]

One technique which has been somewhat more successful than conductometry for multivalent electrolytes is dielectric relaxation spectroscopy (DRS),[35, 47] which studies the response of liquids or materials to applied electric fields. In particular, associated salt species present in solution show dipolar relaxation in the studied frequency range and hence their presence may be detected by DRS. Moreover, loss in solvent polarizability due to the bounding of free solvent molecules (e.g. loss of "free" solvent molecules to the primary solvation shell of ions) can also be measured. The frequencies of DRS used to study dipolar response are typically between 0.5 GHz and 100 GHz.

There is a significant body of work of DRS applied to low permittivity 1-1 liquid electrolytes, where DRS is often combined with conductometry and/or spectroscopic analysis such as Raman. These studies have elucidated precise infinite dilution association constants K_{A}^{0} between free ions and contact ion pairs, and the possible presence of triple ion formation.[17, 19, 48] Importantly, DRS has allowed researchers to explain the minima and subsequent increase in molar conductivity (see Figure 1.4) via the redissociation hypothesis. Here the associated salt increases the permittivity, leading to a decrease in the chemical potential of free ions due to the Born solvation contribution and an increase in their fractional population. It is worth noting that this explanation has been under contention, it has been proposed that increased molar conductivity is due instead to a higher fraction of (charged) triple ions.[48] It is the opinion of the author of this thesis, as well as Petrucci et

al.,[48] that the redissociation mechanism from permittivity is more likely than the strictly triple ion theory. Nonetheless, there is no reason to rule out that triple ions may still be present in larger quantities at higher concentrations, even as the permittivity increases and redissociation between free ions and contact ion pairs is occurring.

Interestingly, although there has been some work on DRS of multivalent electrolytes (e.g. in water or acetonitrile),[49, 50] DRS has not been previously applied to multivalent low permittivity electrolytes. This technique has a prominent place in this thesis for two important reasons: 1) it can provide two measurable signatures for each salt species (dielectric increase per species and relaxation frequency), which helps circumvent the pitfalls of multivalent conductometry analysis, and 2) it is the only experimental technique that can reliably provide the static permittivity (or dielectric constant) of liquid electrolytes, albeit with certain assumptions.

Figure 1.6 (left) shows a cartoon of a coaxial probe dipped in an electrolyte solution which allows measurements of the frequency dependent permittivity as a function of concentration. Solvent molecules present a dipole moment, for which the alignment can contribute to the polarizability $\mathbf{P}$, which is related to the electric field via the complex permittivity ($\mathbf{P} = \varepsilon_0(\varepsilon - 1)\mathbf{E}$).[47, 51] The electric field of a frequency f is set by the DRS instrument and the complex permittivity ε can be indirectly measured (see below) by the DRS instrument. In the cartoon (middle) a microscopic picture of polarizability is offered: solvent molecules show a smaller dipole and a faster relaxation than associated salt species, exemplified by contact ion pairs, which tend to show a larger dipole moment.

In DRS, the measurable quantity is the *total* complex permittivity η. The so-called permittivity ε' is equal to the real part of η. The imaginary part of η is a sum of two contributions, the first from ionic conductivity σ and the second from the dielectric loss ε'' (sometimes referred to as the imaginary component of the permittivity):[47]

$$\varepsilon''(f) = \eta''(f) - \frac{\sigma}{2\pi f \varepsilon_0} \tag{1.17}$$

The real and imaginary permittivity components ε' and ε'' are mathematically related.[51] With a proper underlying model, ε'(f) can be extrapolated to zero frequency $\varepsilon'(f = 0)$, which is defined as the static permittivity (or equivalently the dielectric constant). The permittivity of liquid electrolytes at lower frequencies than those investigated by microwave spectroscopy generally cannot be probed directly due to the high noise from the ionic conductivity. Figure 1.6 (right) shows an example DRS spectra for a solution with two detectable dipolar species: a solvent molecule, for which the dipole moment is shown with an arrow, and one associated salt species. The salt species shows a dipolar relaxation at lower frequency as it it larger and more sluggish in the solution. In the cartoon (middle), it is solvated by three solvent species. ε' and ε'' can be fit here with two Debye-type relaxation frequencies,[51] for which the equations are as follows:

$$\varepsilon' = \frac{\varepsilon_1}{1 + (f/f_1)^2} + \frac{\varepsilon_2}{1 + (f/f_2)^2} + \varepsilon_\infty \tag{1.18}$$

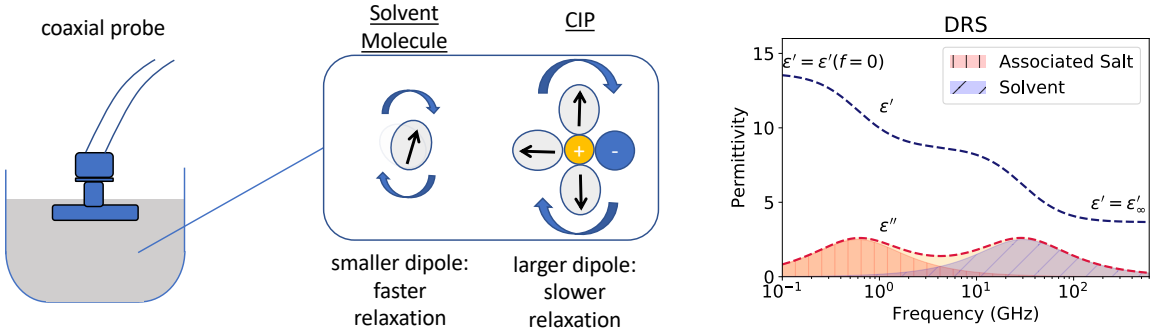

Figure 1.6: Cartoon of coaxial probe dipped in an electrolyte liquid (left). Inset cartoon of possible electrolyte species probed by DRS (middle). Example DRS spectra from an electrolyte (right).

$$\varepsilon'' = \frac{\varepsilon_1(f/f_1)}{1+(f/f_1)^2} + \frac{\varepsilon_2(f/f_2)}{1+(f/f_2)^2} \tag{1.19}$$

In the above equations, ε_i and f_i refer to the magnitude and frequency of the process i, which is assumed to be of Debye-type. For example, $i = 1$ and $i = 2$ can refer to the associated salt and solvent dipolar relaxation processes, respectively. The Debye type of relaxation is the simplest, and the main assumption is that the time derivative of the polarization is proportional to its actual value. A derivation of relaxation expressions for Debye-type processes is provided in Kremer et al.[51] ε_∞ refers to high frequency processes inaccessible by the equipment, generally related to electronic polarization. It is often the case that spectra of ε' and ε'' are obtained via DRS measurements but the chemical structures of the associated salt species contributing to the non-solvent features is not a priori evident. For example, a contact ion pair or a triple ion of a 2-1 electrolyte may have dipole moments of significant magnitude contributing to the dielectric spectra. Often, structural assumptions are made to decipher the likeliness of the various species that could be contributing to the DRS features.[50] Moreover, although solvated *free* ions do not hold a positive contribution to the DRS spectra, the binding of solvent molecules to the solvation of said ions generally results in a decrease in the solvent contribution to the dielectric spectra. Sometimes, this is referred to as electrostriction, or dielectric saturation. In the following sections it is shown how molecular dynamics simulations can be used to quantify contributions of various salt species to the dielectric spectra. Such simulations can help explain anomalous conductivity and redissociation in the studied low permittivity electrolytes via understanding of the speciation and its underlying thermodynamic driving forces.

Chapter 2

Modeling Dielectric Relaxation Spectroscopy using Classical Molecular Dynamics

2.1 Linear Response Theory and the Fluctuation Dissipation Theorem

The well-known particle physicist Michael Peskin famously said, "physics is that subset of human experience which can be reduced to coupled harmonic oscillators".[52] Thus, if we can explain the fluctuation dissipation theorem (FDT) for a spring we can at least understand the underlying physics. A simple harmonic oscillator, or a spring, is a theoretical physical object for which the force F required to displace a mass is directly proportional to the distance

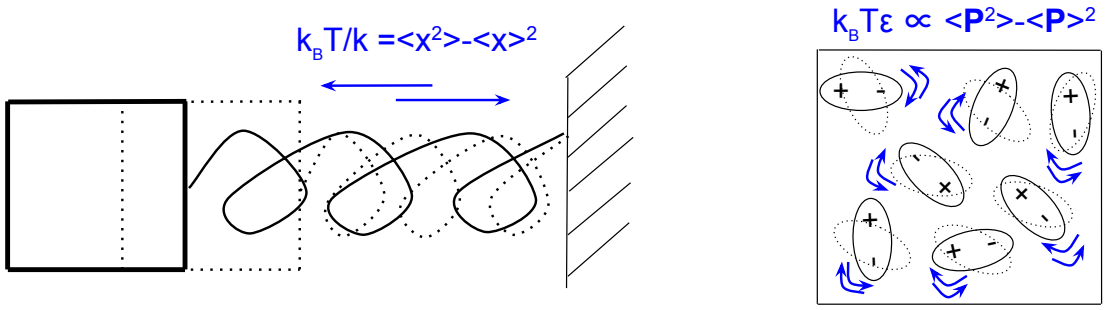

Figure 2.1: Cartoon of a spring on a wall (left) and cartoon of a liquid composed of molecules with a dipole moment (right). In each case there is a relation between the response function and fluctuations at equilibrium.

displaced, for which the proportionality constant is denoted by k.

$$F = kx \tag{2.1}$$

Importantly, this is the premise of linear response theory: that we perturb the system (in this case with a force F) which results in a change in the response (position) which is linear (a linearity described by the spring constant k). We know that under say, large forces, or far away from equilibrium, this relationship may not hold — perhaps a higher order polynomial would better describe the system. When we can adequately describe the system with a linear relation, such as equation 2.1, we are in the linear response regime. From this premise we can derive a result of the FDT via statistical mechanics.

For a canonical ensemble, at thermal equilibrium, we can write the following, where Z is the partition function, H the Hamiltonian, H_0 the Hamiltonian with no external force applied, and $\beta = (k_{\mathrm{B}}T)^{-1}$:

$$Z = \Sigma_i \exp(-\beta H_i) \tag{2.2}$$

In the above equation, H_i refers to the following:

$$H_i = H_0 - x_i F \tag{2.3}$$

Hooke's law can be cast as the following, where brackets denote ensemble average:

$$\langle x \rangle = \left(\frac{1}{k}\right) F \tag{2.4}$$

The position average can be related to Z via the following:

$$\frac{\Sigma x_i \exp(-\beta H_i)}{Z} = \langle x \rangle = \frac{1}{\beta Z}\frac{\partial Z}{\partial F} \tag{2.5}$$

Similarly the variance of the position can be written:

$$\frac{\Sigma x_i^2 \exp(-\beta H_i)}{Z} = \langle x^2 \rangle = \frac{1}{\beta^2 Z}\frac{\partial^2 Z}{\partial F^2} \tag{2.6}$$

The derivative of the average position with respect to the applied force can be related to the variance of the position:

$$\frac{\partial \langle x \rangle}{\partial F} = \frac{\partial}{\partial F}\left(\frac{1}{\beta Z}\frac{\partial Z}{\partial F}\right) = -\frac{1}{\beta Z^2}\frac{\partial Z}{\partial F}\frac{\partial Z}{\partial F} + \frac{1}{\beta Z}\frac{\partial^2 Z}{\partial F^2} = -\beta\langle x \rangle^2 + \beta\langle x^2 \rangle \tag{2.7}$$

Differentiation equation 2.4 with respect to force yields the following:

$$\frac{\partial \langle x \rangle}{\partial F} = \frac{1}{k} \tag{2.8}$$

Finally, using the above equation with equation 2.7 we can relate the inverse of the spring constant to the variance of the position of the spring at thermal equilibrium:

$$\frac{1}{k} = \beta(\langle x^2 \rangle - \langle x \rangle^2) \tag{2.9}$$

The above relationship holds for any applied force F, even when it is zero. And so, importantly, the above relationship holds for systems at thermodynamic equilibrium with no applied force. Consequently, if we know the variance in the position of the spring when it is at thermal equilibrium, we can directly calculate the spring constant. This is one embodiment of the fluctuation dissipation theorem: response functions (e.g. k) can be obtained via studying systems at thermal equilibrium. Many computational tools are well-suited for studying systems at thermal equilibrium, and thus can be used to obtain response functions without the need for directly simulating an external disturbance. Figure 2.1 (left) is a cartoon representation of the FDT, where thermal oscillations of a spring at thermal equilibrium, as quantified by the variance of position, can be used to characterize the spring constant k of a spring.

Electric Polarizability

Analogous to a spring being pulled by a force F displaced by an amount x, with a spring constant k, we can talk about a liquid of volume V being under an applied electric field $\mathbf{E}$, polarized by an amount $\mathbf{p}$ ($\mathbf{p}$ is the total dipole moment), with a dielectric constant ε:

$$\langle \frac{\mathbf{p}}{V} \rangle = \varepsilon_0(\varepsilon - 1)\mathbf{E} \tag{2.10}$$

ε_0 is the vacuum permittivity, here allowing the use of SI units. It is also assumed that the applied electric field and the total field are equal, which is discussed further below. For a dipole moment $\mathbf{p}$, we can arrive to a similar result of that of the spring:

$$Z = \Sigma_i \exp(-\beta H_i) \tag{2.11}$$

$$H_i = H_0 - p_i E \tag{2.12}$$

For an isotropic fluid, where x is a Cartesian coordinate, differentiating equation 2.10 with respect to E_x we obtain:

$$\frac{1}{V}\frac{\partial \langle p_x \rangle}{\partial E_x} = (\varepsilon - 1)\varepsilon_0 \tag{2.13}$$

Drawing an analogy directly to equations 2.8 and 2.9, and introducing a factor of 1/3 to account for the three spatial dimensions, we obtain:

$$\varepsilon_0(\varepsilon - 1) = \frac{\beta(\langle \mathbf{p}^2 \rangle - \langle \mathbf{p} \rangle^2)}{3V} \tag{2.14}$$

Thus, from the variance of $\mathbf{p}$ at thermal equilibrium (with no applied electric field) we can obtain the response $\varepsilon_0(\varepsilon - 1)$ to an applied electric field. Figure 2.1 (right) shows a cartoon

of the FDT where thermal rotations of molecular dipoles, as quantified by the variance of the dipole moment, are proportional to ε. A more rigorous derivation of this result involves the consideration of the effects of the boundary conditions, which introduces reaction field effects complicating the relationship between dipole fluctuations and the permittivity, as the applied electric field may be different than the total electric field. However, in this thesis, the boundary conditions at infinite distance are picked as "tinfoil" (perfect conductor), as is conventional in modern classical molecular dynamics. This allows for the equation 2.14 to remain valid.[53–56]

2.2 Dielectric Relaxation Spectroscopy and Molecular Dynamics Simulations

Following the derivation in the previous subsection, equation 2.14 can be rewritten as follows, where $\mathbf{p}$ is the dipole moment, (V,T) are the volume and temperature of the system and neglecting electronic polarizability:

$$\frac{\langle \mathbf{p}^2 \rangle - \langle \mathbf{p} \rangle^2}{3k_{\mathrm{B}}TV\varepsilon_0} = \varepsilon - 1 \tag{2.15}$$

The dipole moment can be directly calculated by summing over the charge q_i of atoms i multiplied by their position $\mathbf{r_i}$:

$$\mathbf{p} = \Sigma q_i \mathbf{r_i} \tag{2.16}$$

Computing the variance of the dipole moment, as shown in equation 2.15, allows us to compute ε provided there is no ionic conductivity, i.e. the salt species are completely associated into neutral aggregates (e.g. CIPs for 1-1 electrolytes). Thus, the above formalism can be used to calculate ε of solutions comprising both a solvent and salt, since the associated and neutral salt aggregates can be treated as neutral molecules. The treatment of polar species with an overall charge is discussed in the following chapter. Although it has been well established in the experimental literature that polar associated salt species contribute to the dielectric constant, molecular level calculations and simulations, e.g. work on classical molecular dynamics simulations[57] and theoretical methods[58] have generally overlooked this effect.

2.3 Case Study of Lithium Salts in Dimethyl Carbonate

In current "state-of-the-art" Li-ion battery electrolytes, the electrolyte is comprised of a polar (dissociating) co-solvent and a less-polar (viscosity reducing) co-solvent. For example, a blend of ethylene carbonate (EC, polar) with a linear carbonate (such as DMC, less viscous)

is quite common. More precisely, additives are generally used as they change the passivation films on the electrode in such a way that the cyclability is dramatically increased. These additives, due to their small weight percentage (e.g. 5%) generally do not affect bulk quantities such as fraction of dissociated salt or viscosity. However, it has been shown [59–61] that the dissociating co-solvent EC is not necessary. Although linear carbonates are much less polar, the molar conductivity and bulk conductivity of linear carbonate based electrolytes, at sufficiently high concentrations, are comparable to that of the EC-based blends. This is due to the redissociation effect which is explained below. EC-based electrolytes are still are used, as through their decomposition, they form a passivating film on the negative electrode (e.g. graphite) which allows better cyclability, at least compared to propylene carbonate (PC), a similarly structured solvent molecule. While linear carbonates do not form a functional passivating film, however, additives can preferentially decompose and passivate the negative electrode. Thus such "EC-free" electrolytes are viable, and are an active area of research for LIBs.[61] In this context, it is of interest to characterize such solutions and their bulk properties, and the work presented here allows us to connect the bulk permittivity, and at least to a qualitative extent the conductivity, to the atomic, molecular and supra-molecular structure of the electrolyte.

Classical Molecular Dynamics

Insights of molecular level interactions in liquids at a given temperature can be obtained through molecular dynamics (MD) simulations,[62] on a length scale of tens of nanometers and a timescale of ns to ms. In this thesis, *classical* molecular dynamics is employed, i.e. atoms have fixed charges as the system evolves with time. From the GROMACS manual, "A typical MD user chooses an initial molecular configuration, describes the atomic interactions and model physics, runs a simulation, and makes observations from the trajectory. Such simulations evaluate the millions of interactions of particles for billions of time steps."[63]

In this case study, the MD simulations were carried out with GROMACS software.[64] 1 Li^+, 1 anion, PF_6^- or 1 ClO_4^-, and 127 molecules of DMC were placed into a box of size 2.55 nm x 2.55 nm x 2.55 nm ($\simeq$ 0.10 mol/L) using Packmol.[65] Figure 2.2 (left) shows a box with the electrolyte herein mentioned. The DMC solvent atoms' charges were taken from Soetens et al.,[66] while the other necessary forcefield parameters were taken from the standard OPLS forcefield.[67, 68] For the ions, the charges were taken from Lopes and Padua (PF_6^-) and Doherty et al. (ClO_4^-).[69, 70] For this case study, ions were modelled with their full charge, e.g. Li^+ with a charge of +1. Since the density of electrolytes is generally not known a priori, and the initial configuration is not necessarily one at thermodynamic equilibrium, a series of MD simulations were carried out with various ensembles. First, a steepest descent minimization of the force field was used, followed by an isothermal-isobaric (NPT) ensemble (for at least 3 ns) which allowed relaxation to the correct electrolyte density. In this case a Berendsen barostat was used.[71] However, although the Berendsen barostat allows for relatively quick convergence to the correct pressure, it is not adequate to obtain response functions from MD simulations. After the NPT equilibration, steps of annealing (heating)

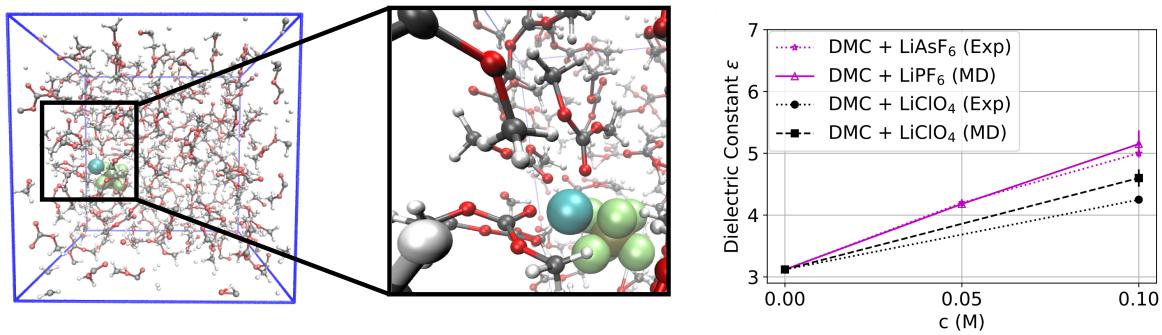

Figure 2.2: Snapshot of an MD simulation of 1 pair of $LiPF_6$ with 127 DMC molecules (left). Inset of associated salt species (middle). Dielectric constant as a function of salt concentration (right).

and quenching (cooling) were undertaken in the (canonical) NVT ensemble (a fixed density), to help avoid local minima traps in the potential energy surface. The heating step was one at 400 K for 2 ns, and the cooling step was one of three successive temperature drops from 400 K to 350 K to 298 K, each of 1 ns. Finally, a production run in the NVT ensemble, for at least 10 ns, was undertaken.[72] This final run allowed for the study of response functions, for example the calculation of the dielectric constant from the analysis of fluctuations of the dipole moment per unit volume at thermal equilibrium. From the study of the $LiPF_6$ in DMC system, the dielectric constant as a function of concentration can be obtained, as shown in the rightmost panel of Figure 2.2. Here, given the very high association constant,[19] it is assumed that the fraction of free ions in sufficiently small that their contribution to the dielectric constant can be neglected in this concentration regime. This approximation will be revised later in this thesis. In Figure 2.2 (right), the agreement of the computed to experimental dielectric constant is good, and many important conclusions can be drawn. First, this provides further evidence that the dielectric increase is in fact due associated salt species, as illustrated in Figure 2.2 (middle), which is occasionally overlooked.[58] Second, molecular dynamics simulations can provide quantitative interpretation of experimental DRS results. This is potentially very useful in the interpretation of DRS data for multivalent electrolytes, where multiple associated salt species may be present at once. In other words, the relationship between associated species and the dielectric properties of the electrolyte can serve as a powerful fingerprint. Generally the dielectric decrease from solvation of ions is well understood,[73] but the dielectric constant increase from associated salt is not as well established. Third, provided a model for speciation, we show that MD simulations have predictive power with respect to the dielectric constant for finite salt concentrations — in the case shown in Figure 2.3 the speciation model required only knowledge of K_A^0 and the Born radii.

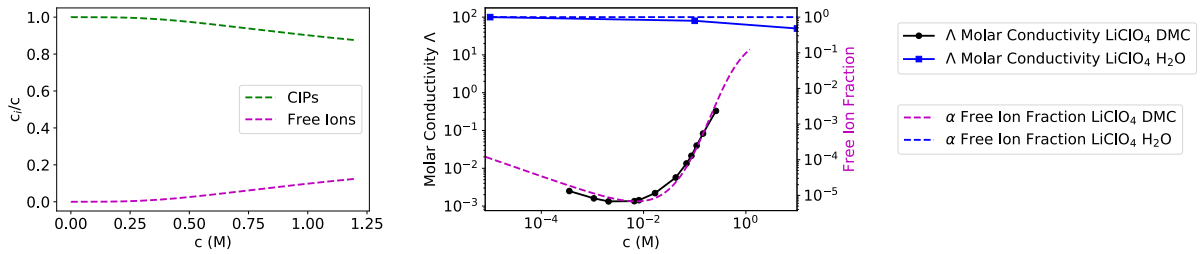

Figure 2.3: Speciation diagram of $LiClO_4$ in DMC (left) as calculated by Delsignore et al. and the same speciation diagram on log-log scale compared to the molar conductivity from Delsignore et al. (right)[19] In addition, data from $LiClO_4$ in water from Perron et al.,[74] with no ion pairing (see text), is shown for comparison.

Redissociation

Given $\varepsilon(c)$ and the thermodynamic parameters fit and assumed from Delsignore et al.[19], it is possible to plot the speciation diagram for $LiClO_4$ in DMC using equations 1.9, 1.10 and A.5. This speciation diagram is shown in Figure 2.3. The calculation parameters taken from reference[19] include the infinite dilution association constant K_A^0 and the Born radii of the free ions. Figure 2.3 (left) shows the fraction of free ions and CIPs as a function of concentration. In the shown concentration range, as $\varepsilon(c)$ increases due to the CIP presence, the fraction of free ions increases since the higher permittivity significantly reduces the activity coefficient of free ions. Figure 2.3 (right) shows the molar conductivity Λ in a log-log plot and it is compared the fraction of free ions (scale on right). Here, a minimum in the molar conductivity coincides with a minimum in the fraction of free ions at a concentration for which the permittivity starts to increase sufficiently to allow for redissociation of free ions. A cartoon of redissociation is shown in Figure 1.3 (middle row). In contrast, aqueous $LiClO_4$, for which the data is also shown, does not show any significant ion pairing[74] and the molar conductivity only decreases in the studied concentration range, with no redissociation taking place. Redissociation, as exemplified here for $LiClO_4$ in DMC, is also an important but often overlooked phenomenon for multivalent electrolytes, as will be shown in the following chapter.

2.4 Electronic Structure Methods

Electronic structure methods allow for the precise calculation of the electronic structure of certain molecules, ions, supramolecular and ionic complexes as well as electronic energy changes upon chemical reaction and conformation change. Such methods are often referred also referred to as *quantum chemistry*. The idea is that the energies of the molecular orbitals are calculated and populated via sophisticated approximation schemes to solve Schrodinger's

equation. This allows calculation of a total electronic energy based on an underlying atomic structure, which itself may be optimized self-consistently. The most commonly known electronic structure method is density functional theory (DFT), and specifically for organic systems, the most popular approach uses so-called hybrid-functionals, which combine elements of both DFT and Hartree-Fock (HF) based methods.[75, 76] Molecular dynamics simulations at the electronic structure level (AIMD, ab initio molecular dynamics) are well developed to study short-timescale chemical processes. However the computational cost is generally too prohibitive to allow study of DRS features at the timescales required ($\sim$ 1 ns). Electronic structure methods can nonetheless be useful to elucidate structure, conformation, and importantly, infinite dilution association constants K_{A}^{0}. In the previous subsection, a speciation diagram of $LiClO_4$ in DMC was shown (Figure 2.3). The MD-calculated dielectric increment per salt species, as well as the relevant (Born) radii and infinite dilution association constant K_{A}^{0} obtained from experiment[19] were used. However in many circumstances it may be impractical or impossible to find the relevant K_{A}^{0}, and electronic structure methods can allow for its calculation. Simply, the free energy of the reactants are subtracted from the products and the difference in free energy is related to K_{A}^{0}. There exist various schemes to account for the presence of the solvent. Arguably one of the most precise methods is to include the first solvation shell of the ions in addition to a structureless dielectric continuum around the (explicitly-)solvated species, where the use of a surrounding structureless dielectric medium is known as the continuum solvation model approach, or polarizable continuum model (PCM).[77] This approximation allows for a correction to the electronic energy from the solvation of salt species in solution. In addition, proper accounting for translational, rotational and vibrational degrees of freedom[78, 79] can allow for a total *free* energy of the species resulting in an improved accuracy of K_{A}^{0}.

Electronic structure methods by themselves are in principle well suited to obtain infinite dilution equilibrium constants K_{A}^{0} but by themselves cannot account for concentration effects, which is why a combined computational approach using both electronic structure methods (to obtain K_{A}^{0}, as well as the relevant Born and DH radii) in addition to molecular dynamics methods (to obtain the dielectric constant change as a function of concentration of salt species present, and the relevant activity coefficients) will be used in the following chapter.

Chapter 3

Case Study of a Magnesium Salt in Monoglyme and Diglyme

3.1 Introduction

One of the impediments towards improving Mg electrochemistry is the lack of the fundamental understanding of the governing electrochemical and physiochemical properties of the electrolyte. Although there exists a significant body of work focusing on transport properties, solvation and electrochemical stability,[8, 80–84] ion pairing and speciation remain poorly understood for commonly studied multivalent electrolyte systems,[85] despite their crucial importance to overall electrolyte behavior. A critical leap in understanding is needed in multivalent electrolytes to accelerate their development and achieve parity with lithium electrolytes.

Most Li-ion and specifically high permittivity electrolytes studied for electrochemical applications exhibit a decreasing molar conductivity as a function of concentration,[86] as ion pairing and viscosity increase. In contrast, multivalent electrolytes (which are generally prepared with solvents of low static permittivity,[8] e.g. $\varepsilon < 10$) can show an increasing molar conductivity Λ (concentration normalized conductivity) versus concentration. More precisely, in concentration ranges of electrochemical interest (e.g. 0.01 M to 1 M), the molar conductivity initially increases and eventually reaches a maximum at moderate concentrations. As discussed in the previous chapters, the initial increase in molar conductivity for multivalent low permittivity electrolytes may be due to a dramatic, more complex change in ion speciation as compared to monovalent high permittivity electrolytes.

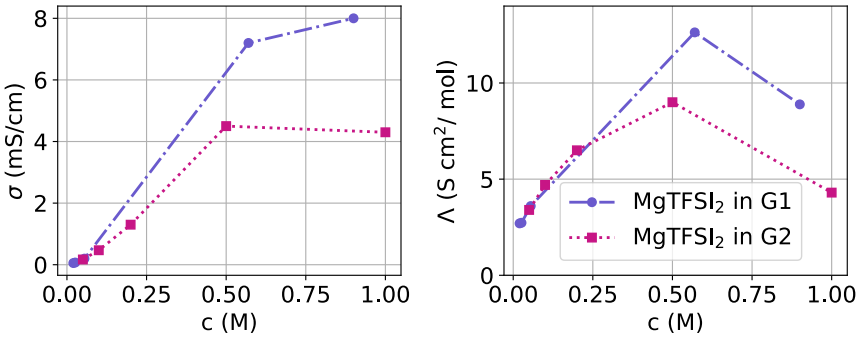

Figure 3.1: Measured conductivity (left) and molar conductivity (right) as a function of $MgTFSI_2$ salt concentration in G1 or G2 solvents.

Two representative low permittivity multivalent Mg^{2+} electrolytes are $MgTFSI_2$ (Mg bis(trifluoromethylsulfonyl)imide) in monoglyme (G1) and $MgTFSI_2$ in diglyme (G2), which are widely investigated electrolytes for use in electrochemical cells,[8] primarily due to their high conductivity, solubility and commercial availability.These anion-solvent combinations are also widely utilized for Li-oxygen and Li-sulfur electrochemistry.[87–89] However, $MgTFSI_2$ in ethers requires additional salt (e.g. $MgCl_2$) in order to allow plating and stripping at high Coulombic efficiencies.[8] Nonetheless, the present work will focus specifically on $MgTFSI_2$ in ethers without additional salt, as even such simple electrolytes, which are the subject of intense research and interest,[81, 82, 84, 90, 91] are still poorly understood in terms of salt speciation[92] and bulk thermodynamic properties.[93]

For both $MgTFSI_2$ in G1 and G2, concentration dependent molar conductivity deviates from that of high permittivity electrolytes (Figure 3.1).[93, 94] The molar conductivity increases with concentration, indicating non-conventional behavior: typically (e.g. for high permittivity solvents) molar conductivity decreases as a function of concentration in the dilute limit following Kohlrausch's law,[15] and at concentrations ~ 0.5 M following, among other factors, significant viscosity and ion pairing increases.[95] The molar conductivity increase for G1 and G2 suggests that ion pairing decreases[91] (i.e. the population fraction of charge carriers is increased), contrary to what would be expected from simple predictions based on the law of mass action.

Salama et al. suggested from diffusion and Raman measurements that $MgTFSI_2$ in G1 exists primarily as free ions, independent of concentration,[93] a finding under contention[84, 85]. Similarly, Kubisiak and Eilmes[90] reported MD simulations which showed strictly solvent-solvated Mg^{2+} from 0.1 M to 1 M $MgTFSI_2$ in G1. Sa et al. studied $MgTFSI_2$ in G2, and found (an unusual) increase in diffusivity of salt from 0.1 M to 0.7 M by an order of magnitude, which is suggested as resulting from a "complicated solution environment at different ionic strengths".[94] Using MD they found a significant presence of SSIPs or free ions, and monotonically increasing ion pairing with concentration from 0.2 M to 2 M. Unfortunately,

the results from Salama et al., Kubisiak and Eilmes and Sa et al. are not consistent with the relevant molar conductivity increase. Lapidus et al.,[84] via X-ray and MD studies of 0.4 M $MgTFSI_2$ in G2, found approximately half of Mg^{2+} was free, with the remaining split into contact ion pairs (CIPs) or neutral triple ions. Kimura et al., who studied $MgTFSI_2$ in triglyme via conductivity and Raman, suggested a shifting equilibrium between solvent-separated ion pairs (SSIPs) and free ions as concentration is varied to explain the increasing molar conductivity, without providing a physical motivation for such a mechanism.[91] The differences in the aforementionned interpretations and suggestions illustrate that no clear consensus has yet emerged regarding the speciation in low permittivity multivalent systems.

We hypothesize that the interplay between ion pairing and molar conductivity can be rationalized via *redissociation*.[19, 48, 96–98] In low permittivity electrolytes, associated salt species tend to form due to the strong electrostatic interactions compared to polar solvents.[35] If these associated species are endowed with a significant dipole moment, they will increase the total permittivity via an increase in the orientational polarizability and favor a larger population of dissociated salt species as concentration increases, a phenomenon termed redissociation.[48, 97, 99] Previous work on studying the interplay between permittivity increase and ion association has focused on monovalent salts.[19, 48, 97–101] To the best of the authors' knowledge, redissociation has not been analyzed or proposed for non-aqueous multivalent systems, despite the inherently stronger electrostatic interactions present.

Characterization of ion pairing for multivalent liquid electrolytes systems is quite challenging due to the strong interionic interactions in solution: many conventional techniques such as conductometry are often not directly applicable,[35] and the challenges are compounded for low permittivity systems. In order to evaluate the redissociation hypothesis for low permittivity multivalent electrolytes, we herein use a multiscale computational model (MSM) to predict permittivity and salt speciation as a function of concentration. To verify the results, we undertake Raman and dielectric relaxation spectroscopy (DRS). While previous work on combined permittivity and speciation diagrams have used a posteriori experimental data,[50, 98, 102] the current MSM is entirely theoretically and computationally based, and relies on experimental input only for validation. Furthermore, a significant number of dielectric relaxation studies have been carried out on monovalent low permittivity systems,[19, 97, 100, 101] as well as some high permittivity multivalent systems,[50] however none yet on multivalent low permittivity electrolytes — the subject of the present work.

For a system with divalent cations and monovalent anions, the concentration association constant K_A directly provides the concentration ratio of associated monocationic contact ion pairs $c_{\mathrm{CIP},+}$ to free ions c_{++} and c_{-} via the following relationships:[35]

$$K_\mathrm{A}(c) = \frac{c_{\mathrm{CIP},+}}{c_{++}c_{-}} = K_\mathrm{A}^0 \frac{y_{\mathrm{DH},++}y_{\mathrm{DH},-}}{y_{\mathrm{DH,CIP},+}} f_{\varepsilon,\mathrm{A}} \tag{3.1}$$

In the above equation, the thermodynamic association constant K_A^0 is introduced, as well as the concentration activity coefficients of the multivalent cation, anion, and contact ion pair $y_{\mathrm{DH},++}$, $y_{\mathrm{DH},--}$ and $y_{\mathrm{DH,CIP},+}$ and the permittivity correction term $f_{\varepsilon,\mathrm{A}} = \frac{y_{\mathrm{Born},++}y_{\mathrm{Born},-}}{y_{\mathrm{Born,CIP},+}}$. As introduced in section Chapter 1, K_A^0 accounts for specific short range interactions while

the activity coefficients $y_{\mathrm{DH},i}$ as well as the permittivity correction term $f_{\varepsilon,\mathrm{A}}$, account for long-range non-specific electrostatic interactions.

Assuming only free ions and contact ion pairs then the following concentration conservation equation can be written:

$$c = c_{++} + c_{\mathrm{CIP},+} \tag{3.2}$$

Moreover, charge neutrality imposes the following condition:

$$2c_{++} + c_{\mathrm{CIP},+} = c_{-} \tag{3.3}$$

In the present work, K_{A}^{0} is obtained through first-principles electronic structure calculations within a continuum solvation model enhanced with an explicit first solvation shell for the multivalent cation (see Methods, section 3.4). For low to moderate concentrations (e.g. up to 0.7 M), a Guggenheim-type equation is often used for activity coefficients,[50] where the first term is the Debye-Huckel expression, employed in the present work, as follows:[24, 50]

$$\frac{y_{\mathrm{DH},++}y_{\mathrm{DH},-}}{y_{\mathrm{DH,CIP},+}} = 10^{\frac{-4A_{\mathrm{DH}}\sqrt{I}}{1+B_{\mathrm{DH}}\alpha_{\mathrm{DH}}\sqrt{I}}} \tag{3.4}$$

In the above equation, the symbols have their typical significance,[24, 50] where B_{DH} is the Debye-Huckel term, α_{DH} is the distance of closest approach, A_{DH} is the Debye-Huckel parameter and I is the ionic strength (see Appendix for further details). While Guggenheim-type expressions also include linear and higher order terms in ionic strength for the ions' chemical potential, here we assume that additional terms to the standard Debye-Huckel expression impact first order due to changes in permittivity.[26, 27] Thus, the role of such terms is fulfilled by $f_{\varepsilon,\mathrm{A}}$, described above. Hence, we neglect any higher order corrections.

If the permittivity of the electrolyte remains fairly constant as a function of concentration, then $f_{\varepsilon,\mathrm{A}}$ would equal unity. However, if the permittivity changes appreciably, as it tends to for low permittivity electrolytes, then the following phenomenological equation can be used,[19] where b is a positive phenomenological constant:[19]

$$f_{\varepsilon,\mathrm{A}} = \exp\left(\frac{-b}{\varepsilon(c=0)} + \frac{b}{\varepsilon(c)}\right) \tag{3.5}$$

With increasing concentration of charged species, the y_i charged species activity coefficients decrease, hence competing with the mass action law which promotes association. If the permittivity increases, then this will act as an additional driving force for reduced association (and increased association if the permittivity decreases). Together, equations 3.1, 3.2, 3.3, 3.4 and 3.5 allow for construction of speciation diagrams from first principles calculations provided $\varepsilon(c)$ is known in the desired concentration range.

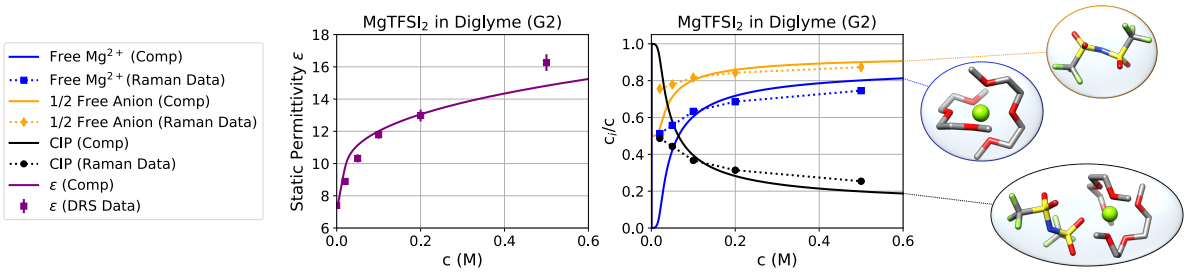

Figure 3.2: Permittivity (left) and speciation diagram (right) of $MgTFSI_2$ in G2 at 25°C. Computed species fraction c_i/c is shown with solid lines, except for the anion which is shown for 0.5 c_i/c. Species in question are illustrated in bubbles.

Concentration-Dependent Static Permittivity

$$\varepsilon(c) = \varepsilon(c=0) + \sum_i \Delta\varepsilon_i c_i + O(c_i c_j) \tag{3.6}$$

In equation 3.6, the concentration-dependent permittivity is equal to the permittivity of the neat solvent $\varepsilon(c=0)$ in addition to the dielectric increment per species $\Delta\varepsilon_i$ multiplied by the concentration of said species c_i. $\Delta\varepsilon_i$ is here independent of concentration, and it is also assumed that higher order terms can be neglected. If coupled to equations 3.1-3.5, then the total permittivity can be calculated as a function of concentration, provided each $\Delta\varepsilon_i$ is known. As described in the Methods (section 3.4), in Chapter 2 and in a previous publication,[57] $\Delta\varepsilon_i$ can be calculated from classical molecular dynamics simulations.

3.2 Results and Discussion

Figure 3.2 (left) shows the static permittivity (dielectric constant) as a function of concentration and the speciation as a function of concentration (right) for $MgTFSI_2$ in G2. The static permittivity is computed to increase from 7.4 (neat G2) to 14.8 (0.5 M), while it is measured to increase from 7.4 to 16.2. There is good agreement throughout the studied concentration range (0.02 M to 0.5 M). The error bars are a consequence of the fitting procedure required to extract the static permittivity values from the frequency dependent spectra (see Methods, section 3.4). The tendency of the permittivity to increase with concentration is different than salts in typical high permittivity electrolytes (e.g. NaCl in water) where the dielectric constant typically decreases with concentration due to the loss of free solvent molecules bound into the solvation shell of free ions, thus reducing the orientational polarizability of the solution.[13] Here, the increase in permittivity with concentration unequivocally indicates that associated species, e.g. CIPs, which hold a strong dipole moment, are present in appreciable quantities in the solution.

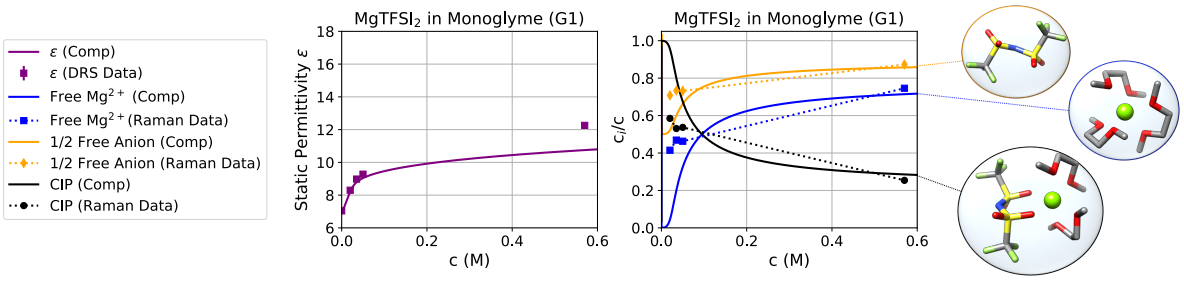

Figure 3.3: Permittivity (left) and speciation diagram (right) of $MgTFSI_2$ in G1 at 25°C. Computed species fraction c_i/c is shown with solid lines, except for the anion which is shown for 0.5 c_i/c. Species in question are illustrated in bubbles.

The speciation inferred from the Raman analysis of TFSI ion pairing is in good agreement with the computed values (Figure 3.2, right). Here, the population fraction of free ions increases with concentration, while the fraction of associated species, e.g. CIPs, decrease, consistent with the molar conductivity increase.

Table 3.1 shows the computed dielectric increment per salt species, which was used in the MSM. We note that the presence of free ions tends to lower ε, however, the decrease is much less than the increase in ε from CIPs.

solvent	$\Delta\varepsilon_{++}(\frac{1}{\mathrm{M}})$	$\Delta\varepsilon_{-}(\frac{1}{\mathrm{M}})$	$\Delta\varepsilon_{\mathrm{CIP},+}(\frac{1}{\mathrm{M}})$	K_{A}^{0}
G2	-11	-3.0	147	5.2×10^8
G1	-13	-2.7	72	3.6×10^8

Table 3.1: Computed dielectric increment per mole of species, and computed K_{A}^{0}.

Figure 3.3 shows the static permittivity as a function of concentration (left) and the speciation as a function of concentration (right) for $MgTFSI_2$ in G1. The static permittivity is computed to increase with concentration, from 7.0 (neat G1) to 10.8 (0.57 M salt in G1), and is measured to increase from 7.0 to 12.3 by DRS, in general agreement. No data points were obtained between 0.05 M and 0.57 M due to the miscibility gap in the electrolyte[93] (see Methods, section 3.4).

The rightmost plot of Figure 3.3 shows the speciation as a function of concentration. The Raman analysis of associated $TFSI^-$ populations is consistent with the trends: the fraction of associated salt (CIPs) generally decreases with concentration and fraction of free ions increases with concentration, qualitatively similar to the $MgTFSI_2$ in G2 system. The high concentration population experimental data (0.57 M) are within 5 % of the computed values, but the lower concentrations do not show such agreement. The disagreement suggests that either the computed K_{A} is overestimated in the lower concentrations, or there could be

presence of higher order aggregates (e.g. solvent separated ion pairs, triple ions), which is discussed futher below. The Raman data points indicate a slight increase in ion pairing from 0.035 M to 0.05 M by 0.6 %. However, the error estimate for Raman inferred populations due to instrument noise is 6 % in the lowest concentration (0.02 M), and otherwise the ion-paired populations generally decrease with increasing concentration (error bars are not displayed here for visual clarity, see Appendix). Thus, the emphasis is here placed on the general trend of decreasing ion pairing with concentration.

At high concentrations, the permittivity of G2 electrolytes is higher than that of G1, despite a similar fraction of ion pairing according to Raman spectroscopy, and this highlights an important difference in CIP structure tendencies. As shown in Table 3.1, CIPs in G2 show a much larger dielectric increment increase than G1 (147/M versus 72/M), which allows the electrolyte to reach a higher static permittivity despite having a similar fraction of CIPs. The larger dielectric increment is due to a preference for the more polar monodentate configuration of the CIP in G2, in contrast to the bidendate majority configuration of the CIP in G1 (see inset illustrations in Figure 3.3). In the model used herein, we approximate the majority dentation as the only ion-pair structure, although likely some admixture of both dentations is present in both liquids. The K_A^0 values for both studied systems (G2 and G1) are on the order of 10^8 (Table 3.1), while for high permittivity electrolytes typically K_A^0s are much smaller (e.g. on the order of 10^2).[50] The concentration-dependent K_As are dramatically lowered from the permittivity increase, a phenomenon specific to low permittivity systems.

As part of the presented results, a few possible sources of errors should be considered and discussed. First, the assumption of a concentration-independent interionic distance parameter α_{DH} could in principle be improved.[46] In this work we derive α_{DH} as the sum of radii[103, 104] of a CIP and an anion, providing a reasonable value for a multivalent Mg^{2+} system.[46] Second, assuming CIPs as the only associated species is certainly an approximation, especially in the low concentration regime. For previous multivalent systems, SSIPs were shown to be present at low concentrations (below 0.2 M),[50] which may explain the disagreement at low concentration for the $MgTFSI_2$ in G1 and G2 systems. Unfortunately, the low frequency limit of DRS, and the Raman analysis methods (which cannot distinguish between free ions and SSIPs, and show higher errors at lower concentrations), preclude us from directly investigating the presence of SSIPs in this work. Moreover, the agreement between the MSM with DRS and Raman analysis at higher concentrations supports the assumption of CIPs as the majority associated species at higher concentrations.

Importantly, for both G1 and G2 electrolyte systems, the calculated values for permittivity and speciation and the respective experimental data are consistent with the redissociation hypothesis. More precisely, the permittivity increase, in addition to the increasing ionic strength, which enhances screening of free ions and lowers their chemical potential (via equation 3.4), explains the dramatic stabilization of free ions at higher concentrations.

3.3 Conclusion

In contrast to high permittivity Li-ion electrolytes, multivalent electrolytes for battery applications, which generally use low permittivity solvents, show an increasing molar conductivity versus concentration. To improve our understanding of the complex speciation in these liquids, we use modeling and DRS, to establish an increase in static permittivity as a function of salt concentration in $Mg(TFSI)_2$/G1 and G2 electrolytes. Furthermore, the speciation diagrams constructed from the multi-scale modeling methodology show an increase in the fraction of dissociated species with concentration, which is confirmed experimentally by Raman spectroscopy. The combined evidence strongly indicates that polar contact ion-pairs that form at low concentration trigger a redissociation mechanism, leading to an increase in free, charge-carrier ions at higher concentrations. For G1, the dramatic change in speciation from redissociation may also play a role in the miscibility gap from 0.05 M to 0.57 M.[93] Furthermore, the current results suggest that for multivalent low permittivity electrolytes, redissociation is a non-specific effect (i.e. independent of the salt chemistry), provided a considerable population of strongly polar associated species persists. Preliminary measurements indicate that many Mg^{2+} and Ca^{2+} electrolytes of interest exhibit increasing molar conductivity with concentration, and further investigations linking these observations to the attendant cluster structures and populations will be the subject of future work. Finally, the ability to tune redissociation — and therefore speciation and transport — via designer salt additives remains a viable path forward.

3.4 Methods

Computational and Theoretical Details

Infinite dilution association constants K_{A}^{0}, shown in Table 3.1, were calculated via first principles quantum chemistry calculation. Hybrid-DFT calculations were undertaken with Gaussian 016 software[105] using ωb97x-d[75] with the def2tzvp basis,[106] with a continuum solvation model[77] (CSM) using the neat solvent permittivity, as well as an first explicit solvation shell for cations. Before geometry optimization via ab initio methods, initial configurations were picked via conformational analysis using MacroModel[107] and an OPLS-based force field,[68] where structures with dentation matching those from the classical molecular dynamics were picked. In order to correct for spurious contributions of low frequency modes to the vibrational partition function, Truhlar's[78] correction was applied using Patton's code.[108] $f_{\varepsilon,\mathrm{A}}$ was calculated using the optimized geometries of the neat solvent and then single point calculations as the permittivity of the CSM is varied. A function as described by equation 3.5 was fit (further details in the Appendix). This yielded an analytic function allowing the computation of the correction to the association constant due to the change in permittivity.

In order to calculate $\Delta\varepsilon_i$, molecular dynamics calculations were undertaken with GRO-

MACS,[64] with details following those of a previous manuscript.[57] Briefly, each simulation held a single salt species in a box of solvent, such that the concentration was 0.1 M. In order to include the contribution of salt species to the total permittivity via the fluctuation dissipation theorem, the dipole of the salt species had to be drawn and included in the total polarization. This was undertaken with in house code, described and provided in a previous publication.[57] As was necessary, certain of the simulations carried an overall charge, which, for which the GROMACS software provided a correcting background homogeneous charge.[64, 109] For charged associated salt species, the net charge was subtracted at the center of mass.[64] Briefly, the dipole moment P of the associated salt species can be written as follows:

$$P_{\text{salt species},x} = \Sigma_{\text{ions}} q_{\text{ions}} r_x \tag{3.7}$$

In the above equation, "ions" refers to the atomic point charges of the salt species and x the given cartesian direction. If the associated salt species has an overall charge, then the center of mass (COM) charge can be subtracted:

$$P'_{\text{salt species},j} = P_{\text{salt species},j} - r_{\text{COM}}(\Sigma_k q_k) \tag{3.8}$$

Experimental Details

The experimental measurements for ionic conductivity, DRS, and Raman were carried out by collaborators, who are co-authored on the manuscript cited at the start of this chapter.[20] The analysis and fitting of the experimentally collected DRS spectra was nonetheless undertaken as a collective effort. Electrolyte solutions for ionic conductivity, DRS, and Raman measurements were prepared in an argon-filled glove box with $H_2O < 1$ ppm and $O_2 < 0.1$ ppm (MBraun). The solvents G1 (1,2-dimethoxyethane) and G2 (diethylene glycol dimethyl ether) were purchased in anhydrous form from Millipore-Sigma, distilled, and stored over 3 Å molecular sieves with activated alumina. $MgTFSI_2$ (Solvionic, 99.5%) was dried under vacuum at 170°C for a minimum of 48 h prior to use. It was found that the dissolved $MgTFSI_2$ salt imparted a non-trivial solution volume increase over that of the pure solvents and thus careful measurement of overall solution volume was required to achieve accurate molarity values. This is particularly important for solutions of moderate to high concentration. Consistent with a previous report, it was found that $MgTFSI_2$/G1 solutions exhibit a significant miscibility gap between ∼0.05 M and ∼0.57 M, precluding measurements at intermediate concentrations.[93]

Solution ionic conductivities were measured in the aforementioned glove box using AC impedance incorporating a home-made conductivity probe consisting of two parallel Pt electrodes. The cell constant of this conductivity probe was periodically calibrated in KCl solutions of various concentrations to ensure measurement accuracy.

Raman spectroscopy was performed in sealed vials on a WITec Confocal Raman Microscope using a 532 nm excitation laser. The TFSI speciation was measured through careful

spectral fitting of the TFSI breathing mode region ($\sim$740 cm^{-1}) using Gaussian/Lorentzian line shapes, similar to published methods.[83, 110] Select examples are shown in the Appendix.

Dielectric spectra were measured in glass vials using an immersed slim-form coaxial probe (Keysight N1501A) and vector network analyzer (Keysight P9375A) over a frequency range from 0.5 to 26.5 GHz. Multiple measurements were made to ensure repeatability, and various immersion depths were tested to confirm the absence of associated artifacts. Calibration was maintained and periodically refreshed through an ECal module (Keysight N7555A). A three-point calibration was performed before each DRS series using air, short-circuit, and tetrahydrofuran.[111] During spectral acquisition, the samples were briefly exposed to air ($<$ 1 min). However, no subsequent changes were observed in DRS measurements repeated after long-term exposure to air, indicating that the measurement is insensitive to electrolyte air exposure over these time-scales. DRS data were fit with two Debye relaxations for G1 electrolytes, and one Cole-Cole and one Debye relaxation for G2 electrolytes (further details in the Appendix).[51, 112, 113]

Chapter 4

Case Study of a Calcium Salt in Tetrahydrofuran

4.1 Calcium Electrodeposition

Calcium (Ca) electrochemistry research is much less advanced than its lithium and magnesium counterparts. A current scientific effort is underway to identify electrolytes that could reversibly electroplate calcium metal, which would pave the way to a potential calcium battery. The latter would also require a viable positive electrode (cathode),[2, 114–120] which is not discussed further in this chapter.

An in depth study by Aurbach et al. in 1991[121] found that for a wide variety of common anions and solvents, calcium electrolytes do not allow reversible electrodeposition, due to the formation of an ionically insulating surface film. Despite Aurbach's work showcasing the difficulties of enabling Ca electrodeposition, this field has found a recent renaissance due to the discovery of partially viable electrolytes. First, Ponrouch et al. in 2016[122] reported that 0.3 M $Ca(BF_4)_2$ in EC/PC mixtures could reversibly electroplate, however only at high temperatures (75°C or above) and with notable electrolyte decomposition products found on the Ca metal electrode. The role of high temperature remains unclear, it may have eased the transport through the electrolyte-electrode interphase domains formed by these products, or perhaps it allowed for otherwise difficult desolvation of the electroactive cation. Later work by Biria et al.[123] reported reversible deposition at relatively high efficiencies (95 %) at room temperature for this electrolyte, although the current density was fairly low and the necessary overpotentials considerable.

In 2018 Wang et al.[124] found that 1.5 M $Ca(BH_4)_2$ in THF could be reversibly plated with relatively high efficiencies (96 %). They highlighted the need for still higher efficiencies (above 99.98 %) for Ca electrochemistry to be a viable contender commercially. They suggested that a better surface film could allow such high efficiencies. The surface film identified on the metal anode was comprised in part of CaH_2, which did not sufficiently passivate the electrode. Moreover, the oxidative stability limit of $Ca(BH_4)_2$ may not allow for a sufficiently

large electrochemical window.[2, 125]

Shywamsunder et al. in 2019[126] found that the large BHFIP anion (tetrakis (hexafluoroisopropoyloxy) borate) could be used to allow reversible electroplating at moderate efficiencies (92-95 %). This design choice was inspired by work on Mg electrolytes,[125] where the guiding principle was to reduce ion pairing via the use of large anions. For $Ca(BHFIP)_2$ in G1, the ability to reversibly electrodeposit calcium has been attributed to the low anion-cation interaction strength in addition to the sufficiently low solvent-cation interaction strength.[127]

In the above mentioned systems, it is an open question what properties of an electrolyte are limiting the efficiencies for reversible plating and stripping. In order to identify such properties, one approach is to first identify the solvation environment of the calcium ion in solution. This is essential in order to understand deposition, desolvation and charge delivery at the nanosocale. The description of solvation and identification of speciation is undertaken herein for the $Ca(BH_4)_2$ in THF system in the following section. Preceding the following section, the following subsection briefly discusses cyclic voltammetry in the context of Ca electrochemistry.

Introduction to Cyclic Voltammetry

In this section we provide a brief introduction to cyclic voltammetry (CV), which refers to an electrochemical measurement where the potential is varied linearly and cyclically with time. We refer to Bard and Faulkner for a more complete introduction.[128] CV may be best known for its application to diffusion-limited charge-transfer reactions,[128] such as for an electrolyte solution containing ferrocene. However, the scope of the technique is much broader, including information about reversible plating and stripping of metal electrodes, and the study of complicated electrode reactions. It should be noted that CV alone cannot definitely prove that plating and stripping is occurring, which is why it is generally undertaken in combination with other techniques, such as microscopy.[129] Figure 4.1 a) shows a schematic of a three electrode cyclic voltammetry experiment. A working electrode (WE) is the electrode where the electrochemical reaction or reactions under study take place, if they do. In order to close the circuit, a power supply provides the necessary current to or from the WE and from or to the counter electrode (CE). To monitor the voltage of the WE, voltage is measured between the WE and a reference (or pseudo-reference) electrode RE, in this case with a voltmeter. Here, all three electrodes are immersed in an electrolyte of a given composition. In Figure 4.1 b), the voltmeter and DC power supply are generally replaced by a potentiostat, as it accomplishes the same as the previously mentioned voltmeter and DC power supply. Here, following the setup of Aurbach et al.[121], the WE, CE and RE all are Ca. The WE is generally smaller than the CE and its area is well known in order for the experiment to be reported as a function of current density. Moreover, a larger CE, in the case of Ca, may assure the CV electrochemist that if there is electrochemical passivation occuring from the studied reaction, the WE will be passivated first before the CE due its much smaller area. In Figure 4.1 c), a CV plot of $LiClO_4$ in THF is shown.[121] Following the interpretation by

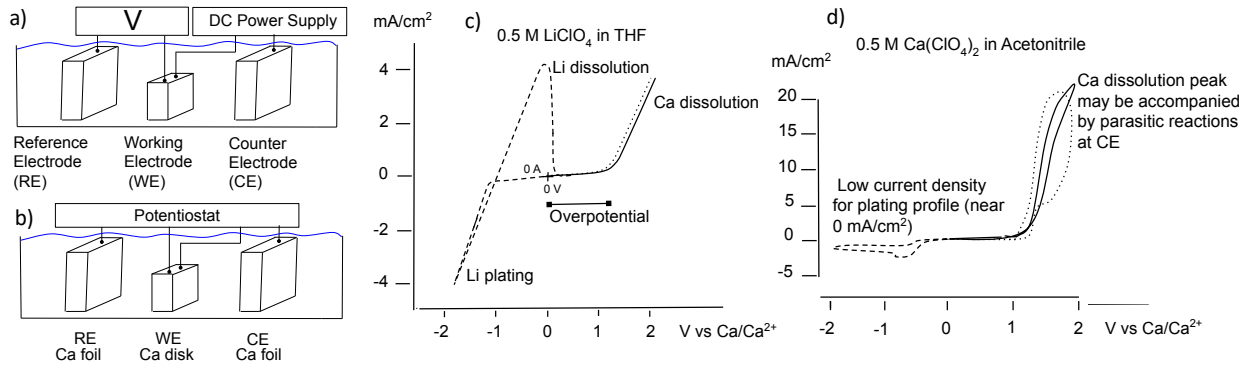

Figure 4.1: a) Setup schematic for a CV measurement. b) Same schematic with the the potentiostat playing the role of both voltmeter and power supply, with all electrodes as Ca as in Aurbach et al.[121] c) Cyclic voltammogram for $LiClO_4$ in THF with the setup of b). d) Cyclic voltammogram on Au for $Ca(ClO_4)_2$ in acetonitrile with the setup of b). Data for c) and d) digitized from Aurbach et al.[121]

Aurbach et al.,[121] the bottom (negative current) feature is in the lithium plating on the Ca WE. As the voltage is increased, a positive current is eventually reached, where Li (which was previously plated from the electrolye onto the WE), starts dissolving back into solution, until there is no plated Li left on the WE, at which point the current drops to 0. As the voltage is increased above 0 vs Ca/Ca^{2+}, there is a feature attributed to Ca dissolution, i.e. dissolving from the WE into solution. Since this feature is much above 0 V vs Ca/Ca^{2+}, which is the equilibrum thermodynamic potential (of plating and stripping), the difference between the *onset* and the equilibrium voltage is often described as the *overpotential*. Application of rigorous models of electrochemical reactions may lead to different values of overpotential [24, 128] as they account for concentration and surface overpotentials and the Ohmic voltage drop in solution. Nonetheless, the non-zero overpotential, as seen by inspection in this example, shows that the Ca dissolution does not occur in solution without difficulty.

Figure 4.1 d) shows the CV of $Ca(ClO_4)_2$ in acetonitrile with a Ca WE. Here, the feature at negative voltage is of near 0 current, suggesting that plating is difficult or impossible with this electrolyte. At higher voltage (above 0 V vs Ca/Ca^{2+}), there is a possible dissolution feature. However, since the dissolution and plating are not reversible, it is unclear what reactions are occurring at the CE (e.g. irreversible decomposition of the solvent). The different line types in Figures 4.1 c) and d) refer to different CV cycles, following the legend of Aurbach et al.,[121] where the data was digitized from.

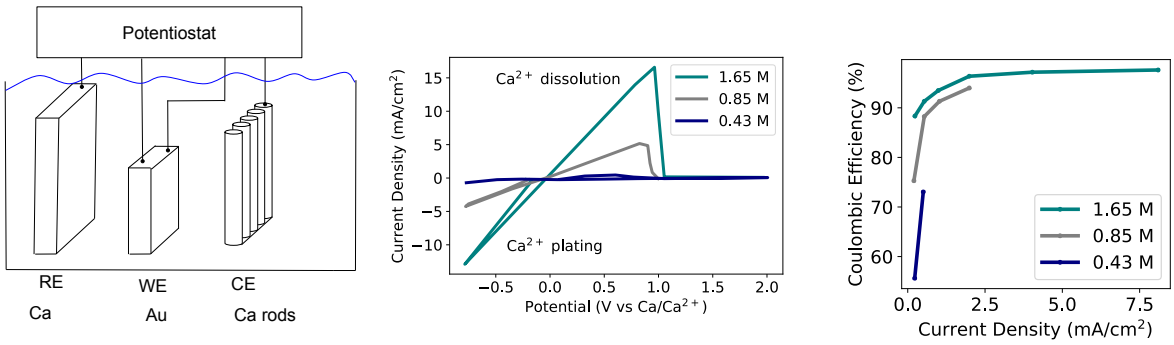

Figure 4.2: Setup schematic for CV experiments of $Ca(BH_4)_2$ plating on a Au WE. (left) cyclic voltammogram of $Ca(BH_4)_2$ in THF for three different salt concentrations (middle). Coulombic efficiency as a function of current density (right), where higher salt concentrations yield significantly higher efficiencies. Data for middle and right panels digitized from Hahn et al.[130]

4.2 $Ca(BH_4)_2$ and $Mg(BH_4)_2$ in Tetrahydrofuran

Figure 4.2 (left) shows a schematic of the three electrode cell setup used to investigate $Ca(BH_4)_2$ in THF electroytes. The working electrode is composed of gold (Au) while the counter electrode is comprised of calcium rods, which allow for a high surface area. Figure 4.2 (middle) shows the CV of $Ca(BH_4)_2$ in THF at different salt concentrations. As the concentration is increased from 0.43 M to 0.85 M to 1.65 M, the current densities attained are much higher. Figure 4.2 (right) shows the Coulombic efficiency as a function of current density, obtained via galvanostatic charging (i.e. constant current as opposed to a linear voltage sweep). The data was digitized from Hahn et al.[130] The efficiency increase with current density suggests that time-dependent parasitic reactions are significant in this system, and are likely related to the evolution of a surface film. To analyze and understand the underlying electrochemical behavior, the electrolyte transport properties are useful. These can help infer details about the solvation environment present in the liquid electrolytes as well as give direct information on transport limitations. The conductivity of various low permittivity multivalent electrolytes is shown in Figure 4.3, including $Ca(BH_4)_2$. The conductivity increases significantly from low to high concentrations for the latter. Moreover, there is an anomalous increase in molar conductivity for the low permittivity multivalent electrolytes, whereas a 1-1 aqueous electrolyte (e.g. LiTFSI in water) shows decreasing molar conductivity (see Chapter 1). The current density increase with salt concentration for $Ca(BH_4)_2$ in THF plating and stripping (Figure 4.2 middle) is likely due in part to the increase in conductivity with concentration which reduces the Ohmic voltage drop. It is noted that, following convention,[121] the Ohmic drop is not corrected for in the Figure 4.2. The

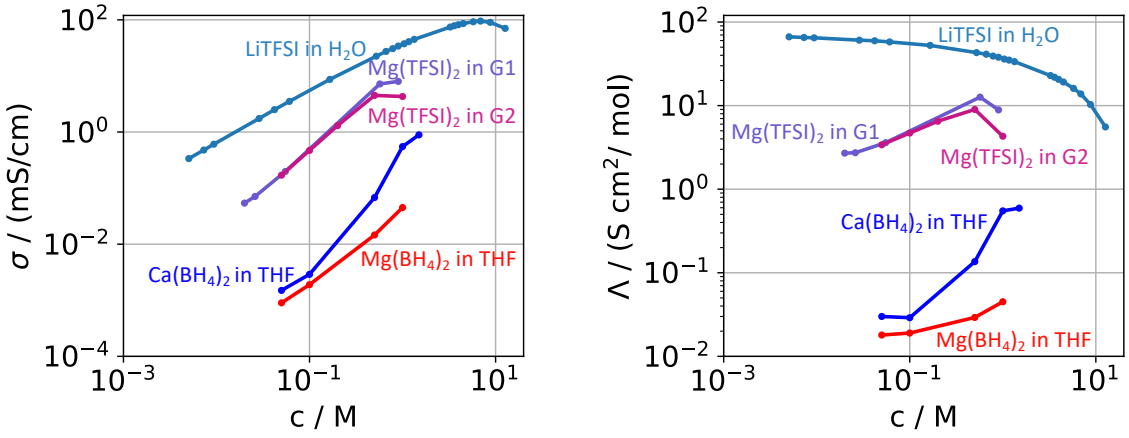

Figure 4.3: Conductivity (left) and molar conductivity (right) of various Ca and Mg electrolytes. Data taken from literature.[20, 74, 130]

rest of this chapter will focus on probing the nanoscale structure of this calcium electrolyte ($Ca(BH_4)_2$ in THF) for three reasons. First, understanding the solvation structure and its link(s) to transport will aid in the future design of liquid electrolytes with adequate transport properties. Second, the solvation structures and environment of the electroactive specices may be vital in understanding the electrode-film forming processes, which are considered one of the main impediments to calcium eletrochemistry. Third, $Ca(BH_4)_2$ in THF provides a valuable case study given its high Coulombic efficiency and interest transport properties.

The remainder of this chapter is reproduced in large part from a manuscript authored by Nathan T. Hahn, Julian Self, Kee Sung Han, Vijayakumar Murugesan, Karl T. Mueller, Kristin A. Persson and Kevin R. Zavadil, with permission from the Journal of Physical Chemistry B, Copyright 2021, American Chemical Society.[131] The content, as well as most of the wording, is a collaborative effort between all the authors listed in the above cited publication.

4.3 Quantifying Species Populations in Multivalent Borohydride Electrolytes

Multivalent batteries represent an important beyond Li-ion energy storage concept. The prospect of calcium batteries in particular has emerged recently due to novel electrolyte demonstrations, especially that of a ground-breaking combination of the borohydride salt $Ca(BH_4)_2$ dissolved in tetrahydrofuran. Recent analysis of magnesium and calcium versions

of this electrolyte led to the identification of divergent speciation pathways for Mg^{2+} and Ca^{2+} despite identical anions and solvents, owing to differences in cation size and attendant flexibility of coordination. To test these proposed speciation equilibria and develop a more quantitative understanding thereof, we have applied pulsed-field-gradient nuclear magnetic resonance and dielectric relaxation spectroscopy to the study of these electrolytes. Concentration-dependent variation in anion diffusivities and solution dipole relaxations, interpreted with the aid of molecular dynamics simulations, confirm these divergent Mg^{2+} and Ca^{2+} speciation pathways. These results provide a more quantitative description of the electroactive species populations. We find that these species are present in relatively small quantities, even in the highly active $Ca(BH_4)_2$/tetrahydrofuran electrolyte. This finding helps interpret previous characterizations of metal deposition efficiency and morphology control and thus provides important fundamental insight into the dynamic properties of multivalent electrolytes for next generation batteries.

Introduction

As discussed in Chapter 1, Li-ion batteries have come to dominate the global portable electronics and electrified vehicle markets, but further advances in batteries are required to meet anticipated energy storage needs for a diversity of applications.[132] Among the proposed avenues toward this goal, multivalent batteries, including Ca, Mg, Zn, and Al, are intriguing options due to the high energy densities and generally lower reactivities of their metallic anodes compared to Li.[133] The alkaline earth chemistries of Mg and Ca have received growing interest recently due to their significantly negative redox potentials, yielding the prospect of high cell voltage.[122, 133, 134] These high voltages, however, come at the cost of electrolyte stability, which must be managed to maintain high efficiencies and rates for the corresponding metal plating and stripping reactions. Because of this requirement, early stage electrolyte demonstrations have largely originated from exotic formulations containing reducing salts including organometallics facilitated by chloride dissolved in ethereal solvents such as tetrahydrofuran (THF).[135, 136] One of the first non-halide magnesium salts demonstrated to reversibly deposit Mg was $Mg(BH_4)_2$,[137, 138] and the first such calcium salt to function in this manner at room temperature was $Ca(BH_4)_2$.[129] The ground-breaking nature of these electrolytes highlights the importance of the borohydride class as a system of fundamental study, despite its obvious drawbacks from the standpoint of oxidative reactivity. Moreover, understanding the links between borohydride solvation environments and properties has high potential impact for both solid-state electrolytes and reversible hydrogen storage, areas in which borohydrides are under active investigation.[139–142]

While several investigations into the liquid solvation environment of $Mg(BH_4)_2$ electrolytes have been conducted,[137, 138, 143–146] understanding of $Ca(BH_4)_2$ electrolyte solvation is relatively nascent.[130, 147] Our recent findings underscored the importance of BH_4^- coordination in determining speciation and delivery of the metal cation to the interface.[130] The most probable ionic species determined from density functional theory (DFT) calculations were found to be $CaBH_4^+$ and $Ca(BH_4)_3^-$, indicating that the electroactive

species is the cationic cluster $CaBH_4^+$. Difficulty in forming the active species, whether in $Ca(BH_4)_2$/THF at low concentrations ($\leq$ 0.5 M) or in $Mg(BH_4)_2$/THF across all salt concentrations, reduces the measured metal deposition current density and Coulombic efficiency.[130]. These findings also implicated the role of multimer formation in facilitating the creation of these important ionic species based on X-ray absorption spectroscopy; a key feature differentiating the behavior of the Mg and Ca electrolytes based on their configurational flexibility differences. The term "configurational flexibility" reflects the fact that Ca^{2+} can adopt a wider range of bonding configurations due to its greater size and polarizability than Mg^{2+}.[148, 149] To validate these proposed speciation details from a more quantitative perspective, we report complimentary investigation into $Mg(BH_4)_2$ and $Ca(BH_4)_2$ solutions in THF via pulsed-field-gradient nuclear magnetic resonance (PFG-NMR) and dielectric relaxation spectroscopy (DRS). The results of this investigation confirm a significantly greater population of electroactive ionic species in the Ca system, which is particularly enhanced at high salt concentrations. By using molecular dynamics (MD) simulations to interpret the DRS data we are able to provide a quantitative estimation of the primary species in solution. We demonstrate the dominance of neutral monomers in $Mg(BH_4)_2$/THF across the full concentration range and the enhancement of neutral dimers and ionic species in $Ca(BH_4)_2$/THF at high salt concentrations. Despite the enhancement of electroactive $CaBH_4^+$ at high concentrations in the Ca case, the relative population of this species is still only a small fraction of the total Ca^{2+} inventory. This fact has important ramifications for sustaining high rate and energy efficient calcium plating from this electrolyte.

Methods

Electrolyte preparation: electrolyte synthesis was performed inside a catalyst-purified, argon filled glove box (MBraun) with typical water and oxygen levels below 1 ppm and 0.1 ppm, respectively. THF was purchased from Sigma-Aldrich, distilled over sodium, and stored over activated alumina and 3A molecular sieves prior to use, yielding measured water levels below 10 ppm. $Ca(BH_4)_2{\cdot}2THF$, $Mg(BH_4)_2$ (95%), and $LiBH_4$ (95%) salts were purchased from Sigma-Aldrich and used as received. Ionic conductivities were measured using electrochemical impedance spectroscopy in a custom cell consisting of parallel Pt electrodes, the cell constant of which was determined using aqueous KCl solutions. PFG-NMR: D_{anion} and D_{solvent} were determined simultaneously by ^{1}H PFG-NMR using a bipolar gradient PFG sequence at 25^{o}C on a 600 MHz NMR spectrometer (Agilent, USA) equipped with a 5 mm z-gradient probe (Doty Scientific, USA). The PFG-echo profiles were obtained as a function of gradient strength (g) with a gradient length (δ) and a diffusion delay fixed at 2 and 30 ms, respectively. The gradient strength was gradually increased in 16 equal steps to the maximum applied gradient strength to observe the full decay in the echo profiles. The recorded echo profiles, $S(g)$ were fitted with the Stejskal-Tanner equation,

$$S(g) = S(0)\exp[-D(\gamma g\delta)^2(\Delta - \delta/3)] \tag{4.1}$$

where $S(0)$ is the echo intensity at gradient strength of zero. D, γ, δ, and Δ are the diffusion coefficient, the gyromagnetic ratio ($\gamma(^1\mathrm{H}) = 2\pi \cdot 42.577$ rad $\cdot$ MHz $\cdot$ T^{-1}), the gradient length, and the time interval between the two bipolar gradient pairs, respectively. ^{43}Ca and ^{25}Mg PFG-NMR were not successful for the determination of D_{cation} for Ca^{2+} and Mg^{2+} in these solutions due to the fast nuclear relaxation rates for ^{43}Ca and ^{25}Mg in these samples. Dielectric Relaxation Spectroscopy: DRS was performed on electrolytes in glass vials using a dielectric probe kit (Keysight N1501A) and vector network analyzer (Keysight 9375A) over a frequency range of 0.5 to 26.5 GHz. Each set of measurements were performed with three-point calibration using air, a shorting block, and THF. Duplicate measurements were performed after recalibration to ensure consistency. Simultaneous fitting of the real (ε') and imaginary (ε") components of the complex, frequency-dependent relative permittivity (equation 4.2) was performed numerically by deconvolution of the individual dipole relaxation processes (equation 4.3).[47]

$$\varepsilon(\nu) = \varepsilon'(\nu) - i\varepsilon''(\nu) \tag{4.2}$$

$$\varepsilon(\nu) = \varepsilon_\infty + \Sigma_{j=1}^{n} \varepsilon_j [1 - (i2\pi\nu\tau_j)^{1-\alpha_j}]^{-1} \tag{4.3}$$

In equation 4.3, ε_∞ accounts for the total intramolecular polarizability of the solution while the n solution dipole re-orientation contributions are included in the summation term based on each dipole's permittivity amplitude (ε), relaxation time (τ), and broadening or Cole-Cole parameter (α). For Debye relaxations $\alpha = 0$. Ionic conductivities (used to extract ε'' from the permittivity data) measured by impedance spectroscopy were treated as fixed parameters during the fitting process. It was determined that spectra obtained from the $Mg(BH_4)_2$/THF solutions were best fit by one Debye relaxation for the solvent and one Cole-Cole relaxation for the salt while spectra from $Ca(BH_4)_2$/THF solutions were best fit by two to three Debye relaxations. Summation of these relaxation amplitudes yields the total dielectric constant, ε_r, of the solution (denoted as ε in the previous chapters. See Appendix for fitting parameters, Table A.4 and A.5). The 1.0 M $Mg(BH_4)_2$ solution was observed to react at the probe tip, nucleating small bubbles which impacted the measured parameters. The data reported for this system were thus averaged over completely independent electrolyte makeups and calibrations (see Appendix, Table A.5). The conclusions are not impacted by the uncertainty in this datapoint. Aside from the 1.0 M $Mg(BH_4)_2$ solution, the samples showed consistent dielectric constants in repeated measurements (typically better than $\pm$ 0.05). Species populations were determined by combining the measured dielectric constant changes with calculated dielectric increments ($\Delta\varepsilon$) and $\Lambda/\Lambda_{\mathrm{NMR,eff}}$ measurements, as described in the Appendix.

Regarding computational simulations, dielectric increment calculations were done with classical molecular dynamics simulations, as discussed in Chapter 2 and previous publications.[20, 57] Single salt species (such as CIPs, etc.) were placed in a box with 112 THF solvent molecules (approx. 0.10-0.11 M) using PACKMOL. With the GROMACS MD software, these electrolytes were equilibrated first using a Berendsen barostat (NPT), followed

by heating and cooling steps. Afterwards, production runs in the NVT ensemble using the velocity rescaling thermostat were undertaken. In these regimes, salt species were associated for the duration of the simulation (each at least 10 ns) and from their dipole moment, in addition to the dipole moment of the solvent species, the dielectric constant of the entire electrolyte solution was found. The dielectric constant of the neat THF solution was subtracted from this value, which was then subsequently divided by the concentration (e.g. 0.11 M) to obtain the dielectric increment per salt species, as appearing in the Appendix (Table A.6, Table A.7, and Figure A.8). For associated salt species with an overall charge, the overall charge was subtracted from the dipole moment as discussed in a previous publication.[20] The forcefield parameter files for BH_4^- were the same as those from Rajput et al.,[130, 150], the THF force field files from Caleman et al. and the Ca and Mg forcefield files from the standard OPLS forcefield.[53, 68] Error estimates appearing in Table A.6 and A.7 were calculated from duplicate simulations and analyses.

Results and Discussion

An increase in relative electroactive ionic species populations with overall salt concentration is demonstrated in that the ionic conductivities of both $Mg(BH_4)_2$/THF and $Ca(BH_4)_2$/THF solutions increase with concentration despite a drop in average BH_4^- diffusivity. Although the conductivity increase is much more dramatic for $Ca(BH_4)_2$ than for $Mg(BH_4)_2$, both increase significantly on a relative basis (Figure 4.4 a). When the conductivity values are normalized by concentration yielding molar conductivities, Λ, the positive trends persist up to 1 M (Figure 4.3). An increase in Λ should represent an increase either in the ionicity (relative formation of ionic species) of the electrolyte or in the diffusivities of the ionic species. Since the PFG-NMR measured diffusivity of BH_4^- (D_{anion}) decreases by nearly a factor of two in both solutions as concentration increases from 0.1 to 1.0 M (Figure 4.4 b), the dominant factor must be an ionicity increase. This increase is clearly enhanced in the Ca system.

The significant ionicity increase in these solutions occurs despite their strong ion pairing tendencies. The presence of extensive ion pairing is demonstrated by the relative anion and solvent diffusivities as measured by PFG-NMR. As shown in Figure 4.4 b), the decrease in D_{anion} is accompanied by a decrease in THF diffusivity (D_{solvent}) with increasing concentration. This can be attributed to both an increase in solution viscosity (η) and an increased fraction of THF bound to the metal cations. To account for the solution viscosity changes, the ratio of $D_{\text{anion}}/D_{\text{solvent}}$ was calculated in each case (Figure 4.4 c). Viscosity should affect both anion and solvent diffusivities in a similar manner based on the Stokes-Einstein relation $D \sim (\eta R)^{-1}$, where R is the effective radius of the solution species. In all solutions D_{anion} is less than half of D_{solvent}, despite that fact that the calculated radius of gyration (R_g) of BH_4^- from MD simulations ($R_g = 0.6$ Å) is smaller than that of THF ($R_g = 1.4$ A). This difference in R_g means that a "free" BH_4^- anion should diffuse much faster than a free THF molecule. The fact that $D_{\text{anion}} < D_{\text{solvent}}$ indicates that most, if not all, of the BH_4^- anions are coordinated to metal cations, forming clusters with significantly larger effective

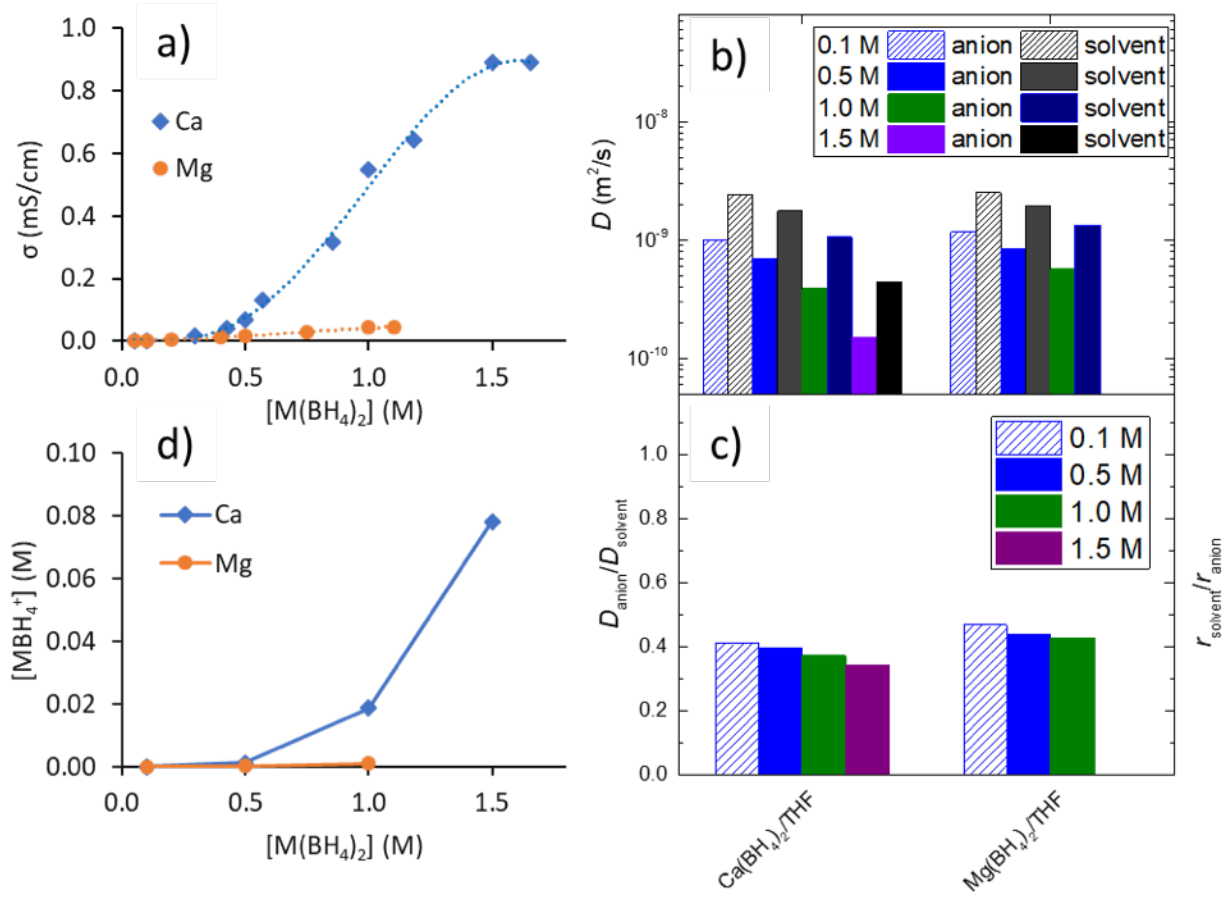

Figure 4.4: a) Ionic conductivity values measured for $Mg(BH_4)_2$ and $Ca(BH_4)_2$ in THF as a function of concentration (adapted in part from Hahn et al.[130] with permission from the Royal Society of Chemistry). Dotted lines represent polynomial fits serving as guides to the eye. b) Diffusivity values of BH_4^- and THF measured by PFG-NMR as a function of borohydride salt concentration. c) The relative diffusivities of anion:solvent calculated from the PFG-NMR data. d) Calculated concentrations of $CaBH_4^+$ and $MgBH_4^+$ in solution as a function of overall salt concentration based on an effective ionicity ratio analysis, assuming ionic species of MBH_4^+ and $M(BH_4)_3^-$.

radii than free BH_4^- and yielding a lower average D_{anion} value. Indeed, the calculated R_g values for associated clusters from MD simulations are between 2.5 and 4.5 A, i.e. approximately twice as large as the R_g of THF. This size difference is consistent with the measured $D_{\text{anion}}/D_{\text{solvent}}$ values (Appendix, Tables A.6 and A.7).

The absence of free BH_4^- is consistent with previously reported Raman measurements that were unable to detect free BH_4^- in these electrolytes and with DFT calculations showing that dissociation of BH_4^- from Ca^{2+} or Mg^{2+} is unfavorable.[130, 144] Indeed, even the dissociation of BH_4^- from Li^+ is highly unfavorable in THF.[151] Furthermore, DFT calculations indicated that the primary ionic species in $Ca(BH_4)_2$/THF are most likely the associated clusters $CaBH_4^+$ and $Ca(BH_4)_3^-$, in which case the overall equilibrium could be considered as $2Ca(BH_4)_2 \leftrightarrow CaBH_4^+ + Ca(BH_4)_3^-$. The differences in measured Λ between the Ca^{2+} and Mg^{2+} electrolytes imply that these clusters form much more readily from $Ca(BH_4)_2$ than from $Mg(BH_4)_2$ in THF. The fact that $D_{\text{anion}}/D_{\text{solvent}}$ decreases with increasing concentration in both $Ca(BH_4)_2$ and $Mg(BH_4)_2$ solutions confirms that enhanced populations of free BH_4^- (which would increase $D_{\text{anion}}/D_{\text{solvent}}$) are not the origin of the ionicity increases. If anything, this trend implies that some degree of salt aggregation is favored at high concentrations in both solutions, although previous work indicated that $Ca(BH_4)_2$ more readily forms multimeric species than $Mg(BH_4)_2$ in THF.[130, 152–154] These results validate our hypothesis that the primary origin of the increasing Λ vs. concentration trend in alkaline earth borohydride solutions is the enhanced formation of associated ionic clusters such as MBH_4^+ rather than liberation of free BH_4^- or a possible increase in ion diffusivity.[155]

Considering these results in light of the proposed ionic species (MBH_4^+ and $M(BH_4)_3^-$),[130] we estimate their concentrations from the measured Λ and D_{anion} values based on an effective ionicity ratio $\Lambda/\Lambda_{\text{NMR,eff}}$ (i.e. effective Haven ratio), where $\Lambda_{\text{NMR,eff}}$ is the molar conductivity expected if all the dissolved salt is converted into the proposed ionic species. This value is given by equation 4.4:[156, 157]

$$\Lambda_{\text{NMR,eff}} = \frac{eF}{k_B T}\left(\frac{D_i z_i^2 c_i}{c_{\text{salt}}} + \frac{D_j z_j^2 c_j}{c_{\text{salt}}}\right) \tag{4.4}$$

In equation 4.4, species i and j refer to MBH_4^+ and $M(BH_4)_3^-$, respectively, D is the species self-diffusion coefficient, z is the species charge, c is the species concentration, and c_{salt} is the overall salt concentration. Therefore, $z_i = z_j = 1$, and $c_i/c_{\text{salt}} = c_j/c_{\text{salt}} = 0.5$ based on stoichiometry. To a first approximation it is assumed that $D_i = D_j$, i.e. $D(MBH_4^+) = D(M(BH_4)_3^-)$, and that these diffusivities are approximately equal to the ensemble measured anion (BH_4^-) diffusivity. These assumptions are based on the lack of free BH_4^- and on the similarity of the calculated R_g values for the resulting metal-borohydride clusters in MD simulations (Appendix, Tables A.6 and A.7). Furthermore, the charged cluster diffusivities are not expected to differ much from those of the neutral clusters.[158, 159] The contributions of the charged clusters to $\Lambda_{\text{NMR,eff}}$ are approximated as ideal, i.e. long-range interionic interactions are neglected. Thus, ionic populations estimated from the effective ionicity may be somewhat underestimated. The MBH_4^+ concentrations resulting from this

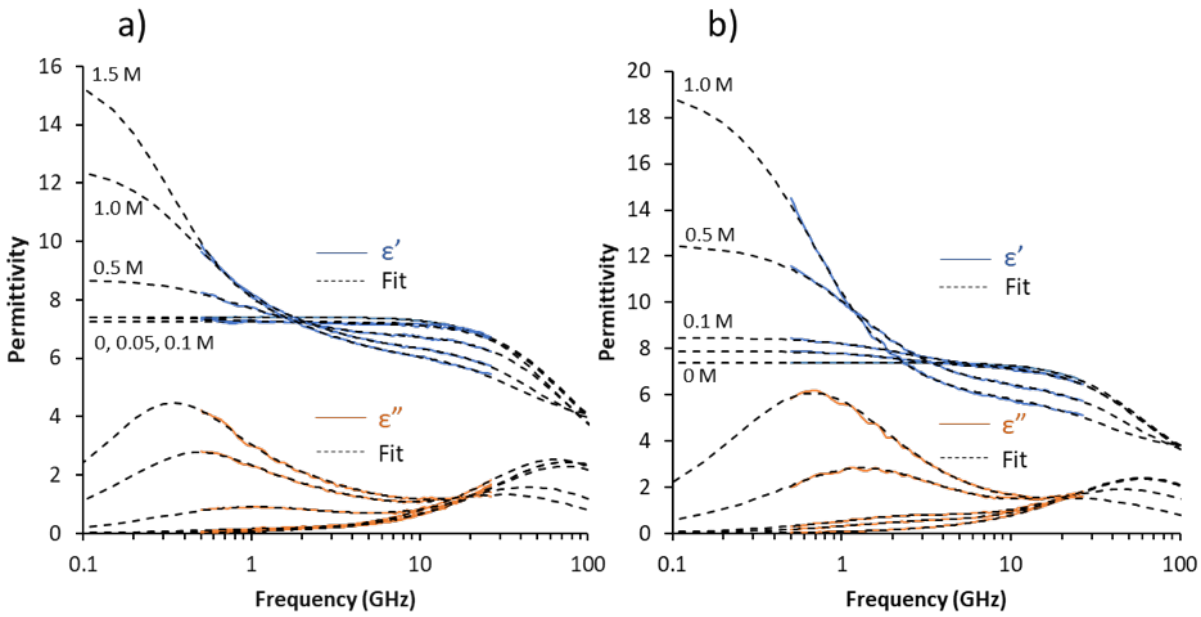

Figure 4.5: Real (ε', top) and imaginary (ε'', bottom) components of the complex permittivity measured as a function of frequency in a) $Ca(BH_4)_2$/THF and b) $Mg(BH_4)$/THF. Solid lines represent the measured data while dashed lines represent fits of the data based on a summation of Debye and/or Cole-Cole relaxations. Deconvolutions of these relaxations are shown in the Appendix, Figure A.6.

analysis are shown in Figure 4.4 d). These calculations highlight the remarkable increase in concentration of these electroactive species as a function of overall salt concentration in the Ca system. These species are almost non-existent at salt concentrations less than 0.5 M, which readily explains the severely inhibited calcium electrodeposition response reported at such concentrations.[130] Since the Mg system possesses very low concentrations of $MgBH_4^+$ at all salt concentrations, its metal deposition response is inhibited even at high salt concentrations. This is consistent with previous reports demonstrating that alkali-salt additives ($LiBH_4$ or $NaBH_4$) are required to achieve adequate magnesium electrodeposition rate and reversibility.[137, 144, 145, 160]

Significant differences in the concentration-dependent speciation pathways of the Mg and Ca electrolytes are manifested in the complex permittivity responses of the solvated species. DRS spectra measured across a range of salt concentrations in these two systems reveal their characteristic frequency-dependent permittivity (Figure 4.5). In both systems two primary relaxations are observed: a high frequency solvent relaxation (f $\sim$ 30 to 70 GHz), and a low frequency relaxation corresponding to dipolar salt clusters (f $\sim$ 0.3 to 3 GHz). The $Ca(BH_4)_2$ clusters exhibit slower relaxations due to the larger size of Ca^{2+} and its related complexes.

In $Ca(BH_4)_2$/THF the impact of dipolar salt clusters on the solution permittivity is not significant until salt concentration exceeds 0.1 M while in $Mg(BH_4)_2$/THF these clusters are significant even at 0.05 M. Due to the presence of these clusters, the dielectric constants (ε_r) of the concentrated solutions are far greater that of the neat THF solvent ($\varepsilon_r = 7.4$), reaching values as high as 18.2 for $Mg(BH_4)_2$ and 16.0 for $Ca(BH_4)_2$ (Figure 4.6 a). Our observation of a net increase in ε_r is consistent with previous investigations of strongly associating alkali salts in low permittivity solvents.[19, 48, 130, 161] Recently we speculated that ε_r could increase to a value as high as 10 in $Ca(BH_4)_2$/THF due to such effects,[130] but this value turns out to have been a significant underestimation. The most important difference in the permittivity behavior of the Mg and Ca systems lies in the functional forms of the ε_r vs. concentration dependence (Figure 4.6). In $Mg(BH_4)_2$/THF, ε_r increases linearly across the entire concentration range while in $Ca(BH_4)_2$/THF the ε_r change is non-linear and even non-monotonic. The linear $Mg(BH_4)_2$ behavior implies an essentially static speciation profile in which one or more dipolar clusters are present at a constant relative population regardless of salt concentration. In contrast, the $Ca(BH_4)_2$ behavior implies on evolving speciation profile where the relative dipolar cluster populations vary significantly with salt concentration. This result speaks to the configurational flexibility differences of Ca^{2+} and Mg^{2+}.

Our previous investigations led us to conclude that the primary solvated species in $Mg(BH_4)_2$/THF is the neutral, monomeric form of the dissolved salt across all concentrations, based on the low measured conductivities and the reported tendency of $Mg(BH_4)_2$ toward forming monomeric solvates.[130, 152, 154] To test whether such species could explain the linear and steeply sloped ε_r vs. concentration trend, the dielectric increments ($\Delta\varepsilon$) of several clusters were simulated by MD; the parameter $\Delta\varepsilon$ represents the net change in ε_r that a given cluster would induce when formed in a THF medium at a concentration of 1 M. The neutral monomer, $Mg(BH_4)_2$, possesses a highly asymmetric structure and a large dipole moment leading to a large computed net $\Delta\varepsilon$ of 8.9 M^{-1}. This value agrees well with the net $\Delta\varepsilon$ of 9.4 $^{-1}$ measured for this electrolyte across the entire concentration range (Appendix, Figure A.7). This agreement suggests that these neutral monomers are the majority solvated species across this concentration range. We note that the small populations of $MgBH_4^+$ species predicted from conductivity and diffusivity analyses are unlikely to be observed by DRS due to their low concentration. For comparison, measurements of $LiBH_4$/THF as a simpler 1:1 salt system ostensibly dominated by neutral contact ion pairs (CIPs) in THF ($K_A \sim 10^9$)[151] also yielded a linear ε_r vs. concentration trend (Appendix, Figure A.8). As in the Mg case, the $\Delta\varepsilon$ derived from the $LiBH_4$ measurements agrees with the calculated $\Delta\varepsilon$ value (9.2 vs. 9.7). This agreement between measured overall $\Delta\varepsilon$ and calculated neutral monomer $\Delta\varepsilon$ in both systems provides strong evidence that both systems are dominated by these species at the concentrations investigated. In previous studies, salt clusters composed of a single cation and two anions ("triple ions") were sometimes presumed as linear and thus not detectable as dipolar species by DRS.[48, 49] However, a more rigorous evaluation of cluster dielectric increments by MD simulations clearly shows that such structural assumptions can be misleading, as exemplified by the case of $Mg(BH_4)_2$/THF.

In $Ca(BH_4)_2$/THF we recently proposed that neutral monomers ($Ca(BH_4)_2$) are prevalent

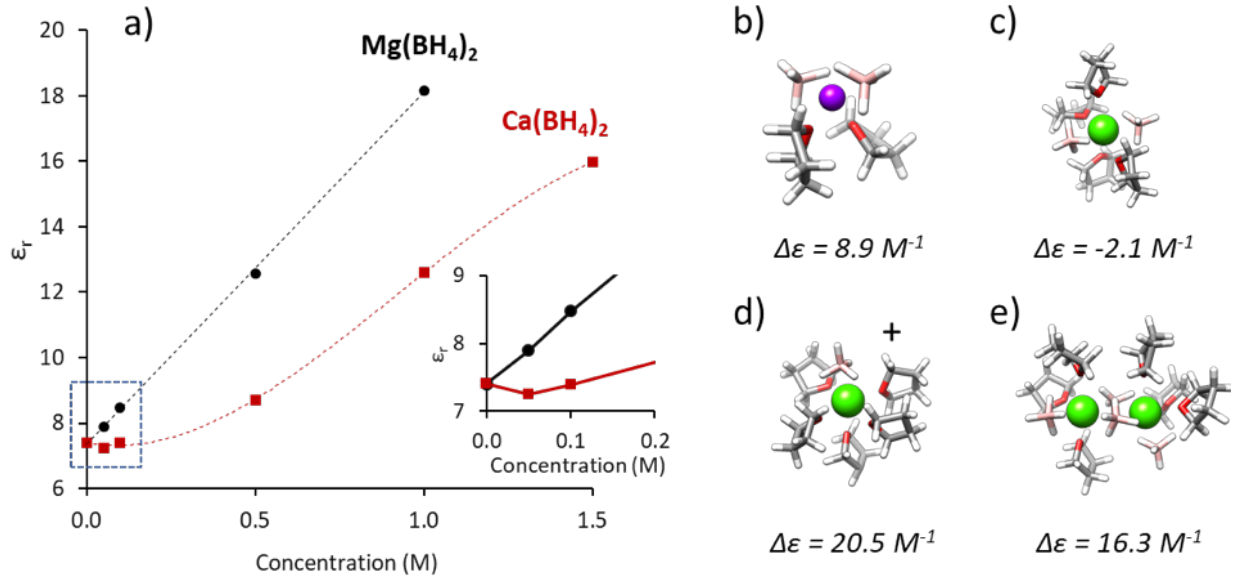

Figure 4.6: a) Solution dielectric constants (ε_r) determined from fits of the complex permittivity data as a function of concentration. Dotted lines represent trend lines for the ε_r vs. concentration data (linear in the case of Mg^{2+} and polynomial in the case of Ca^{2+}). Inset: magnification of the plots at low concentrations. b-e) Representative cluster structures to which the ε_r changes are attributed. The calculated net dielectric increment ($\Delta\varepsilon$) of each cluster is indicated. These species are referred to as: b) Mg neutral monomer, c) Ca neutral monomer, d) Ca CIP (contact ion pair) cation, e) Ca neutral dimer (bent configuration). Mg, Ca, B, C, H and O atoms are shown in purple, green, pink, grey, white and red respectively. The calculated parameters and uncertainties of all species investigated are shown in Tables A.4 and A.5 in the Appendix.

at low salt concentrations and that these are progressively converted to multimeric and ionic species such as $Ca_2(BH_4)_4$, $CaBH_4^+$, and $Ca(BH_4)_3^-$ as salt concentration is increased.[130] Calculations of these species' $\Delta\varepsilon$ values indicates that our hypothesized trajectory of species evolution can explain the unique ε_r vs. concentration trend measured in this system (Figure 4.6). MD simulations reveal that the neutral calcium monomer is much more symmetric than the magnesium analog and has almost no dipole moment (Figure 4.6 c), resulting in a $\Delta\varepsilon$ of -2.1 M^{-1}. The negative $\Delta\varepsilon$ arises from the fact that several THF molecules are bound to this solvated cluster and can no longer contribute to the background dielectric constant. Therefore, a population of solvated neutral monomers can readily explain the small initial decrease in measured dielectric constant of $\sim$ 0.1 units at 0.05 M (Figure 4.6a, inset). At concentrations above 0.1 M the measured dielectric constant increases significantly above that of neat THF, signaling a shift in the solution equilibria toward more polar clusters.

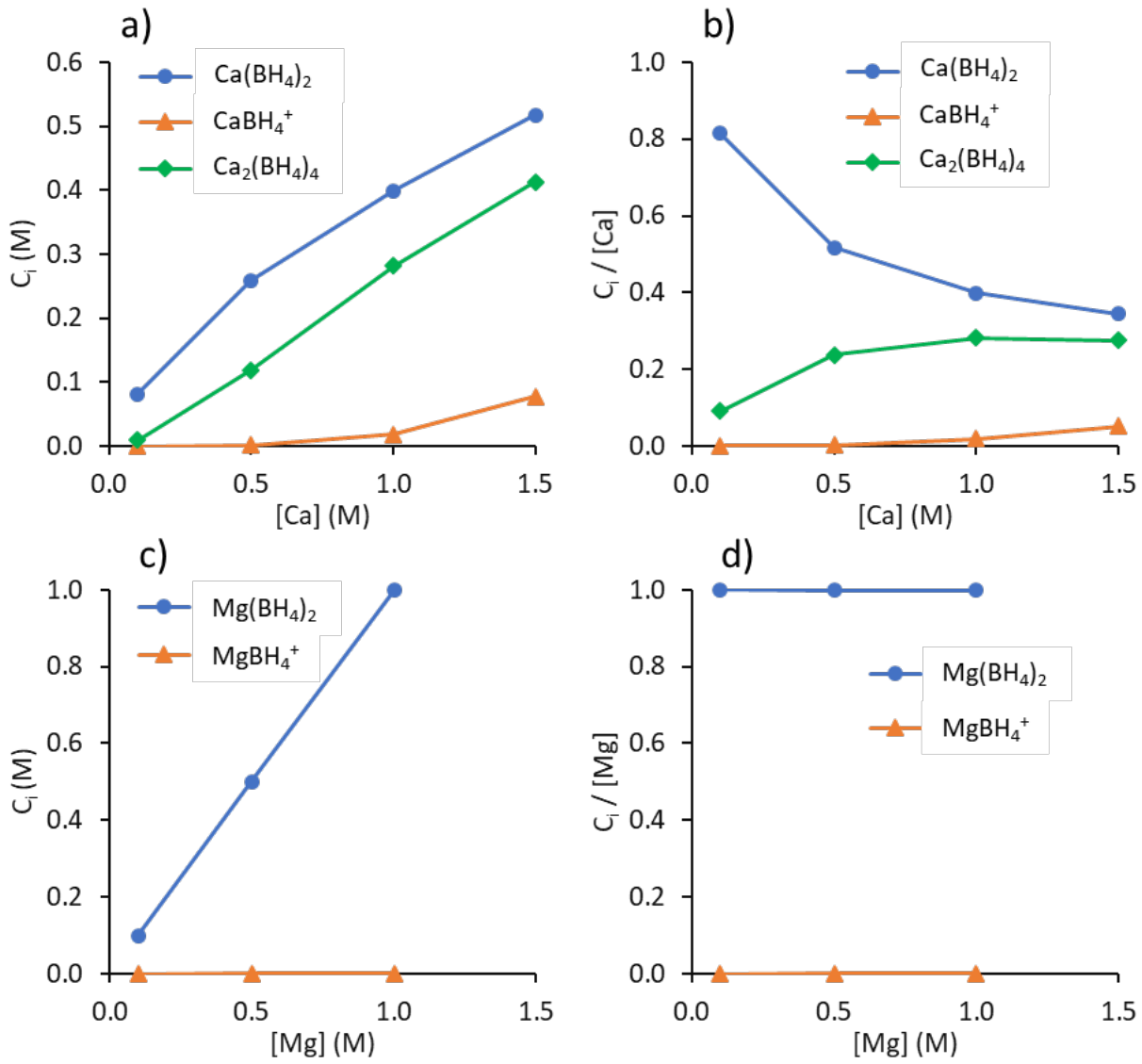

Figure 4.7: Concentrations of the major solvated species calculated from the effective ionicity analysis combined with DRS measurements and modeling as a function of overall salt concentration for (a,b) $Ca(BH_4)_2$/THF and (c,d) $Mg(BH_4)_2$/THF. The data are plotted either (a,c) as species concentrations or (b,d) as relative populations. It is assumed that $[MBH_4^+] = [M(BH_4)_3^-]$.

Analysis of the hypothesized clusters reveals that both $CaBH_4^+$ ($\Delta\varepsilon$ = 20.5 M^{-1}) and $Ca_2(BH_4)_4$ ($\Delta\varepsilon$ = 16.3 M^{-1}) could contribute significantly to the permittivity increase measured in $Ca(BH_4)_2$/THF. The large dielectric increment of the dimer species is surprising given that neutral dimers are often assumed to have negligible dipole moments due to their approximately symmetric structure.[48, 97] However, over our simulated MD trajectory we find that this $Ca_2(BH_4)_4$ cluster frequently rearranges into bent or pyramidal configurations, leading to a significant time-averaged dipole moment magnitude and a resulting dielectric increment of 16.3 M^{-1} (Appendix Figure A.9). This again highlights the importance of MD simulations in accurately accounting for the range of conformations that a given cluster may adopt. The calculated $\Delta\varepsilon$ values allow for estimation of various species populations contributing to the overall measured $\Delta\varepsilon$ assuming an equilibrium distribution among the four proposed major species: $2\,Ca(BH_4)_2 \leftrightarrow Ca_2(BH_4)_4 \leftrightarrow CaBH_4^+ + Ca(BH_4)_3^-$. The MD-simulated $\Delta\varepsilon$ values of these species were used to calculate the self-consistent populations that could account for the measured overall $\Delta\varepsilon$ at each salt concentration. To bolster this approach, the calculations were refined by incorporating the $CaBH_4^+$ and $Ca(BH_4)_3^-$ concentrations predicted from the aforementioned effective ionicity analysis (as shown in Figure 4.4 d). Without this input, the species populations cannot be inferred precisely due to difficulties in differentiating the contributions of $CaBH_4^+$ and $Ca_2(BH_4)_4$ to ε_r (Appendix, Figure A.10). The calculated speciation diagrams, as shown in Figure 4.7 a) and Figure 4.7 b), reveal that the neutral monomer is the dominant species at low salt concentrations of 0.1 M and below, that these species are partially converted to dimers at moderate to high salt concentrations, and that small populations of the ionic species become stabilized at high salt concentrations. In $Mg(BH_4)_2$/THF, however, the neutral monomers are more strongly favored and almost no change in speciation is observed (Figure 4.7 c-d).

The fact that dimers account for at least half of the total calcium inventory in solution at high salt concentrations ensures their detection via X-ray absorption spectroscopy,[130] lending credence to these calculations. The high concentration of polar dimers and the resulting solution permittivity increase likely helps stabilize the ionic species. This phenomenon is termed "redissociation".[20, 48, 99] However, we note that such a mechanism apparently does not operate nearly as effectively in $Mg(BH_4)_2$/THF despite its high concentration of polar monomers. We speculate that this is due to a smaller thermodynamic equilibrium constant for forming the proposed ionic species (MBH_4^+ and $M(BH_4)_3^-$), due to the greater charge density and lesser polarizability of Mg^{2+}. Therefore, the configurational flexibility of Ca^{2+} remains an important criterion for effective ionic cluster formation in these strongly ion-associating solutions. We further note that "redissociation" has generally previously referred to the stabilization of free ions at higher concentration, while here the ionic species are ion-pairs or ion clusters. Thus, a perhaps better term would here be "reioniziation".

Although the proposed electroactive species $CaBH_4^+$ constitutes only a minority population in $Ca(BH_4)_2$/THF, the kinetics of species interconversion likely prevent $CaBH_4^+$ from becoming selectively depleted at the anode surface during calcium plating (i.e. cell charging). The kinetics of ion pairing and dissociation are generally fast enough, by many orders of magnitude,[162] to prevent species-specific depletion due to electrochemical con-

sumption at an electrode, provided the overall concentration of salt is maintained. However, the concentration-dependent thermodynamics of speciation, as demonstrated in Figure 4.7, predict a strong suppression of [$CaBH_4^+$] near the surface and in the diffusion layer if large salt concentration gradients are formed during high rate and/or high capacity calcium plating. This suppression of ionic species may lead to a significant Ohmic potential drop despite high bulk salt concentrations. Moreover, low concentrations of electroactive $CaBH_4^+$ near the electrode may promote parasitic reactions and loss of calcium morphology control. Indeed, a recent study highlighted that such rate-dependent calcium plating problems are encountered in $Ca(BH_4)_2$/THF electrolytes.[163] Therefore, we propose the relatively small, concentration-dependent population of $CaBH_4^+$ as the underlying cause. Our findings thus inform both recent and ongoing efforts at studying interfacial phenomena in these unique electrolyte environments.

Conclusion

Complimentary analyses of ionic conductivity, anion diffusivity, and solution permittivity augment our quantitative understanding of solvation in an important class of alkaline earth metal borohydride electrolytes in THF. The primary findings of these analyses are: 1) both $Mg(BH_4)_2$ and $Ca(BH_4)_2$ electrolytes exhibit an increase in ionicity with concentration despite extensive ion pairing in both systems; 2) electroactive MBH_4^+ species populations are much more favored in the latter case, especially at high salt concentrations; 3) $Mg(BH_4)_2$/THF is dominated by neutral monomers across the full concentration range while $Ca(BH_4)_2$/THF speciation evolves from neutral monomers to multimers and ionic species; 4) the population of the electroactive $CaBH_4^+$ species in $Ca(BH_4)_2$/THF is less than 0.1 M, even in high salt concentration electrolytes (1 to 1.5 M) that support high Coulombic efficiency electrodeposition. The ability to quantify species populations in the $Ca(BH_4)_2$/THF electrolyte represents an important contribution to the understanding of these systems that directly links to recent demonstrations of surface and interfacial phenomena.

Chapter 5

Conclusion and Further Work

5.1 Further Work

This thesis encompasses case studies of Ca and Mg salts in ethereal electrolytes where the particular emphasis was put on discussing the various thermodynamics driving forces that dictate speciation. Moreover, methodology to interpret dielectric spectra via use of molecular dynamics simulations was established. Regarding the physical chemistry and electrochemistry of such electrolyte solutions, many questions are left unanswered and would benefit from further work.

For example, certain low permittivity electrolytes, notably $MgTFSI_2$ in G1, show a miscibility gap.[20, 93] Between concentrations of 0.05 M - 0.6 M (approximately), the $MgTFSI_2$ in G1 electrolyte spontaneously segregates into low and high density regions. Our work indicates that the low concentration (lower density phase) is of lower permittivity than the higher concentration phase (higher density). This suggests a parallel between the immiscibilty of oil in water, where solvents of significantly different polarity are immiscible. However, since $MgTFSI_2$ in G2 does not show a miscibility gap, this analogy is not sufficient to explain the phenomenon. Perhaps the specific short-range solvation of G1 or G2 (e.g. denticity, solvation number) contributes to the thermodynamic driving forces for immiscibility. In addition, the role of higher order aggregates (e.g. neutral triple species) may be a critical factor distinguishing the G1 electrolytes from G2 electrolytes and may explain immiscibility.

Furthermore, the question of higher order associated species beyond CIPs was raised in Chapters 3 and 4. One such species is the SSIP, which was taken as negligible in concentration in the systems studied in the present work. Nonetheless a more refined approach can relax this assumption. However, the thermodynamics of SSIPs and whether they are predictable from first principles is not well established. For example, Eberspacher et al. noticed that SSIPs quickly fall in fractional population for certain chlorate salts in acetonitrile while the CIP fraction increases.[50] Mass action would suggest that both CIPs and SSIPs should increase with increasing salt concentration - and further work should investigate why this rule does not generally apply for the SSIPs. It is possible that the entropic contribution to free

energy from capture or release of solvent molecules upon ion pairing and ion dissociation[35] plays a critical role.

While the work presented in this thesis focuses on bulk electrolyte speciation, it is possible to extend this understanding to modelling salt concentration profiles in the diffusion layer using relevant transport models. Such continuum modelling is established in the literature[164] and is often done with the use of software packages such as COMSOL,[165] or more recently, PYBAMM.[166] Such approaches can allow for calculations of the limiting current[167] and may also allow for proper accounting of the Ohmic drop and concentration overpotentials for electrochemical measurements, which is important but seldom reported by investigators of Mg and Ca electrochemistry. Knowledge of the concentration overpotentials and Ohmic drop in turn allow estimation of surface overpotentials in a cell and may yield further insight on desolvation[21] and charge transfer kinetics. In this regard, it is possible that the kinetics of ion pair formation[162] may be used as an equilibrium "probe" of the kinetics of solvation and desolvation, although such methods are not yet well established.

Beyond bulk and continuum modelling of the diffusion layer, there remains the question of the interface, interphases and electric double layer. Although there exist classical molecular dynamics simulation methods to model the electrolyte at the interface of the electrode,[168, 169] such methodology is highly dependent on the specifics of the interface chemistry and termination, which are in many cases not known and hence the results may not be relevant to real systems. Analytic methods and/or phenomenological expressions[170–172] may be a viable complement or alternative, provided they are developed in a way that allows for experimental validation — perhaps via prediction of a surface overpotential relating to the transfer of an electroactive cation through the modelled double layer and/or interface and interphases.

An avenue different than that of further characterization of binary electrolytes (single salt and single solvent) is the consideration of ternary systems, as in two solvents and a salt, or two salts and a solvent. The methodology used in Chapters 3 and 4 can be applied to systems with a supporting electrolyte. One interesting case study is that of the bi-salt system $Mg(BH_4)_2$ with supporting $LiBH_4$ in an ethereal solvent.[137, 145, 160, 173] Such investigations may pave the way for bi-salt designer electrolytes to enhance transport and charge transfer kinetics.

5.2 Conclusion

In this thesis, it was found that anomalous transport in Mg and Ca ethereal electrolytes is well explained via the speciation of the salt in solution. Specifically, redissociation, or reionization, of the ions in solution explains the increase in molar conductivity. Dielectric relaxation spectroscopy was used to investigate the speciation in the Mg and Ca ether-based case studies. Moreover, methodology to analyze dielectric spectra using molecular dynamics simulation was developed and used successfully. It was shown that the specific permittivity contributions from various ionic species can be computed. These species-specific contribu-

tions can allow calculation of the permittivity if speciation is computed, or alternatively, help infer speciation if the permittivity is measured.

In the case of $MgTFSI_2$ in G1 and $MgTFSI_2$ in G2, redissociation from charged contact ion pairs to free ions explains the increase in molar conductivity. Moreover, it was found that speciation diagrams can be constructed from first principles. Consideration of Debye-Huckel theory, Born solvation and ion pairing were necessary for a reasonable physical chemical picture of the ions in solution. The agreement between theory and DRS-derived speciation was further confirmed through independent Raman spectroscopy measurements. A clear picture was provided for the speciation of ions in the studied solutions — a topic that has been under considerable contention.

For $Ca(BH_4)_2$ and $Mg(BH_4)_2$ in THF, speciation from DRS measurements was inferred. Here, once again, redissociation, or reionization, as neutral species diminish in fraction to allow for a higher fraction of ionic (charged) species at higher salt concentrations, is consistent with the measured results. The dielectric constant of the electrolyte increases from the presence of neutral ionic cluster species, providing a thermodynamic driving force for a lager fraction of charged species as the salt concentration increases. It was found that for $Ca(BH_4)_2$ salt in THF, both neutral $Ca(BH_4)_2$ and $Ca_2(BH_4)_4$ species were present in significant quantities. The ionic cluster species of $Ca(BH_4)^+$ and $Ca(BH_4)_3^-$ were the main charge carriers, with free ion presence being negligible.

The findings presented in this thesis are relevant to fundamental physical chemistry and applied electrochemistry. In the latter case, redissociation and transport may be enhanced with designer electrolytes, via use of either dual solvent or dual salt electrolytes.

Bibliography

(1) Whittingham, M. S. *Chemical Reviews* **2014**, *114*, 11414–11443.

(2) Canepa, P.; Sai Gautam, G.; Hannah, D. C.; Malik, R.; Liu, M.; Gallagher, K. G.; Persson, K. A.; Ceder, G. *Chemical Reviews* **2017**, *117*, 4287–4341.

(3) Tran, T. T. The Use of Alloy Anodes and Conventional Electrolytes in Magnesium Batteries, Ph.D. Thesis, Dalhousie University, 2012.

(4) Nuss, P.; Eckelman, M. J. *PLoS ONE* **2014**, *9*, ed. by Janssen, P. J., e101298.

(5) Hebié, S.; Ngo, H. P. K.; Leprêtre, J.-C.; Iojoiu, C.; Cointeaux, L.; Berthelot, R.; Alloin, F. *ACS Applied Materials & Interfaces* **2017**, *9*, 28377–28385.

(6) Sa, N.; Pan, B.; Saha-Shah, A.; Hubaud, A. A.; Vaughey, J. T.; Baker, L. A.; Liao, C.; Burrell, A. K. *ACS Applied Materials & Interfaces* **2016**, *8*, 16002–16008.

(7) Van der Ven, A.; Deng, Z.; Banerjee, S.; Ong, S. P. *Chemical reviews* **2020**, *120*, 6977–7019.

(8) Attias, R.; Salama, M.; Hirsch, B.; Goffer, Y.; Aurbach, D. *Joule* **2019**, *3*, 27–52.

(9) Song, J.; Sahadeo, E.; Noked, M.; Lee, S. B. *J. Phys. Chem. Lett.* **2016**, 14.

(10) Richard Feynman; R. B. Leighton; M. Sands, *The Feynman Lectures on Physics*; Basic Books: 2011; Vol. 1.

(11) Makar, G.; Kruger, J. *International materials reviews* **1993**, *38*, Publisher: Taylor & Francis, 138–153.

(12) Lide, D. R., *CRC handbook of chemistry and physics*; CRC press: 2004; Vol. 85.

(13) Buchner, R.; Hefter, G. T.; May, P. M. *The Journal of Physical Chemistry A* **1999**, *103*, 1–9.

(14) Perron, G.; Brouillette, D.; Desnoyers, J. *Can. J. Chem.* **1997**, *75*, 1608–1614.

(15) Wright, M. R., *An Introduction to Aqueous Electrolyte Solutions*; Wiley: 2007.

(16) Brouillette, D.; Perron, G.; Desnoyers, J. E., 32.

(17) Onishi, S.; Farber, H.; Petrucci, S. *The Journal of Physical Chemistry* **1980**, *84*, 2922–2927.

(18) Nanbu, N.; Watanabe, S.; Takehara, M.; Ue, M.; Sasaki, Y. *Journal of Electroanalytical Chemistry* **2009**, *625*, 7–15.

(19) Delsignore, M.; Farber, H.; Petrucci, S. *The Journal of Physical Chemistry* **1985**, *89*, 4968–4973.

(20) Self, J.; Hahn, N. T.; Fong, K. D.; McClary, S. A.; Zavadil, K. R.; Persson, K. A. *The Journal of Physical Chemistry Letters* **2020**, *11*, 2046–2052.

(21) Xu, K.; von Cresce, A.; Lee, U. *Langmuir* **2010**, *26*, 11538–11543.

(22) Ma, L.; Schroeder, M. A.; Pollard, T. P.; Borodin, O.; Ding, M. S.; Sun, R.; Cao, L.; Ho, J.; Baker, D. R.; Wang, C.; Xu, K. *Energy & Environmental Materials* **2020**, eem2.12077.

(23) Jow, R.; Zhang, S. S.; Xu, K.; Allen, J. *ECS Transactions* **2007**, *3*, 51–58.

(24) Newman, J.; Thomas-Alyea, K. E., *Electrochemical Systems*; John Wiley & Sons: 2012.

(25) Ue, M. *Journal of the electrochemical society* **1994**, *141*, 3336–3342.

(26) Shilov, I. Y.; Lyashchenko, A. K. *The Journal of Physical Chemistry B* **2015**, *119*, 10087–10095.

(27) Schlumpberger, S.; Bazant, M. Z. *arXiv:1709.03106 [cond-mat, physics:physics]* **2017**, arXiv: 1709.03106.

(28) Israelachvili, J. N., *Intermolecular and surface forces*; Academic press: 2011.

(29) Barthel, J.; Neueder, R.; Poepke, H.; Wittmann, H. *Journal of solution chemistry* **1999**, *28*, Publisher: Springer, 489–503.

(30) Cachet, H.; Fekir, M.; Lestrade, J.-C. *Canadian Journal of Chemistry* **1981**, *59*, 1051–1060.

(31) *Electrolytes for Lithium and Lithium-Ion Batteries*; Jow, T. R., Xu, K., Borodin, O., Ue, M., Eds.; Modern Aspects of Electrochemistry, Vol. 58; Springer New York: New York, NY, 2014.

(32) Pitzer, K. S. *The Journal of Physical Chemistry* **1973**, *77*, Publisher: ACS Publications, 268–277.

(33) Pitzer, K. S.; Mayorga, G. *The Journal of Physical Chemistry* **1973**, *77*, Publisher: ACS Publications, 2300–2308.

(34) Barthel, J.; Neueder, R.; Poepke, H.; Wittmann, H. *Journal of solution chemistry* **1998**, *27*, Publisher: Springer, 1055–1066.

(35) Marcus, Y.; Hefter, G. *Chemical Reviews* **2006**, *106*, 4585–4621.

(36) Blum, L. *Molecular Physics* **1975**, *30*, Publisher: Taylor & Francis, 1529–1535.

(37) Maribo-Mogensen, B.; Kontogeorgis, G. M.; Thomsen, K. *Industrial & Engineering Chemistry Research* **2012**, *51*, 5353–5363.

(38) Crothers, A. R.; Radke, C. J.; Prausnitz, J. M. *Industrial & Engineering Chemistry Research* **2019**, *58*, 18367–18377.

(39) Simonin, J.-P.; Bernard, O.; Blum, L. *The Journal of Physical Chemistry B* **1998**, *102*, 4411–4417.

(40) Vincze, J.; Valiskó, M.; Boda, D. *The Journal of Chemical Physics* **2010**, *133*, 154507.

(41) Valiskó, M.; Boda, D. *The Journal of Physical Chemistry B* **2015**, *119*, 14332–14336.

(42) Borodin, O.; Self, J.; Persson, K. A.; Wang, C.; Xu, K. *Joule* **2020**, *4*, 69–100.

(43) Self, J.; Fong, K. D.; Persson, K. A. *ACS Energy Letters* **2019**, *4*, 2843–2849.

(44) Abbo, H. S.; Al-Najar, A. A. *Bull. Chem. Soc. Jpn.* **1990**, *2447*, 2447–2449.

(45) Kondo, K.; Sano, M.; Hiwara, A.; Omi, T.; Fujita, M.; Kuwae, A.; Iida, M.; Mogi, K.; Yokoyama, H. *The Journal of Physical Chemistry B* **2000**, *104*, 5040–5044.

(46) Lee, W. H.; Wheaton, R. J. *The Journal of Physical Chemistry* **1978**, *82*, 605–608.

(47) Buchner, R.; Hefter, G. *Physical Chemistry Chemical Physics* **2009**, *11*, 8984.

(48) Petrucci, S.; Masiker, M. C.; Eyring, E. M. *Journal of Solution Chemistry* **2008**, *37*, 1031–1035.

(49) Buchner, R.; Chen, T.; Hefter, G. *The Journal of Physical Chemistry B* **2004**, *108*, 2365–2375.

(50) Eberspächer, P.; Wismeth, E.; Buchner, R.; Barthel, J. *Journal of Molecular Liquids* **2006**, *129*, 3–12.

(51) *Broadband Dielectric Spectroscopy*; Kremer, F., Schönhals, A., Eds.; Springer Berlin Heidelberg: Berlin, Heidelberg, 2003.

(52) Schwichtenberg, J., *No-nonsense Classical Mechanics: A Student-Friendly Introduction*; No-Nonsense Books: 2019.

(53) Caleman, C.; van Maaren, P. J.; Hong, M.; Hub, J. S.; Costa, L. T.; van der Spoel, D. *Journal of Chemical Theory and Computation* **2012**, *8*, 61–74.

(54) Kolafa, J.; Viererblová, L. *Journal of Chemical Theory and Computation* **2014**, *10*, 1468–1476.

(55) Neumann, M. *Molecular Physics* **1983**, *50*, 841–858.

(56) Boresch, S.; Steinhauser, O. *Berichte der Bunsengesellschaft für physikalische Chemie* **1997**, *101*, 1019–1029.

(57) Self, J.; Wood, B. M.; Rajput, N. N.; Persson, K. A. *The Journal of Physical Chemistry C* **2018**, *122*, 1990–1994.

(58) Grzetic, D. J.; Delaney, K. T.; Fredrickson, G. H. *Physical Review Letters* **2019**, *122*, 128007.

(59) Gmitter, A. J.; Plitz, I.; Amatucci, G. G. *Journal of The Electrochemical Society* **2012**, *159*, A370–A379.

(60) Petibon, R.; Aiken, C.; Ma, L.; Xiong, D.; Dahn, J. *Electrochimica Acta* **2015**, *154*, 287–293.

(61) Ma, L.; Glazier, S. L.; Petibon, R.; Xia, J.; Peters, J. M.; Liu, Q.; Allen, J.; Doig, R. N. C.; Dahn, J. R. *Journal of The Electrochemical Society* **2017**, *164*, A5008–A5018.

(62) Frenkel, D.; Smit, B., *Understanding Molecular Simulation: from Algorithms to Applications*; Academic Press: San Diego, 2002; Vol. 1.

(63) Hess, B.; Kutzner, C.; van der Spoel, D.; Lindahl, E. *Journal of Chemical Theory and Computation* **2008**, *4*, 435–447.

(64) Abraham, M. J.; Murtola, T.; Schulz, R.; Páll, S.; Smith, J. C.; Hess, B.; Lindahl, E. *SoftwareX* **2015**, *1-2*, 19–25.

(65) Martínez, L.; Andrade, R.; Birgin, E. G.; Martínez, J. M. *Journal of Computational Chemistry* **2009**, *30*, 2157–2164.

(66) Soetens, J.-C.; Millot, C.; Maigret, B. *The Journal of Physical Chemistry A* **1998**, *102*.

(67) Jorgensen, W. L. *Accounts of Chemical Research* **1989**, *22*, 184–189.

(68) Jorgensen, W. L.; Maxwell, D. S.; Tirado-Rives, J. *Journal of the American Chemical Society* **1996**, *118*, 11225–11236.

(69) Canongia Lopes, J. N.; Deschamps, J.; Pádua, A. A. H. *The Journal of Physical Chemistry B* **2004**, *108*, 2038–2047.

(70) Doherty, B.; Zhong, X.; Gathiaka, S.; Li, B.; Acevedo, O. *Journal of Chemical Theory and Computation* **2017**, *13*, 6131–6145.

(71) Berendsen, H. J. C.; Postma, J. P. M.; van Gunsteren, W. F.; DiNola, A.; Haak, J. R. *The Journal of Chemical Physics* **1984**, *81*, 3684–3690.

(72) Bussi, G.; Donadio, D.; Parrinello, M. *The Journal of Chemical Physics* **2007**, *126*, 014101.

(73) Rinne, K. F.; Gekle, S.; Netz, R. R. *The Journal of Chemical Physics* **2014**, *141*, 214502.

(74) Perron, G.; Brouillete, D.; Desnoyers, J. E. Comparison of the thermodynamic and transport peroperties of lithium bis(trifluoromethylsulfonyl)imide (LiTFSI) with LiClO4 and Bu4NBr in water at 25C, 1997.

(75) Chai, J.-D.; Head-Gordon, M. *Physical Chemistry Chemical Physics* **2008**, *10*, 6615.

(76) Paier, J.; Marsman, M.; Kresse, G. *The Journal of Chemical Physics* **2007**, *127*, 024103.

(77) Tomasi, J.; Mennucci, B.; Cammi, R. *Chemical Reviews* **2005**, *105*, 2999–3094.

(78) Ribeiro, R. F.; Marenich, A. V.; Cramer, C. J.; Truhlar, D. G. *The Journal of Physical Chemistry B* **2011**, *115*, 14556–14562.

(79) Grimme, S. *Chemistry - A European Journal* **2012**, *18*, 9955–9964.

(80) Shterenberg, I.; Salama, M.; Gofer, Y.; Levi, E.; Aurbach, D. *MRS Bulletin* **2014**, *39*, 453–460.

(81) Shterenberg, I.; Salama, M.; Yoo, H. D.; Gofer, Y.; Park, J.-B.; Sun, Y.-K.; Aurbach, D. *Journal of The Electrochemical Society* **2015**, *162*, A7118–A7128.

(82) Ha, S.-Y.; Lee, Y.-W.; Woo, S. W.; Koo, B.; Kim, J.-S.; Cho, J.; Lee, K. T.; Choi, N.-S. *ACS Applied Materials & Interfaces* **2014**, *6*, 4063–4073.

(83) Giffin, G. A.; Moretti, A.; Jeong, S.; Passerini, S. *The Journal of Physical Chemistry C* **2014**, *118*, 9966–9973.

(84) Lapidus, S. H.; Rajput, N. N.; Qu, X.; Chapman, K. W.; Persson, K. A.; Chupas, P. J. *Phys. Chem. Chem. Phys.* **2014**, *16*, 21941–21945.

(85) Rajput, N. N.; Seguin, T. J.; Wood, B. M.; Qu, X.; Persson, K. A. In *Modeling Electrochemical Energy Storage at the Atomic Scale*, Springer, 2018, pp 79–124.

(86) Yamada, Y.; Yamada, A. *Journal of The Electrochemical Society* **2015**, *162*, A2406–A2423.

(87) Aurbach, D.; Pollak, E.; Elazari, R.; Salitra, G.; Kelley, C. S.; Affinito, J. *Journal of The Electrochemical Society* **2009**, *156*, A694.

(88) Burke, C. M.; Pande, V.; Khetan, A.; Viswanathan, V.; McCloskey, B. D. *Proceedings of the National Academy of Sciences* **2015**, *112*, 9293–9298.

(89) Rosenman, A.; Markevich, E.; Salitra, G.; Aurbach, D.; Garsuch, A.; Chesneau, F. F. *Advanced Energy Materials* **2015**, *5*, 1500212.

(90) Kubisiak, P.; Eilmes, A. *The Journal of Physical Chemistry C* **2018**, *122*, 12615–12622.

(91) Kimura, T.; Fujii, K.; Sato, Y.; Morita, M.; Yoshimoto, N. *The Journal of Physical Chemistry C* **2015**, *119*, 18911–18917.

(92) Baskin, A.; Prendergast, D. *The Journal of Physical Chemistry C* **2016**, *120*, 3583–3594.

(93) Salama, M.; Shterenberg, I.; Gizbar, H.; Eliaz, N. N.; Kosa, M.; Keinan-Adamsky, K.; Afri, M.; Shimon, L. J. W.; Gottlieb, H. E.; Major, D. T.; Gofer, Y.; Aurbach, D. *The Journal of Physical Chemistry C* **2016**, *120*, 19586–19594.

(94) Sa, N.; Rajput, N. N.; Wang, H.; Key, B.; Ferrandon, M.; Srinivasan, V.; Persson, K. A.; Burrell, A. K.; Vaughey, J. T. *RSC Advances* **2016**, *6*, 113663–113670.

(95) J. M. Barthel; Krienke, H.; Kunz, W., *Physical Chemistry of Electrolyte Solutions: Modern Aspects*, Springer Science & Business Media, 1998; Vol. 5.

(96) Doucey, L.; Revault, M.; Lautié, A.; Chaussé, A.; Messina, R. *Electrochimica acta* **1999**, *44*, 2371–2377.

(97) Borodin, O.; Douglas, R.; Smith, G.; Eyring, E. M.; Petrucci, S. *The Journal of Physical Chemistry B* **2002**, *106*, 2140–2145.

(98) Logan, E. R.; Tonita, E. M.; Gering, K. L.; Ma, L.; Bauer, M. K. G.; Li, J.; Beaulieu, L. Y.; Dahn, J. R. *Journal of The Electrochemical Society* **2018**, *165*, A705–A716.

(99) Cavell, E. A. S.; Knight, P. C. *Zeitschrift fur Physikalische Chemie Neue Folge* **1968**, *57*, 331–334.

(100) Farber, H.; Petrucci, S. *The Journal of Physical Chemistry* **1975**, *79*, 1221–1227.

(101) Farber, H.; Petrucci, S. *The Journal of Physical Chemistry* **1976**, *80*, 327–335.

(102) Hwang, S.; Kim, D.-H.; Shin, J. H.; Jang, J. E.; Ahn, K. H.; Lee, C.; Lee, H. *The Journal of Physical Chemistry C* **2018**, *122*, 19438–19446.

(103) Marcus, Y. *Chemical Reviews* **1988**, *88*, 1475–1498.

(104) Salomon, M. *Journal of Solution Chemistry* **1993**, *22*.

(105) Frisch, M. J. et al., *Gaussian16 Revision B.01*, 2016.

(106) Weigend, F.; Ahlrichs, R. *Physical Chemistry Chemical Physics* **2005**, *7*, 3297.

(107) Schrodinger, L. MacroModel, New York, NY, 2018.

(108) Rodriguez-Guerra, J.; Chen, J. **2018**, 10.5281/zenodo.1247565, 10.5281/zenodo.1247565.

(109) Hub, J. S.; de Groot, B. L.; Grubmüller, H.; Groenhof, G. *Journal of Chemical Theory and Computation* **2014**, *10*, 381–390.

(110) Watkins, T.; Buttry, D. A. *The Journal of Physical Chemistry B* **2015**, *119*, 7003–7014.

(111) Badiali, J.-P.; Cachet, H.; Cyrot, A.; Lestrade, J.-C. *Journal of the Chemical Society, Faraday Transactions 2* **1973**, *69*, 1339.

(112) Cole, K. S.; Cole, R. H. *The Journal of Chemical Physics* **1941**, *9*, 341–351.

(113) Grosse, C. *Journal of Colloid and Interface Science* **2014**, *419*, 102–106.

(114) Cabello, M.; Nacimiento, F.; Alcántara, R.; Lavela, P.; Pérez Vicente, C.; Tirado, J. L. *Chemistry of Materials* **2018**, *30*, 5853–5861.

(115) Jeon, B.; Heo, J. W.; Hyoung, J.; Kwak, H. H.; Lee, D. M.; Hong, S.-T. *Chemistry of Materials* **2020**, acs.chemmater.0c01112.

(116) Lipson, A. L.; Pan, B.; Lapidus, S. H.; Liao, C.; Vaughey, J. T.; Ingram, B. J. *Chemistry of Materials* **2015**, *27*, 8442–8447.

(117) Park, H.; Cui, Y.; Kim, S.; Vaughey, J. T.; Zapol, P. *The Journal of Physical Chemistry C* **2020**, *124*, 5902–5909.

(118) Ponrouch, A.; Palacin, M. *Current Opinion in Electrochemistry* **2018**, *9*, 1–7.

(119) Tchitchekova, D. S.; Ponrouch, A.; Verrelli, R.; Broux, T.; Frontera, C.; Sorrentino, A.; Bardé, F.; Biskup, N.; Arroyo-de Dompablo, M. E.; Palacín, M. R. *Chemistry of Materials* **2018**, *30*, 847–856.

(120) Wang, J.; Tan, S.; Xiong, F.; Yu, R.; Wu, P.; Cui, L.; An, Q. *Chemical Communications* **2020**, *56*, 3805–3808.

(121) Aurbach, D.; Gofer, Y. *Journal of The Electrochemical Society* **1991**, *138*, 3529–3536.

(122) Ponrouch, A.; Frontera, C.; Bardé, F.; Palacín, M. R. *Nature Materials* **2016**, *15*, 169–172.

(123) Biria, S.; Pathreeker, S.; Li, H.; Hosein, I. D. *ACS Applied Energy Materials* **2019**, *2*, 7738–7743.

(124) Wang, F.; Borodin, O.; Gao, T.; Fan, X.; Sun, W.; Han, F.; Faraone, A.; Dura, J. A.; Xu, K.; Wang, C. *Nature Materials* **2018**, *17*, 543–549.

(125) Zhang, Z.; Cui, Z.; Qiao, L.; Guan, J.; Xu, H.; Wang, X.; Hu, P.; Du, H.; Li, S.; Zhou, X.; Dong, S.; Liu, Z.; Cui, G.; Chen, L. *Advanced Energy Materials* **2017**, *7*, 1602055.

(126) Shyamsunder, A.; Blanc, L. E.; Assoud, A.; Nazar, L. F. *ACS Energy Letters* **2019**, *4*, 2271–2276.

(127) Hahn, N. T.; Driscoll, D. M.; Yu, Z.; Sterbinsky, G. E.; Cheng, L.; Balasubramanian, M.; Zavadil, K. R. *ACS Applied Energy Materials* **2020**, acsaem.0c01070.

(128) Bard, A. J.; Faulkner, L. R., *Electrochemical methods: fundamentals and applications*, 2nd ed; Wiley: New York, 2001.

(129) Wang, D.; Gao, X.; Chen, Y.; Jin, L.; Kuss, C.; Bruce, P. G. *Nature Materials* **2017**, *17*, 16–20.

(130) Hahn, N. T.; Self, J.; Seguin, T. J.; Driscoll, D. M.; Rodriguez, M. A.; Balasubramanian, M.; Persson, K. A.; Zavadil, K. R. *Journal of Materials Chemistry A* **2020**, *8*, 7235–7244.

(131) Hahn, N. T.; Self, J.; Han, K. S.; Vijayakumar, M.; Mueller, K. T.; Persson, K. A.; Zavadil, K. R. *The Journal of Physical Chemistry B* **2021**, In Press, 9.

(132) Trahey, L. et al. *Proceedings of the National Academy of Sciences* **2020**, *117*, 12550–12557.

(133) Liang, Y.; Dong, H.; Aurbach, D.; Yao, Y. *Nature Energy* **2020**, *5*, 646–656.

(134) Arroyo-de Dompablo, M. E.; Ponrouch, A.; Johansson, P.; Palacín, M. R. *Chemical Reviews* **2020**, *120*, 6331–6357.

(135) Mizrahi, O.; Amir, N.; Pollak, E.; Chusid, O.; Marks, V.; Gottlieb, H.; Larush, L.; Zinigrad, E.; Aurbach, D. *Journal of the Electrochemical Society* **2007**, *155*, Publisher: IOP Publishing, A103.

(136) Viestfrid, Y.; Levi, M.; Gofer, Y.; Aurbach, D. *Journal of Electroanalytical Chemistry* **2005**, *576*, 183–195.

(137) Mohtadi, R.; Matsui, M.; Arthur, T. S.; Hwang, S.-J. *Angewandte Chemie International Edition* **2012**, *51*, 9780–9783.

(138) Shao, Y.; Liu, T.; Li, G.; Gu, M.; Nie, Z.; Engelhard, M.; Xiao, J.; Lv, D.; Wang, C.; Zhang, J.-G.; Liu, J. *Scientific Reports* **2013**, *3*, 3130.

(139) Lu, Z.; Ciucci, F. *Chem. Mater.* **2017**, 12.

(140) Cuan, J.; Zhou, Y.; Zhou, T.; Ling, S.; Rui, K.; Guo, Z.; Liu, H.; Yu, X. *Advanced Materials* **2019**, *31*, 1803533.

(141) He, T.; Cao, H.; Chen, P. *Advanced Materials* **2019**, *31*, 1902757.

(142) Schneemann, A.; Wan, L. F.; Lipton, A. S.; Liu, Y.-S.; Snider, J. L.; Baker, A. A.; Sugar, J. D.; Spataru, C. D.; Guo, J.; Autrey, T. S.; Jørgensen, M.; Jensen, T. R.; Wood, B. C.; Allendorf, M. D.; Stavila, V. *ACS Nano* **2020**, *14*, 10294–10304.

(143) Samuel, D.; Steinhauser, C.; Smith, J. G.; Kaufman, A.; Radin, M. D.; Naruse, J.; Hiramatsu, H.; Siegel, D. J. *ACS Applied Materials & Interfaces* **2017**, *9*, 43755–43766.

(144) Deetz, J. D.; Cao, F.; Wang, Q.; Sun, H. *Journal of The Electrochemical Society* **2018**, *165*, A61–A70.

(145) Deetz, J. D.; Cao, F.; Sun, H. *Journal of The Electrochemical Society* **2018**, *165*, A2451–A2457.

(146) Arthur, T. S.; Glans, P.-A.; Singh, N.; Tutusaus, O.; Nie, K.; Liu, Y.-S.; Mizuno, F.; Guo, J.; Alsem, D. H.; Salmon, N. J.; Mohtadi, R. *Chemistry of Materials* **2017**, *29*, 7183–7188.

(147) Ta, K.; Zhang, R.; Shin, M.; Rooney, R. T.; Neumann, E. K.; Gewirth, A. A. *ACS applied materials & interfaces* **2019**, *11*, Publisher: ACS Publications, 21536–21542.

(148) Katz, A. K.; Glusker, J. P.; Beebe, S. A.; Bock, C. W. *Journal of the American Chemical Society* **1996**, *118*, Publisher: ACS Publications, 5752–5763.

(149) Carafoli, E.; Krebs, J. *Journal of Biological Chemistry* **2016**, *291*, Publisher: Elsevier, 20849–20857.

(150) Rajput, N. N.; Qu, X.; Sa, N.; Burrell, A. K.; Persson, K. A. *Journal of the American Chemical Society* **2015**, *137*, 3411–3420.

(151) Ashby, E. C.; Dobbs, F. R.; Hopkins, H. P. *Journal of the American Chemical Society* **1973**, *95*, 2823–2829.

(152) Bremer, M.; Nöth, H.; Thomann, M.; Schmidt, M. *Chemische Berichte* **1995**, *128*, 455–460.

(153) Bremer, M.; Nöth, H.; Warchhold, M. *European Journal of Inorganic Chemistry* **2003**, *2003*, 111–119.

(154) Lobkovskii, E. B.; Titov, L. V.; Psikha, S. B.; Antipin, M. Y.; Struchkov, Y. T. *Journal of Structural Chemistry* **1983**, *23*, 644–646.

(155) Petrowsky, M.; Frech, R.; Suarez, S. N.; Jayakody, J. R. P.; Greenbaum, S. *The Journal of Physical Chemistry B* **2006**, *110*, 23012–23021.

(156) Takeuchi, M.; Kameda, Y.; Umebayashi, Y.; Ogawa, S.; Sonoda, T.; Ishiguro, S.-i.; Fujita, M.; Sano, M. *Journal of Molecular Liquids* **2009**, *148*, 99–108.

(157) Fong, K. D.; Self, J.; McCloskey, B. D.; Persson, K. A. *Macromolecules* **2021**, *54*, 2575–2591.

(158) Cohen, L. H.; Saraf, D. N.; Witherspoon, P. A. *Science* **1963**, *142*, 955–956.

(159) Hall, D. S.; Self, J.; Dahn, J. R. *The Journal of Physical Chemistry C* **2015**, *119*, 22322–22330.

(160) Chang, J.; Haasch, R. T.; Kim, J.; Spila, T.; Braun, P. V.; Gewirth, A. A.; Nuzzo, R. G. *ACS Applied Materials & Interfaces* **2015**, *7*, 2494–2502.

(161) Saar, D.; Brauner, J.; Farber, H.; Petrucci, S. *The Journal of Physical Chemistry* **1978**, *82*, 2531–2535.

(162) Buchner, R.; Barthel, J. *Journal of molecular liquids* **1995**, *63*, Publisher: Elsevier, 55–75.

(163) Pu, S. D.; Gong, C.; Gao, X.; Ning, Z.; Yang, S.; Marie, J.-J.; Liu, B.; House, R. A.; Hartley, G. O.; Luo, J.; Bruce, P. G.; Robertson, A. W. *ACS Energy Letters* **2020**, *5*, 2283–2290.

(164) Doyle, M.; Fuller, T. F.; Newman, J. *Journal of the Electrochemical society* **1993**, *140*, Publisher: IOP Publishing, 1526.

(165) Dickinson, E. J.; Ekström, H.; Fontes, E. *Electrochemistry communications* **2014**, *40*, Publisher: Elsevier, 71–74.

(166) Sulzer, V.; Marquis, S. G.; Timms, R.; Robinson, M.; Chapman, S. J. **2020**, Publisher: ECSarXiv.

(167) Diederichsen, K. M.; McShane, E. J.; McCloskey, B. D. *ACS Energy Letters* **2017**, *2*, 2563–2575.

(168) Merlet, C.; Limmer, D. T.; Salanne, M.; van Roij, R.; Madden, P. A.; Chandler, D.; Rotenberg, B. *The Journal of Physical Chemistry C* **2014**, *118*, 18291–18298.

(169) Hu, Z.; Vatamanu, J.; Borodin, O.; Bedrov, D. *Physical Chemistry Chemical Physics* **2013**, *15*, 14234.

(170) Devanathan, M. A. V. *Transactions of the Faraday Society* **1954**, *50*, 373.

(171) Hamelin, A. In *Modern Aspects of Electrochemistry*, 1985; Vol. 16.

(172) Valette, G. *Journal of Electroanalytical Chemistry and Interfacial Electrochemistry* **1981**, *122*, 285–297.

(173) Shao, Y. et al. *Molecular Physics* **2015**, *113*, 184–215.

Appendix A

Appendix

A.1 Additional Details for Chapter 1

The Debye-Huckel activity coefficient terms,[24, 50] as appearing in equations 1.12 and 1.13 can be calculated via the following expression:

$$y_{\mathrm{DH},i} = \exp(-\frac{z_i^2 A_{\mathrm{DH}}\sqrt{I}}{1 + B_{\mathrm{DH}}\alpha_{\mathrm{DH}}\sqrt{I}}) \tag{A.1}$$

The ionic strength I is defined via the following expression, with z_i as species charge:

$$I = 0.5\sum_i z_i^2 c_i \tag{A.2}$$

The Debye-Huckel term B_{DH} is defined by the following expression:

$$B_{\mathrm{DH}} = \frac{F}{(\varepsilon_0 \varepsilon RT/2)^{0.5}} \tag{A.3}$$

If B_{DH} is in units of $\frac{\sqrt{m}}{\sqrt{\mathrm{mol}}}$, then a unit conversion by multiplying by $\sqrt{10}/(1 \times 10^8)$ gives B_{DH} in units of inverse concentration (mol/L) per nm, and thus B_{DH} is often reported in units of 1/nm, if I is in molar concentration units. In the case of acetonitrile, e.g. $\varepsilon = 36.0$, then $B_{\mathrm{DH}} = 4.86/\mathrm{nm}$. A_{DH} and B_{DH} can be related to the A'_{DH} and B'_{DH} for concentrations in units of molality m via multiplication by the square root of the solvent density ρ (e.g. $A'_{\mathrm{DH}} = A_{\mathrm{DH}}\sqrt{\rho}$ and $B'_{\mathrm{DH}} = B_{\mathrm{DH}}\sqrt{\rho}$). α_{DH} is the distance of closest approach between ions, e.g. ions of charges + and −. The Debye-Huckel parameter A_{DH} can be expressed via the following relationship, where the units are the square root of inverse molality, allowing A_{DH} to often be expressed as unitless provided the ionic strength is also in units of molality. An expression for A_{DH} is as follows:

$$A_{\mathrm{DH}} = \frac{Fe}{8\pi\varepsilon_0\varepsilon RT} B_{\mathrm{DH}} \tag{A.4}$$

As an example, for acetonitrile, $A_{\mathrm{DH}} = 3.80$. If using $\log_{10}(y)$ instead of the natural logarithm $\ln(y)$, as in quite common,[50] then $A_{\mathrm{DH}} = 1.65$.

The Born activity coefficient terms, as appearing in equations 1.12 and 1.13, can be calculated via a product such as the following, where α_{+-} is a distance of closest approach between ions:

$$y_{\mathrm{Born},+} y_{\mathrm{Born},-} = \exp\left(\frac{e^2}{4\pi\varepsilon_0 k_B T}\frac{|z_+ z_-|}{\alpha_{+-}}\frac{\varepsilon(c=0)-\varepsilon(c)}{\varepsilon(c=0)\varepsilon(c)}\right) \tag{A.5}$$

A.2 Additional Details for Chapter 3

Additional details on MSM

For G2, the values of A_{DH}, B_{DH} are 17.85 and 10.75 nm^{-1}, respectively. For G1, the values of A_{DH}, B_{DH} are 20.24 and 11.21 nm^{-1}, respectively. We note that these values change as the permittivity changes, according to their definition.[24] The value of α_{DH} was picked as 0.97 nm: the sum of the radii of the CIP (0.45 nm + 0.07 nm) and the anion (0.45 nm).

The permittivity correction equation can be written as follows:

$$f_{\varepsilon,\mathrm{A}} = \exp\left(a_1\frac{e^2}{4\pi\varepsilon_0 k_B T}\frac{|z_{++} z_-|}{\alpha_{+-}}\frac{\varepsilon(c=0)-\varepsilon(c)}{\varepsilon(c=0)\varepsilon(c)}\right) \tag{A.6}$$

For G1 and G2, the fit parameter a_1 was 1.02 and 0.99, and α_{+-} is 0.52 nm, the distance of closest approach between two free ions. The fact that a_1 is so close to 1 for both G1 and G2 systems indicates that α_{+-}=0.52 nm is a reasonable value to use as the sum of the cation and anion radii. We note that this value differs from that of the α_{DH} used in the Debye-Huckel activity coefficient, which is in this work picked as the sum of a CIP and free anion. Figure A.1 shows the K_{A} dependence on permittivity for G1 (left) and G2 (right), computed from quantum chemistry, and with a fit, while setting the ionic strength to 0.

Figure A.2 shows the concentration dependant association K_{A} as a function of concentration. Here, both the permitivity correction, as shown in Figure A.1, and Debye-Huckel corrections are calculated. The K_{A} values used in Figure A.2 were the ones used to obtain the fractional population of species in the MSM, as reported in the main text.

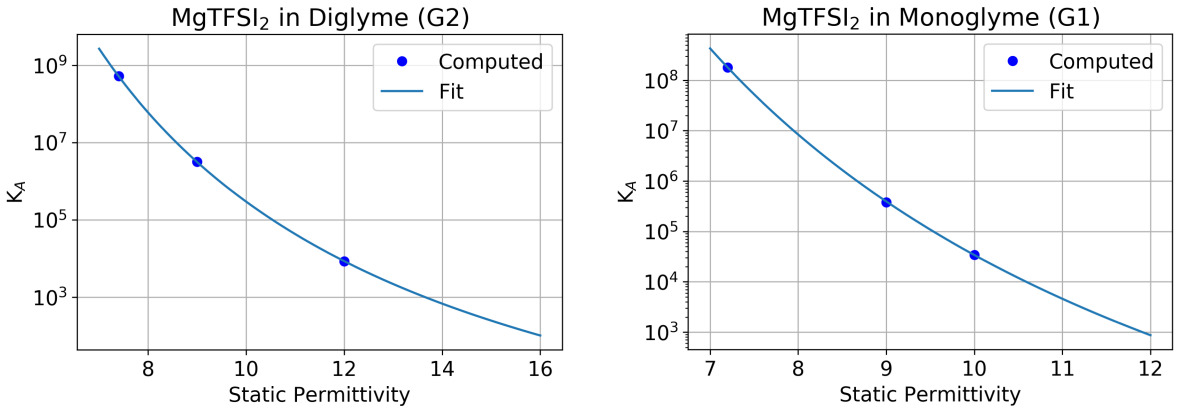

Figure A.1: MSM Permittivity correction for G2 (left) and G1 (right) electrolytes.

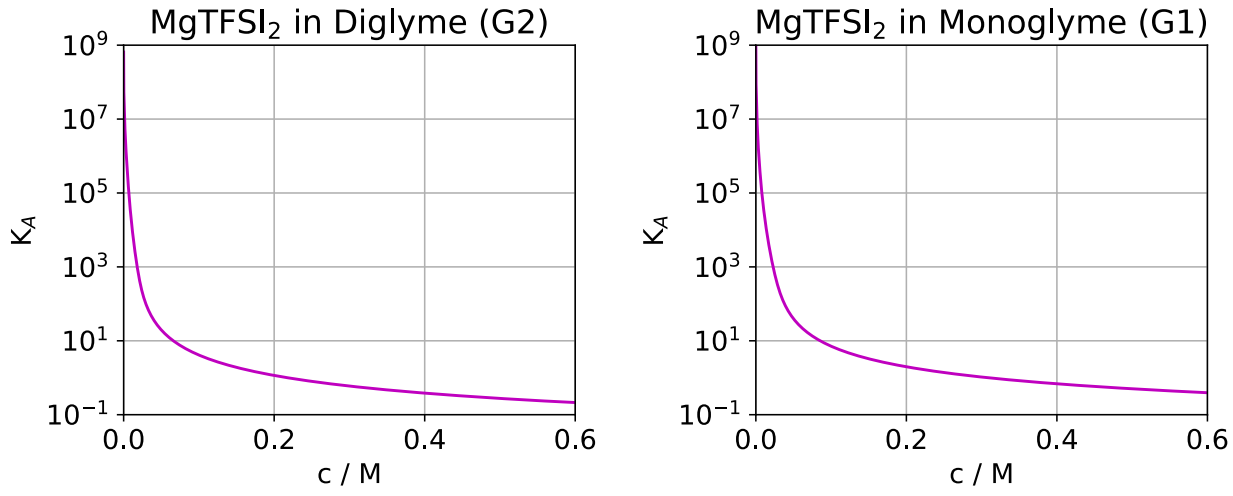

Figure A.2: MSM-calculated K_{A} plotted as a function of concentration for G2 (left) and G1 (right).

DRS data and fits

The permittivity ε can be split up into its real and imaginary parts ε' and ε'' via the following expression:

$$\varepsilon = \varepsilon' - i\varepsilon'' \tag{A.7}$$

However, the only experimentally accessible quantity in DRS, the total complex permittivity[47] ($\eta(f) = \varepsilon(f) - i\frac{\sigma}{2\pi f\varepsilon_0}$), includes a further contribution from the conductivity σ. In this work, input data was generated from an average of multiple dielectric measurements on each electrolyte solution, with fresh calibrations performed between each run. The error was taken as the standard deviation at each frequency. For a given data set, the imaginary portion of the complex total permittivity η spectrum was fit first using Grosse's program.[113] This includes both the imaginary permittivity ε'' as well as the conductivity term. Then, the fit parameters were used as initial guesses for a simultaneous fit of the real and imaginary portions of the dielectric spectrum (ε and ε'').

For G1-based electrolytes, the measured conductivity σ_{meas} was employed in the fitting procedure, while a fitted conductivity σ_{fit} was used for G2-based electrolytes. The fitted conductivity values agreed reasonably with experimental measurements (see Table A.2). For the high-concentration fits (570 mM G1 and 500 mM G2), low frequency data (f $<$ 0.9 GHz) was excluded from the fit due to difficulties in fitting the low frequency behavior, in accordance with previously reported equipment limitations.[13]

For G1 two Debye terms were used for fitting:

$$\varepsilon' = \frac{\varepsilon_1}{1+(f/f_1)^2} + \frac{\varepsilon_2}{1+(f/f_2)^2} + \varepsilon_\infty \tag{A.8}$$

$$\varepsilon'' = \varepsilon_1\frac{(f/f_1)}{1+(f/f_1)^2} + \varepsilon_2\frac{(f/f_2)}{1+(f/f_2)^2} \tag{A.9}$$

The total permittivity, also called the dielectric constant, or static permittivity, or the zero-frequency limit of the real part of the permittivity ε', can be written as :

$$\varepsilon_{\text{total}} = \varepsilon(f=0) = \varepsilon'(f=0) = \varepsilon_1 + \varepsilon_2 + \varepsilon_\infty \tag{A.10}$$

Figure A.3 shows the collected DRS data and fits for the various studied collected G1 electrolytes. Table A.1 shows the respective fit parameters used.

For G2 one Debye term and one Cole-Cole term were used for fitting:

$$\varepsilon' = \varepsilon_\infty + \varepsilon_1\frac{1}{1+(f/f_1)^2} + \varepsilon_2\frac{1+(f/f_2)^{1-\alpha_2}\sin\alpha_2\pi/2}{1+2(f/f_2)^{1-\alpha_2}\sin\alpha_2\pi/2+(f/f_2)^{2(1-\alpha_2)}} \tag{A.11}$$

$$\varepsilon'' = \varepsilon_1\frac{(f/f_1)}{1+(f/f_1)^2} + \varepsilon_2\frac{(f/f_2)^{1-\alpha_2}\cos\alpha_2\pi/2}{1+2(f/f_2)^{1-\alpha_2}\sin\alpha_2\pi/2+(f/f_2)^{2(1-\alpha_2)}} \tag{A.12}$$

Figure A.4 shows the collected DRS data and fits for the various studied collected G2 electrolytes. Table A.2 shows the respective fit parameters used.

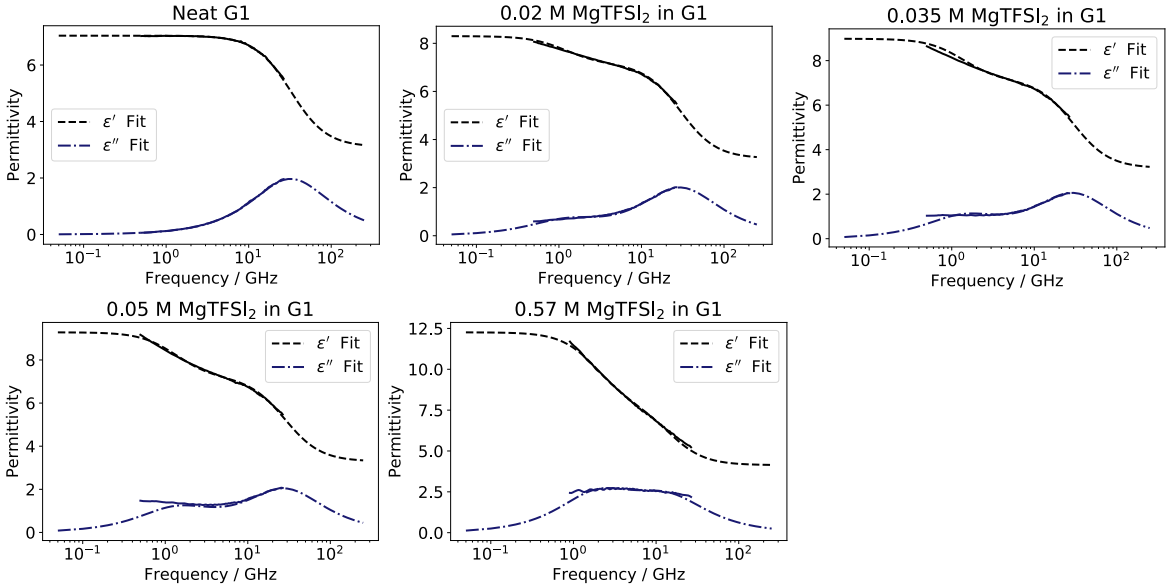

Figure A.3: Permittivity of G1 electrolyte solutions, DRS data (solid) and fits (dashed and dash-dotted).

c / M	$\varepsilon_{\text{total}}$	fit error	f_1	f_2	ε_1	ε_2	ε_∞	σ_{meas}
neat G1	7.04	0.01	-	32	-	3.94	3.10	-
0.02 M G1	8.30	0.02	1.2	30	1.16	3.92	3.22	0.06
0.035 M G1	8.98	0.02	1.4	30	1.87	3.95	3.17	0.11
0.05 M G1	9.28	0.01	1.4	28	2.10	3.89	3.30	0.18
0.57 M G1	12.26	0.01	1.9	14	4.34	3.79	4.13	7.42

Table A.1: Fit parameters for G1 electrolyte solutions. σ is here in units of mS/cm and frequency f in units of GHz.

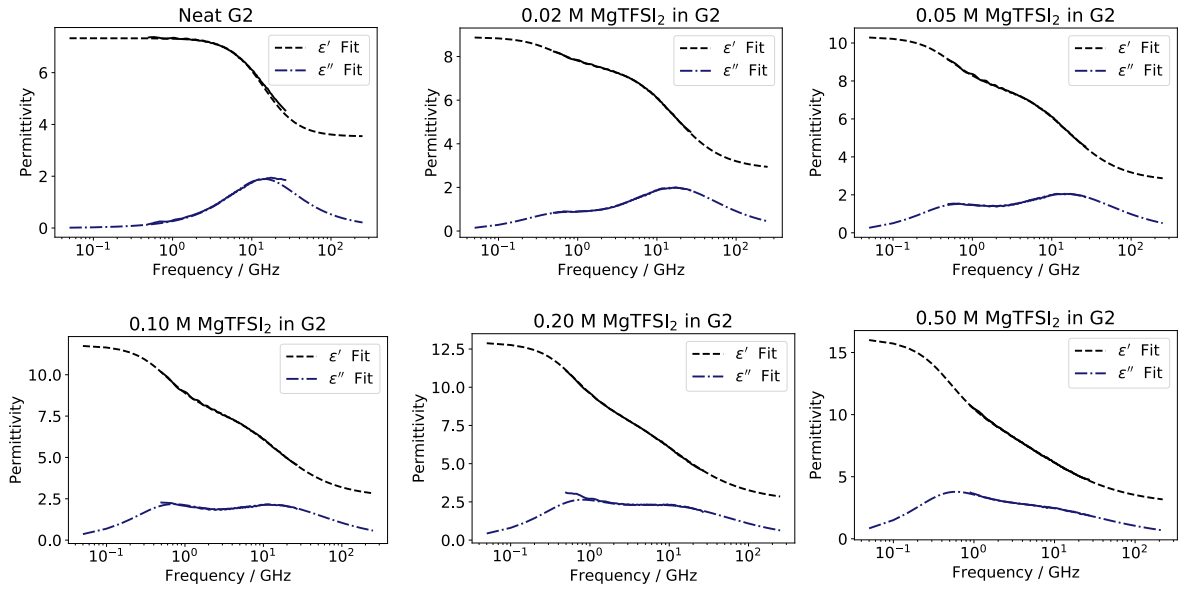

Figure A.4: Permittivity of G2 electrolyte solutions, DRS data (solid) and fits (dashed and dash-dotted).

c / M	$\varepsilon_{\text{total}}$	fit error	f_1	f_2	ε_1	ε_2	ε_∞	α_2	σ_{fit}	σ_{meas}
neat G2	7.40	0.03	-	16.0	-	4.2	3.2	0.06	-	-
0.02 M G2	8.9	0.15	0.51	16.8	1.2	4.9	2.8	0.14	0.04	0.05
0.05 M G2	10.3	0.3	0.54	16.1	2.4	5.3	2.7	0.18	0.19	0.16
0.1 M G2	11.8	0.3	0.58	14.7	3.4	5.8	2.5	0.24	0.59	0.43
0.2 M G2	13.0	0.4	0.63	11.5	3.8	6.7	2.5	0.30	1.79	1.36
0.5 M G2	16.3	0.5	0.48	6.8	5.4	8.2	2.7	0.36	3.93	4.39

Table A.2: Fit parameters for G2 electrolytes. σ is here in units of mS/cm and frequency f in units of GHz.

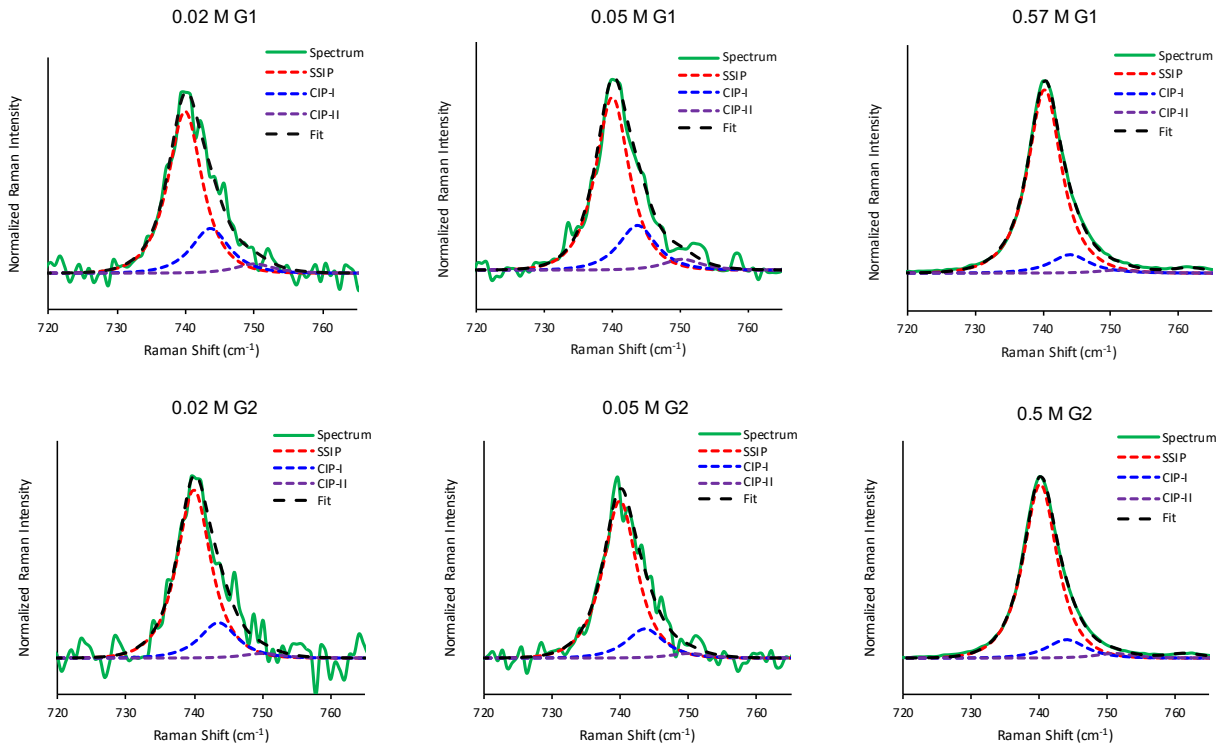

Figure A.5: Sample Raman data and fits used for population analysis.

Raman

Figure A.5 shows sample Raman data and fits used for population analysis. Table A.3 shows the inferred species population fraction. Using an approach similar to Passerini et al. [83] and Buttry et al.,[110] the $TFSI^-$ breathing mode Raman region ~ 740 cm^{-1} was fit with three pseudo-Voigt functions. The lowest frequency mode corresponds to uncoordinated $TFSI^-$, and the two higher frequency modes reflect $TFSI^-$ configurations present in CIPs (labeled CIP-I and CIP-II). Due to a poor signal:noise ratio at low concentrations, these CIP components were not used to provide more definitive structural information, but to indicate the overall fraction of the CIP and SSIP $TFSI^-$ configurations and Table S3 shows the corresponding species population fractions calculated from the Raman spectra based on the proposed dissociation equilibrium, $MgTFSI^+ \leftrightarrow Mg^{2+} + TFSI^-$. Multiple independent measurements and fittings were used to generate statistical uncertainties for these values and range from $\pm$ 1% at high concentration to $\pm$ 6% at the lowest concentration for the free $TFSI^-$ population fraction. We note that the population fraction of free Mg^{2+} is found via charge conservation knowing the population of free (or SSIP) and associated $TFSI^-$, since free Mg^{2+} population fraction cannot be directly inferred via Raman. Accordingly, error propagation leads to twice the error for free Mg^{2+} over free $TFSI^-$.

c / M	$\frac{1}{2}\frac{c_-}{c}$ ($TFSI^-$)	Error	$\frac{c_{2+}}{c}$ (Mg^{++})	Error	$\frac{c_{CIP,+}}{c}$ ($MgTFSI^+$)	Error
0.02 M G1	0.708	0.06	0.415	0.11	0.585	0.11
0.035 M G1	0.734	0.016	0.469	0.03	0.531	0.03
0.05 M G1	0.732	0.010	0.463	0.019	0.537	0.019
0.57 M G1	0.837	0.011	0.746	0.02	0.254	0.02
0.02 M G2	0.756	0.06	0.513	0.12	0.487	0.12
0.05 M G2	0.779	0.06	0.557	0.11	0.443	0.11
0.1 M G2	0.817	0.03	0.633	0.06	0.367	0.06
0.2 M G2	0.843	0.005	0.686	0.011	0.314	0.011
0.57 M G2	0.873	0.009	0.746	0.018	0.254	0.018

Table A.3: Raman analysis, with reported errors from duplicate measurements. $TFSI^-$ refers to free or SSIP species, Mg^{2+} to free cations, and $MgTFSI^+$ to associated salt species (here assumed to be CIPs).

A.3 Additional Details for Chapter 4

The following is reproduced in part with permission from the Journal Of Physical Chemistry B, https://doi.org/10.1021/acs.jpcb.1c00263,[131] Copyright 2021, American Chemical Society.

As mentioned in the main text, dielectric spectra (ε' and ε'') were measured between 0.5 and 26.5 GHz. The ε'' values were corrected for ionic conductivity. Extraction of the overall dielectric constant (static permittivity, ε_r) was accomplished by fitting both the ε' and ε'' spectra simultaneously by discrete dipole relaxations (Debye and/or Cole-Cole) and extrapolation of the total ε' spectrum to zero frequency. This fitting was performed with very few external constraints and is intended to yield an accurate measurement of ε_r rather than provide a complete deconvolution of the individual dipolar species as is sometimes attempted.[50] Many of the most polar species in $Ca(BH_4)_2$/THF have similar calculated relaxation frequencies and thus the overall ε_r is a more reliable metric. Examples of the fitted ε'' spectra are shown in Figure A.6. The relevant fitting parameters for all solutions are shown in Table A.4 and A.5. To estimate the individual species populations in $Ca(BH_4)_2$/THF using this technique, we rely on the fact that the overall change in ε_r for a given electrolyte relative to that of pure THF originates from the sum of the contributions of the various salt species present:

$$\Delta\varepsilon_r = (\varepsilon_r - \Delta\varepsilon_\infty)_c - (\varepsilon_r - \varepsilon_\infty)_0 = \Sigma(c_i \Delta\varepsilon_i) \tag{A.13}$$

where c is concentration in M and $\Delta\varepsilon$ is the computed net dielectric increment in M^{-1}; ε_∞

is the sum of higher frequency intramolecular and electronic permittivity contributions and is extracted from the fitting to isolate the contributions of dipole rotations. Because the concentrations of the various species are interrelated by the proposed overall equilibrium, $2\,Ca(BH_4)_2 \leftrightarrow Ca_2(BH_4)_4 \leftrightarrow CaBH_4{}^+ + Ca(BH_4)_3{}^-$, these concentrations can be derived analytically as shown below, where MON = neutral monomer, DIM = neutral dimer, CIP = contact ion pair cation, and QA = quadruple anion.

$$\Delta\varepsilon_r = [\mathrm{MON}]\varepsilon_{\mathrm{MON}} + [\mathrm{DIM}]\Delta\varepsilon_{\mathrm{DIM}} + [\mathrm{CIP}]\Delta\varepsilon_{\mathrm{CIP}} + [\mathrm{QA}]\Delta\varepsilon_{\mathrm{QA}} \tag{A.14}$$

$$[\mathrm{MON}] + 2[\mathrm{DIM}] + [\mathrm{CIP}] + [\mathrm{QA}] = c \tag{A.15}$$

$$[\mathrm{CIP}] = [\mathrm{QA}] \tag{A.16}$$

Rearranging equation A.16:

$$[\mathrm{DIM}] = (c - 2[\mathrm{CIP}] - [\mathrm{MON}])/2 \tag{A.17}$$

Combining equation A.14, equation A.16 and equation A.17:

$$\Delta\varepsilon_r - [\mathrm{CIP}](\Delta\varepsilon_{\mathrm{CIP}} - \Delta\varepsilon_{\mathrm{QA}}) - \frac{(c - 2[\mathrm{CIP}])}{2}\Delta\varepsilon_{\mathrm{DIM}} = [\mathrm{MON}](\Delta\varepsilon_{\mathrm{MON}} - (\Delta\varepsilon_{\mathrm{DIM}}/2)) \tag{A.18}$$

Rearranging equation A.18:

$$\frac{\Delta\varepsilon_r - [\mathrm{CIP}](\Delta\varepsilon_{\mathrm{CIP}} + \Delta\varepsilon_{\mathrm{QA}}) - \frac{(c-2[\mathrm{CIP}])}{2}\Delta\varepsilon_{\mathrm{DIM}}}{(\Delta\varepsilon_{\mathrm{MON}} - (\Delta\varepsilon_{\mathrm{DIM}})/2)} = [\mathrm{MON}] \tag{A.19}$$

From equation A.19, the values of c_i can be solved if [CIP] is known. The effective ionicity, calculated from the conductivity and diffusivity measurements, provides a first order approximation of [CIP], enabling a best estimate of the precise populations as a function of salt concentration (main text Figure 4.7). Without specifying [CIP], a range of populations could be present, as illustrated in Figure A.10.

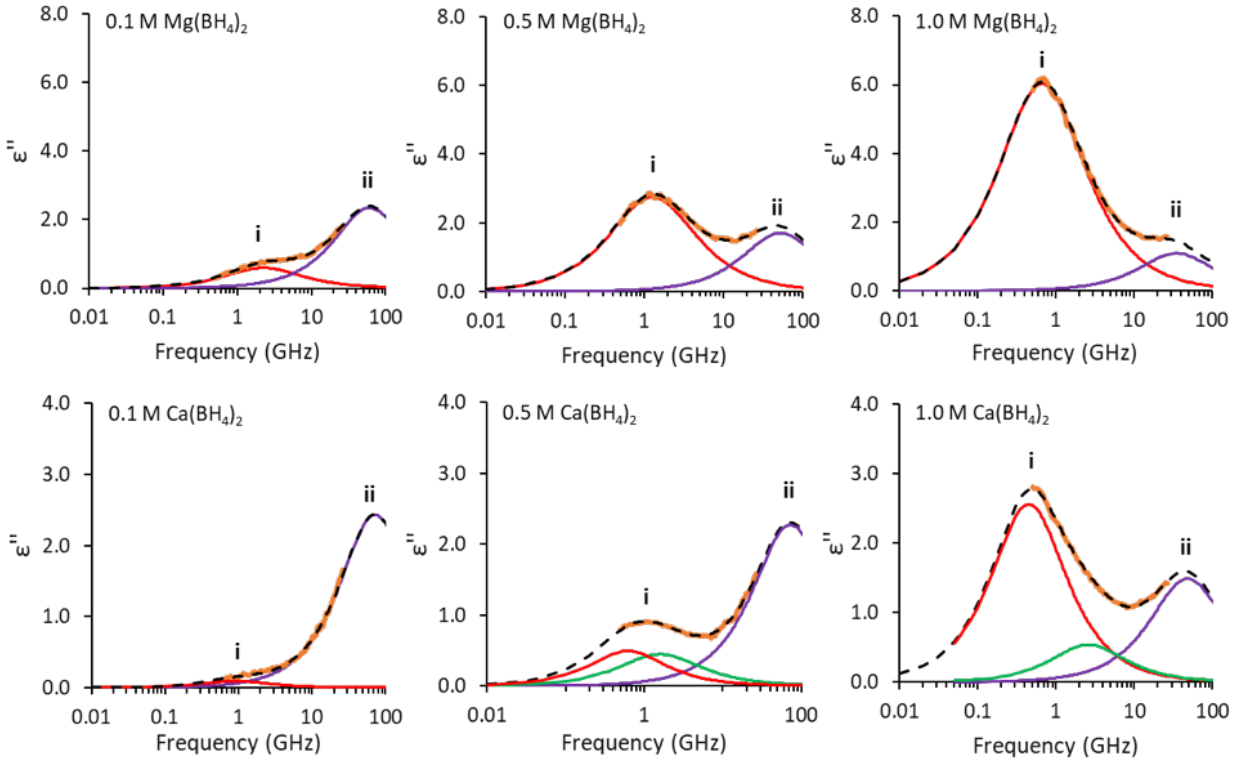

Figure A.6: Example deconvoluted fits of the imaginary permittivity spectra for $Mg(BH_4)_2$/THF (top) and $Ca(BH_4)_2$/THF (bottom) at comparable salt concentrations. The deconvoluted components (solid red, green, and purple traces) correspond to associated salt species (i) or free solvent (ii). The black dashed line represents the sum of these fitted components while the solid orange line represents the data measured from 0.5 to 26.5 GHz.

$[Mg(BH_4)_2]$ (M)	ε_∞	$\varepsilon_{\mathrm{THF}}$	f_{THF} (GHz)^a	ε_2	f_2 (GHz)	α_2^b	ε_r
0	2.59	4.81	58.8	-	-	-	7.40
0.05	2.53	4.67	59.5	0.69	2.3	0.016	7.89
0.1	2.49	4.69	60.7	1.29	2.2	0.052	8.47
0.5	2.93	3.40	52.1	6.24	1.3	0.080	12.57
1.0^c	3.88	2.17	33.7	12.13	0.8	0.075	18.17 ± 1.33

Table A.4: DRS measurement parameters for $Mg(BH_4)_2$/THF electrolytes at 21°C obtained from a fit incorporating one Debye and one Cole-Cole relaxation. $^a f = \frac{1}{2\pi\tau}$. ^{b}Cole-Cole broadening parameter. ^{c}Values at 1.0 M represent the average of two independent solution measurements.

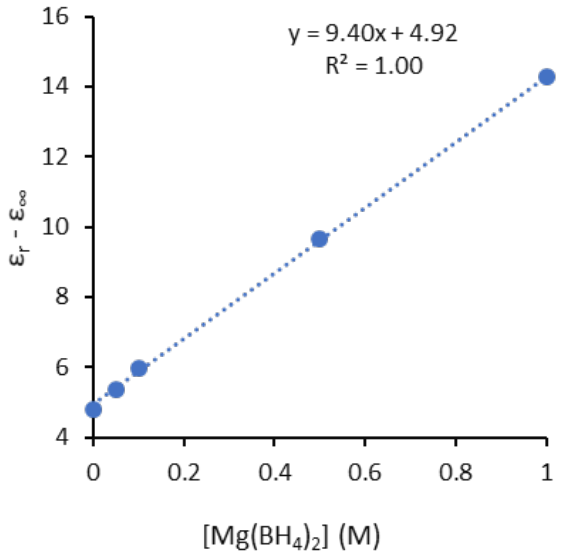

Figure A.7: Measured dipole reorientation contribution to the dielectric constant of $Mg(BH_4)_2$/THF as a function of salt concentration. A linear fit trend line and its parameters are shown. A net $\Delta\varepsilon$ of 9.4 M^{-1} is derived from this fit, similar to the predicted value of the neutral monomer (8.9 M^{-1}).

$[Ca(BH_4)_2]$ (M)	ε_∞	ε_{THF}	f_{THF} (GHz)[a]	ε_2	f_2 (GHz)	ε_3	f_3 (GHz)	ε_r
0	2.33	5.08	62.9	-	-	-	-	7.41
0.05	2.33[b]	4.91	73.7	0.01	1.0[a]	-	-	7.25 ± 0.02
0.1	2.33[b]	4.87	72.4	0.19	0.9	-	-	7.39
0.5	2.22	4.55	73.0	0.96	1.6	0.99	0.6	8.72
1	3.41	2.98	47.9	5.13	0.4	1.08	2.6	12.59
1.5	3.81	2.29	37.8	8.61	0.3	1.26	2.8	15.97

Table A.5: DRS measurement parameters for $Ca(BH_4)_2$/THF electrolytes at 21°C obtained from a fit incorporating three Debye relaxations. [a] $f = \frac{1}{2\pi\tau}$. [b]Externally constrained parameter.

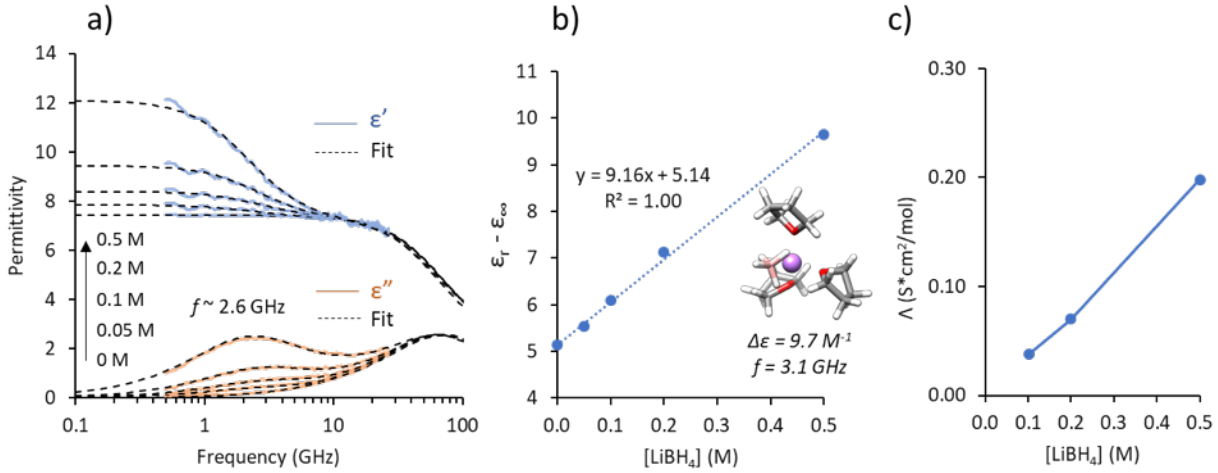

Figure A.8: a) Dielectric spectra (real and imaginary components) measured for various $LiBH_4$ concentrations in THF. Dashed lines represent fits of the data using two Debye relaxations. b) Dipolar contributions to the total permittivity extracted from DRS fits as a function of $LiBH_4$ concentration. A linear fit to this data yields an effective $\Delta\varepsilon$ of 9.2 M^{-1}. The computed structure of the $LiBH_4$ CIP cluster, including its relevant dielectric relaxation parameters determined through MD simulations is overlaid. Both the computed $\Delta\varepsilon$ and relaxation frequency (f) agree very well with the experimentally derived parameters. c) Molar conductivities measured for $LiBH_4$ in THF. The values are small (similar to $Ca(BH_4)_2$ at these concentrations) indicating weak dissociation, consistent with a population dominated by neutral CIPs.

Formula[a]	THF Number[b]	$\Delta\varepsilon^c_{\text{net}}$	$\Delta\varepsilon^d_{\text{gross}}$	f (GHz)[e]	R_g(A)[f]
$Mg(BH_4)^+$	3.8	15.0± 1.4	19 ± 1.5	1.9 ± 0.3	3.2
$Mg(BH_4)_2$	1.9	8.9± 1.2	9.5 ± 1.2	4.5 ± 0.8	2.6
$Mg(BH_4)_3^-$	0.95	1.5± 1.1	5.5 ± 1.07	4.85 ± 0.04	2.5
$Mg_2(BH_4)_3^+$	5.6	19.3± 1.3	22.2± 1.6	1.1 ± 0.2	-
$Mg_2(BH_4)_4$	3.6	17.2± 1.2	18.9± 1.9	1.38 ± 0.04	3.8
$Mg_2(BH_4)_5^-$	1.9	4.4 ± 1.0	6.0 ± 1.0	2.64 ± 0.12	-

Table A.6: Computed magnesium cluster parameters from MD simulations. [a]Formula without THF molecules. [b]Average number of coordinating THF molecules per cluster. [c]Change in dielectric constant including loss of free THF. [d]Change in dielectric constant ignoring loss of free THF. [e]Characteristic reorientation frequency. [f]Effective radius of gyration.

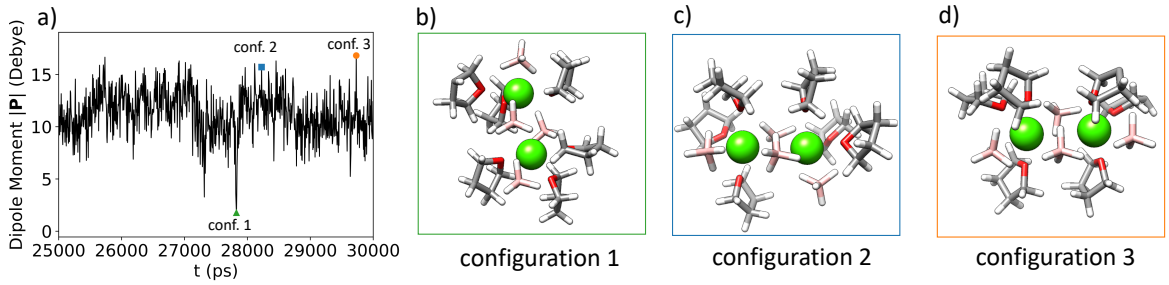

Figure A.9: a) Dipole moment magnitude of the $Ca_2(BH_4)_4$ dimer in solution vs. time during the MD simulation trajectory in units of Debye. The dipole moment plotted here is of the ionic complex which includes contributions from the ions but excludes contributions from any solvent molecules. b) Example of linear (planar) geometry of the dimer species encountered during the MD simulation (c) Example of bent geometry of the dimer species encountered during the MD simulation. (d) Example polar pyramidal geometry of the dimer species encountered during the MD simulation. Ca, B, C, H and O atoms are shown in green, pink, grey, white and red respectively.

Formula[a]	THF Number[b]	$\Delta\varepsilon^c_{\text{net}}$	$\Delta\varepsilon^d_{\text{gross}}$	f (GHz)[e]	R_g(A)[f]
$Ca(BH_4)^+$	4.8	21 ± 2	24 ± 3	1.0 ± 0.3	3.5
$Ca(BH_4)_2$	3.8	-2.1 ± 1.1	1.9 ± 1.2	16 ± 8	3.7
$Ca(BH_4)_3^-$	1.9	-2.1 ± 1.4	0.4 ± 1.7	47 ± 8	2.5
$Ca_2(BH_4)_3^+$	7	24 ± 3	24 ± 4	0.67 ± 0.02	-
$Ca_2(BH_4)_4$	5.6	16 ± 2	15.1 ± 1.4	1.07 ± 0.03	4.5
$Ca_2(BH_4)_5^-$	4	-2.1 ± 1.1	1.9 ± 1.1	23 ± 7	-

Table A.7: Computed calcium cluster parameters from MD simulations. [a]Formula without THF molecules. [b]Average number of coordinating THF molecules per cluster. [c]Change in dielectric constant including loss of free THF. [d]Change in dielectric constant ignoring loss of free THF. [e]Characteristic reorientation frequency. [f]Effective radius of gyration.

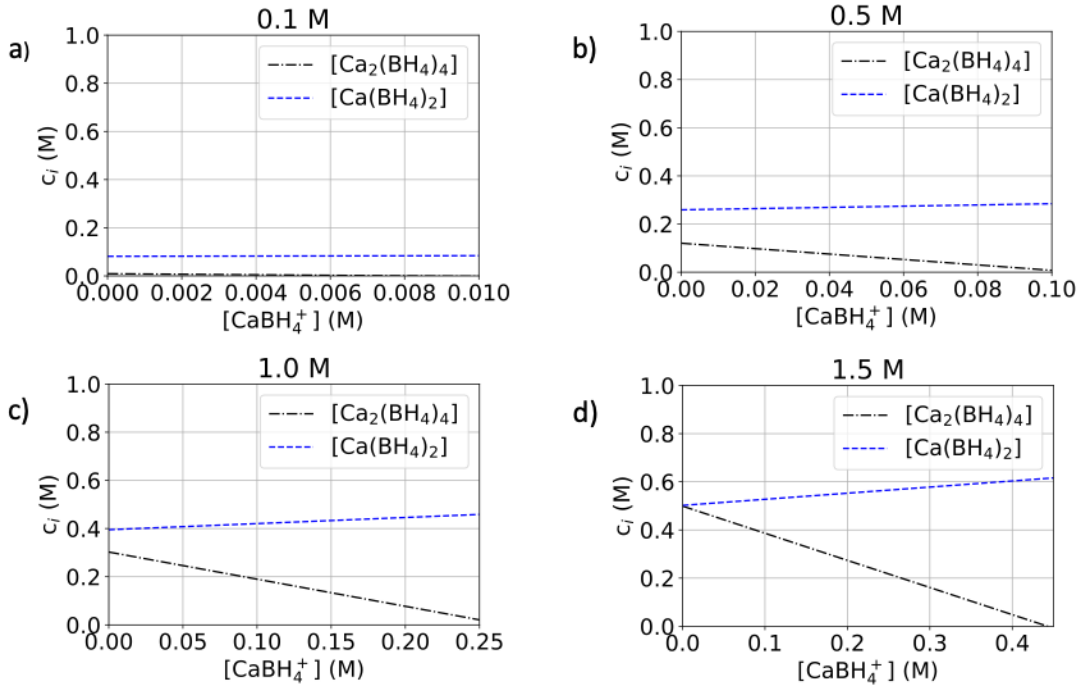

Figure A.10: Calculations of the ranges of species concentrations that could satisfy the overall measured change in dielectric constant for 0.1 M (a), 0.5 M (b), 1.0 M (c), and 1.5 M (d) $Ca(BH_4)_2$in THF as a function of $CaBH_4^+$ concentration. Fixing the value of $[CaBH_4^+]$ based on the conductivity and diffusivity measurements provides more precise estimates of the actual populations, as shown in Figure 4.7.